

AD-A235 097



(2)

Final Report: Underwater Scattering of Sound, ONR Grant N0014-90-J-1041

Victor Twersky, Principal Investigator
Mathematics Department (M/C 249), University of Illinois at Chicago
Box 4348, Chicago, IL 60680

Objective To further the understanding of volume and surface scattering effects on propagation.

Background Scattering by distributions of discrete irregularities in the sea volume and on its surface and bottom influence propagation phenomena relevant to underwater programs. To isolate basic aspects, key problems were investigated. Work in progress deals with slab regions of correlated resonant obstacles.

Approach Analytical and numerical, leading to simplified theory to clarify the essential physics and facilitate measurement and inversion of data.

Results The titles of the attached reprints indicate studies completed:

V.Twersky, "Multiple scattering by finite regular arrays of resonators", J. Acoust. Soc. Am. 87, 25-40 (1990).

R.J.Lucas and V.Twersky, "High-frequency reflection and scattering by multi-component rough surface distributions", J. Acoust. Soc. Am. 87, 1885-1893 (1990).

V.Twersky, "Comments on resonant systems of scatterers", J. Acoust. Soc. Am. 88, 1179-1180 (1990).

N.E.Berger and V.Twersky, "Moments of the Percus-Yevick hard-sphere correlation function", J. Stat. Phys. 61, 1187-1201 (1990).

N.E.Berger and V.Twersky, "Coherent propagation of sound in correlated distributions of resonant spherical scatterers", J. Acoust. Soc. Am. 89, 604-616 (1991).

V.Twersky, "Regular polygonal arrays of resonant scatterers", J. Acoust. Soc. Am. 89, 991-998 (1991).

N.E.Berger, R.J.Lucas, and V.Twersky, "Polydisperse scattering theory and comparison with data for red blood cells", J. Acoust. Soc. Am. 89, 1394-1401 (1991).

Distribution:

Scientific Officer, Code 11250A, Dr. Marshall Orr (3),
Office of Naval Research, 800 North Quincy Street, Arlington, VA 22217-5000

Administrative Grants Officer, ONR Resident Representative N62880 (1),
Administrative Contracting Officer, 536 South Clark St, Chicago, IL 60605-1588

Director, Naval Research Laboratory (1), Attn: Code 2627, Washington, DC 20375

Defense Technical Information Center (12), Building 5, Cameron Station,
Alexandria, VA 22314

DISTRIBUTION STATEMENT A

Approved for public release
Distribution Unlimited

APR 18 1991
S B D

91 4 17 007

Moments of the Percus-Yevick Hard-Sphere Correlation Function

N. E. Berger¹ and V. Twersky¹

Received April 9, 1990; final July 20, 1990

A simple recursive relation is derived for the moments M_n , $n=1, 2, \dots$ of the Percus-Yevick correlation function $h(r)$ for identical hard spheres. The M_n are rational functions of the volume fraction w occupied by the spheres; the first ten are given explicitly, and a single-term asymptotic form is obtained to suffice for the rest. Applications of the $M_n(w)$ include testing different approximations for h by numerical integration of $h(r)r^n$. We compare exact moments with shell approximations $M_n[h^s]$ corresponding to integration from $r=0$ to $s+1$ for $s=3-8$, and with hybrid approximations $M_n[h^s+h^*]$ which supplement the shell approximations with integrals of an asymptotic tail from $s+1$ to ∞ . For a given s , the hybrid approximation is better for w increasing than the shell approximation, and $M_n[h^s+h^*]$ is even better than $M_n[h^s]$.

KEY WORDS: Percus-Yevick correlation function, moments, shell expansions; asymptotic forms, residue series; hybrid approximations.

1. INTRODUCTION

The solution of the Percus-Yevick (PY) equation⁽¹⁾ for the radial distribution function $g(r)$ of a classical fluid of identical hard spheres was obtained by Wertheim⁽²⁾ and by Thiele⁽³⁾ in terms of the Laplace transform $\mathcal{L}\{g(r)\} = G(t)$. Here r is the distance from the center of one sphere divided by the sphere diameter d , so that $g(r)=0$ for $r < 1$ and $g(r)=g(w; r)$ depends on only one parameter; the volume fraction occupied by the spheres, $w = \rho \pi d^3/6$, with ρ the number density. Piecewise analytic expressions for $g(r)$ at given r in the shells $s < r < s+1$ for $s=1, 2, \dots$, can be obtained⁽²⁾ by expanding the inverse transform $\mathcal{L}^{-1}\{G(t)\}$ in a geometrical progression and summing the residues of the

¹ Mathematics Department, University of Illinois, Chicago, Illinois 60680.

terms (g_m) from $m=1$ to s . The exact results in the range $0 \leq r < s+1$ will be indicated by g^* .

Wertheim gave the closed form for g_1 , and analogs through g_5 and tabulated values are available^(4,6) for $r \leq 6$. Such shell expansions have relatively broad applicability, but we found them unsuitable except for small w for numerical investigations of integral equations⁽⁷⁾ for multiple scattering by correlated random distributions of spherical resonators. We extended the shell development to g_8 , considered the residue series for the complete⁽²⁾ $\mathcal{L}^{-1}\{G\}$ (which exhibits a Gibbs-like effect near $r=1$, but whose leading term g^* for moderately large r approximates g^*), as well as a hybrid approximation (g^b) based on g^* for $r \leq s+1$ and g^* for $r > s+1$. Although these extensions suffice for larger w than g^* , the most stable computational routines we developed for even moderately large w were based on the moments M_n of the total correlation function $h = g - 1$. The present paper deals primarily with the moments and their applications to test shell (h^*) and hybrid (h^b) forms of h by numerical integration.

The moments

$$M_n = \int_0^\infty dr h(w; r) r^n = M_n(w), \quad h = g - 1 \quad (1)$$

are simple rational functions of w . The first three are available in the literature,^(4,8,9) and we may reconstruct these and obtain additional moments by symbolic computer differentiation of $\mathcal{L}\{rh(r)\} = H(t)$. However, it is much more convenient to work with a recursive relation for the M_n based on Baxter's equation⁽¹⁰⁾ for the PY h .

Section 2 provides a form of $H(t)$ suitable for symbolic differentiation, and then derives the recursive relation for the M_n . The first ten moments $M_n(w)$ are displayed in Fig. 1 and listed in the Appendix. Section 3 derives an asymptotic series $M_n \sim \sum_i M_i^*$ for large n based on the residues at the roots $t_i(w)$ of the denominator⁽²⁾ of $H(t)$. Figure 2 graphs the first five roots, and Table I provides numerical values for the dominant root $t_1(w)$ (and for basic magnitude U_1 and phase u_1 functions); a one-term approximation M_i^* suffices for $n > 6$ and $w > 0.01$. Section 4 considers shell expansions $g^* = h^* + 1$ and compares exact $M_n(w)$ with shell approximations $M_n[h^*]$ based on numerical integration of $h^* r^n$ from $r=0$ to $s+1$ for $s=3-8$. Figure 3 displays $g(w; r)$ to $r=9$ and $w=0.6$, and Fig. 4 compares $M_2[h^*]$ and M_2 with the exact moments. Section 5 considers the convergent residue for $h(r) = \sum_i h_i^{(w)}$. Figure 5 compares exact shell results with residue sequences for $w=0.2$ and 0.6 to show the Gibbs-like effect near the discontinuity at $r=1$. Figure 6 shows that the leading residue term $h^{(1)} = h^*$ (which follows directly from Table I) suffices for $r > 5$ even for $w=0.6$.

Figure 4 also shows that the hybrid $M_6[h' + h^2] = M_6[h'] + \int_{-1}^{\infty} dr h^{*6}$ approximation is much better than the shell approximation for a given s , and that $M_6[h^3 + h^2]$ is even better than $M_6[h^3]$; the hybrid curves for M_2 included in Fig. 4 practically overlay the exact results.

2. MOMENTS OF THE CORRELATION FUNCTION

The exact leading terms of h for small w equal⁽¹¹⁾

$$\begin{aligned} h &= -1, & 0 \leq r < 1 \\ h &= w(8 - 6r + r^2/2) + \mathcal{O}(w^2), & 1 \leq r < 2 \end{aligned} \quad (2)$$

which also follow from the PY equation.⁽¹³⁾ Substituting in (1), we obtain

$$M_n = -\frac{1}{n+1} + w \frac{2^{n+2}3 - (5n^2 + 39n + 82)}{2(n+1)(n+2)(n+4)} + \mathcal{O}(w^2) \quad (3)$$

The exact w^2 contribution to h is also known⁽¹²⁾ in terms of elementary functions, and the PY approximation can be identified directly by comparison of forms in refs. 12 and 1. Although such expansions of h suffice for small w , (3) indicates that corresponding expansions of M_n are restricted to smaller w as n increases. In the following we consider closed forms of $M_n(w)$ for the PY h without restrictions on w or n .

The generating function of the moments is $\mathcal{L}\{rh(r)\} = H(t)$:

$$\begin{aligned} H(t) &= \int_0^\infty dr rh(r) e^{tr} = \sum_{n=0}^\infty \frac{(-t)^n}{n!} \int_0^\infty dr h(r) r^{n+1} \\ &= \sum_{n=1}^\infty \frac{(-t)^{n-1}}{(n-1)!} M_n \end{aligned} \quad (4)$$

$$M_n = (-1)^{n-1} \lim_{t \rightarrow 0} \frac{d^{n-1}}{dt^{n-1}} H(t) \quad (5)$$

From Wertheim,⁽²⁾ we write $\mathcal{L}\{rg\} = G$ in the form

$$G(t) = tL(t)/D(t), \quad D(t) = 12wL(t) + S(t)e^t, \quad (6)$$

where

$$S(t) = (1-w)^2 t^3 + 6w(1-w)t^2 + 18w^2t - 12w(1-w)$$

$$L(t) = (1+w/2)t + 1 + 2w$$

Thus

$$H(t) = G(t) - t^{-2} = tL(t)/D(t) - t^{-2} \quad (7)$$

COMPLETE FINAL REPORT AND DIST. STAT. A
-PER PHONE CON WITH DR. MARSHALL ORR
(ONR CODE 11250A), TELE. (703)-696-6994
VL 4-16-91

A-1

<input checked="" type="checkbox"/>	
<input type="checkbox"/>	
<input type="checkbox"/>	
per telecon	
Codes	
d/or	
il	

and (5) may be performed by machine⁽¹³⁾ operations on the equivalent form

$$H(t) = \frac{L(t)[E_2(t) - 12wE_3(t)] - (1+w/2)^2}{[1 + 12wE_4(t)]L(t) - i(1+2w)(1+w/2)} \quad (8)$$

where

$$E_n(t) = t^{-n} \left[e^{-t} - \sum_{v=0}^{n-1} (-t)^v / v! \right]$$

The Fourier transform representation of the structure factor

$$\begin{aligned} F(K) &= 1 + (6w/\pi) \int dr h(r) \exp(iK \cdot r) \\ &= 1 + (24w/K) \int_0^\infty dr rh(r) \sin(Kr) \end{aligned} \quad (9)$$

generates the even moments

$$F(K) = 1 + 24w \sum_{n=1}^{\infty} \frac{(-K^2)^{n-1}}{(2n-1)!} M_{2n} = 1 + 24wM_2 - 24w \frac{K^2 M_4}{3!} + \dots \quad (10)$$

Since $F(K) = F(w; K)$ must vanish for the unrealizable bound $w = 1$ (corresponding to zero fluctuation scattering for a uniform medium), we require $M_2(1) = -1/24$ and $M_{2n}(1) = 0$ for $n \geq 2$. The PY F is also known in closed form⁽¹⁴⁾; in particular,

$$F(w; 0) = \frac{(1-w)^4}{(1+2w)^2} = 1 + 24wM_2(w) \quad (11)$$

vanishes at $w = 1$. Equation (11), which also follows⁽¹⁵⁾ directly from the scaled particle⁽¹⁶⁾ equation of state, gives $M_2(w)$ in closed form⁽⁴⁾ by inspection. The remaining PY M_{2n} are found to have $F(w; 0)$ as a factor.

A simpler representation of the M_n follows from Baxter's equation⁽¹⁰⁾

$$rh(r) = -q'(r) + 12w \int_0^r dt (r-t) h(|r-t|) q(t) \quad (12)$$

where

$$q(r)(1-w)^2 = (1+2w)(r^2-1) - (3w/2)(r-1)$$

with $q(r) = 0$ for $r \geq 1$, and $q'(r) = dq/dr$. Operating on rh with $\int_0^x dr r^{n-1}$,

changing the order of r and t integrations, and using $h(|r-t|) = -1$ for $r < t$, yields

$$M_n = - \int_0^1 dr q'(r) r^{n-1} + 12w \int_0^1 dt q(t) \left[\frac{t^{n+1}}{n(n+1)} + \int_t^\infty dr r^{n-1} (r-t) h(r-t) \right] \quad (13)$$

Integrating over $s = r - t$ to obtain

$$\sum_{m=0}^{n-1} \binom{n-1}{m} t^m M_{n-m}$$

we define

$$\begin{aligned} - \int_0^1 dr q'(r) r^{n-1} &= \frac{A}{(1-w)^2}, & A_n &\equiv \frac{-[2n + (n-3)w]}{2n(n+1)} \\ \int_0^1 dt q(t) t^m &= \frac{B_m}{(1-w)^2}, & B_m &\equiv -\frac{[4 + 2m + (m-1)w]}{2(m+1)(m+2)(m+3)} \\ C_n &= A_n + 12w \frac{B_{n+1}}{n(n+1)} = \frac{(n^2 + 9n + 26)[3w - n(2+w)] - 12(2+w)^2}{2(n+1)(n+2)(n+3)(n+4)} \end{aligned} \quad (14)$$

Thus (13) reduces to

$$M_n(1-w)^2 = C_n + 12w \sum_{m=0}^{n-1} \binom{n-1}{m} B_m M_{n-m} \quad (15)$$

and shifting the $m=0$ term $12wB_0M_n = -w(4-w)M_n$ to the left side gives

$$M_n(1+2w) = C_n + 12w \sum_{m=0}^{n-1} \binom{n-1}{m} B_m M_{n-m} \quad (16)$$

such that $M_1 = C_1/(1+2w)$, $M_2 = (C_2 + 12wB_1M_1)/(1+2w)$, etc.

It is clear from (16) and (3) that all moments have the form

$$M_n(w) = \frac{-\mu_n(w; N)}{(n+1)(1+2w)^n}, \quad \mu_n(w; N) = 1 + \sum_{i=1}^N a_i(-w)^i \quad (17)$$

where the polynomial μ_n of order N is given by

$$\mu_n = c_n - \sum_{i=1}^{n-1} \binom{n-1}{i} \frac{n+1}{n+1-i} b_i \mu_{n-i} \quad (18)$$

with $c_n = -(n+1)C_n(1+2w)^{n-1}$, and $b_n = -12wB_n(1+2w)^{n-1}$. All c_n , and b_n except b_1 (which is proportional to w), are of order $n+1$ in w ; the order of μ_n (in general that of $b_2\mu_{n-2}$) is $N = (3n+1)/2$ for n odd, and $N = 3n/2$ for n even.

The Appendix lists the first ten moments (generated by machine⁽¹³⁾), and Fig. 1 provides a three-dimensional display to delineate trends. For $0 < w < 1$, the number of extrema (and zeros) is given by $N - n - 2 > 0$, so that successive pairs from M_5, M_6 , to M_{19}, M_{20} start with one extremum and end with eight extrema, etc.

3. ASYMPTOTIC FORM OF M_n

Since the recursive relation for M_n involves sequential determination of preceding moments, we derive an asymptotic series for large n by working with the residues at the complex roots (t_* , t_*^*) of $D(t)$ in (6).

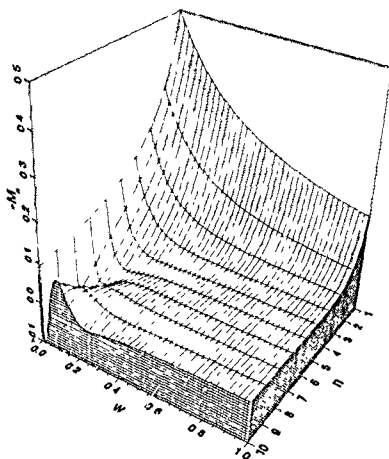


Fig. 1. Three-dimensional display to delineate trends of the first ten moments $M_n(w)$ of the hard-sphere PVh vs. volume fraction w . The values of $-M_n(0)$ are $(1+n)^{-1}$. The values of $-M_n(1)$ for $n = 1, 2, 3$ are $3/20, 1/24, 3/350$, the remaining even moments vanish, and the odd are small and alternate in sign.

As indicated by Wertheim,⁽²⁾ $t_v = -\alpha_v + i\beta_v = -|\alpha_v| + i|\beta_v|$ such that as $w \rightarrow 1$, $\alpha = 0$, and $\beta/2 = \tan(\beta/2)$. Backtracking the branches numerically yields curves versus w in Fig. 2 that show $|t_{v+1}| > |t_v|$ for the corresponding simple poles for all w .

Thus, for large n , from

$$M_n = (-1)^n \frac{(n-1)!}{2\pi i} \oint dt H(t) t^{-n} \quad (19)$$

for a contour around 0 of radius greater than any $|t_v(w)|$ of interest, we obtain⁽¹⁷⁾

$$M_n \sim (-1)^n (n-1)! 2 \operatorname{Re} \sum_v t_v^{-n+1} L_v / D'_v \equiv \sum M'_n \quad (20)$$

where

$$D'_v = \lim_{t \rightarrow t_v} \frac{dD(t)}{dt} = 12wL'_v + (S_v + S'_v) e^{t_v}$$

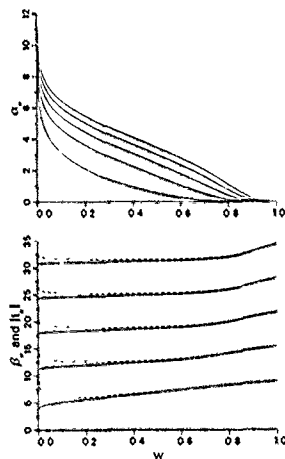


Fig. 2. First five roots $t_v = -\alpha_v + i\beta_v$, vs. $w \geq 0.001$. Top panel shows α_v , and bottom panel shows β_v (solid curves) and $|t_v|$ (dashed curves), the lowest curves correspond to $v=1$ and the highest to $v=5$. The values at $w=10^{-4}$ are: $\alpha_v = 17.109, 17.396, 17.777, 18.149, 18.484$, $\beta_v = 3.537, 10.483, 17.218, 23.803, 30.296$.

with $S_r = S(t_r)$, etc. We write

$$M_n^* = (-1)^n (n-1)! |t_r^{-n}| U_r \cos(u_r + n\tau_r) \quad (21)$$

with $U_r e^{i\tau_r} = 2t_r L_r / D_r^*$ and $\tau_r = \tan^{-1}(\beta_r/\alpha_r)$. For $n > 6$, the curves of $M_n^1(w)$ and $M_n^*(w)$ are indistinguishable for $0.01 \leq w \leq 1$ on the scale of Fig. 1; we may use M_n^1 for $n \geq 10$ and $w \geq 10^{-3}$, and for $n \geq 15$ and $w \geq 10^{-6}$. Except for $n=1$, we can obtain better accord for small w by

Table 1. Data* versus w for Dominant Root $t_1 = -\alpha + i\beta = |t| e^{-i\tau}$
and for $2t_1 L_1 / D_1^* = U e^{i\tau}$

w	α	β	$ t $	τ	U	u
0.0001	11.84249	3.72491	12.41449	0.30474	24253.0	-0.25294
0.0010	9.10273	3.90913	9.90661	0.40563	2001.6	-0.31918
0.0100	6.24844	4.25717	7.56085	0.59808	158.03	-0.43333
0.0200	5.35555	4.42760	6.94878	0.69083	72.747	-0.48600
0.0300	4.82227	4.55123	6.63083	0.75649	46.067	-0.52353
0.0400	4.43754	4.65285	6.42963	0.80908	33.261	-0.55417
0.0500	4.13469	4.74131	6.29092	0.85364	25.811	-0.58078
0.0600	3.88386	4.82086	6.19073	0.89263	20.968	-0.60474
0.0700	3.66906	4.89396	6.11660	0.92748	17.581	-0.62681
0.0800	3.48070	4.96214	6.06120	0.95910	15.038	-0.64747
0.0900	3.31259	5.02646	6.01985	0.98810	13.181	-0.66706
0.1000	3.16050	5.08765	5.98941	1.01493	11.678	-0.68579
0.1250	2.83234	5.23028	5.94794	1.07448	9.0321	-0.72988
0.1500	2.55722	5.36226	5.94081	1.12581	7.3201	-0.77130
0.1750	2.31893	5.48696	5.95685	1.17094	6.1290	-0.81100
0.2000	2.10781	5.60652	5.98966	1.21119	5.2573	-0.84961
0.2500	1.74428	5.83581	6.09091	1.28036	4.0770	-0.92497
0.3000	1.43679	6.05802	6.22607	1.33793	3.3263	-0.99929
0.3500	1.17010	6.27791	6.38602	1.38653	2.8173	-1.07338
0.4000	0.93390	6.49865	6.56570	1.42776	2.4586	-1.14738
0.4500	0.72980	6.72232	6.76182	1.46266	2.2010	-1.22080
0.5000	0.54986	6.95002	6.97174	1.49184	2.0159	-1.29245
0.5500	0.39577	7.18180	7.19270	1.51575	1.8852	-1.36043
0.6000	0.26817	7.41634	7.42119	1.53465	1.7967	-1.42215
0.6500	0.16787	7.65077	7.65261	1.54886	1.7403	-1.47463
0.7000	0.09470	7.88068	7.88125	1.55878	1.7062	-1.51534
0.7500	0.04656	8.10097	8.10111	1.56505	1.6848	-1.54326
0.8000	0.01898	8.30727	8.30729	1.56851	1.6673	-1.55959
0.8500	0.00585	8.49741	8.49741	1.57011	1.6479	-1.56738
0.9000	0.00111	8.67203	8.67203	1.57067	1.6247	-1.57016
0.9500	0.00007	8.83390	8.83390	1.57079	1.5987	-1.57076
1.0000	0.00000	8.98682	8.98682	1.57080	1.5720	-1.57080

* The values specify the moments for large n and the correlation function for large r .

retaining additional terms in v ; however, since the exact $M_n(w)$ are known, we consider only M_n^1 . Suppressing the subscript $v=1$, we have

$$M_n \sim M_n^1 \equiv M_n^2 = (-1)^n (n-1)! [t^{-n}] U \cos(u + n\tau) \quad (22)$$

Table I lists w and values for $t_1 = t = -\alpha + i\beta = |t| e^{-i\tau}$, and for the corresponding $U(w)$ and $u(w)$. This table is also appropriate for a following development of h .

4. SHELL EXPANSIONS OF g

As discussed by Wertheim,⁽²⁾ $g(r)$ can be obtained in closed form for given r from $\mathcal{L}^{-1}\{G\}$ by expanding G of (6) in powers of S^{-1} and evaluating the residues at the roots ($t_0 = |t_0|$, t_1 , $t_2 = t_1^*$) of $S(t)$. Thus, for $r \geq 1$,

$$g(r) = \sum_1^{\infty} g_m(r), \quad g^s(r) = \sum_1^s g_m(r) \quad \text{for } r \leq s+1 \quad (23)$$

such that $g_m(r) = 0$ for $r < m$, and for $r \geq m$,

$$r g_m(r) = \frac{(-12w)^{m-1}}{(m-1)!} \sum_{l=0}^2 \lim_{t \rightarrow t_l} \frac{d^{m-1}}{dt^{m-1}} \left\{ (t-t_l)^m t \left[\frac{L(t)}{S(t)} \right]^m e^{i(r-m)\tau} \right\} \quad (24)$$

where $g_m(m) = 0$ for $m > 1$. The results may be expressed as

$$r g_m(r) = \sum_{l=0}^2 C_l(m, 0) e^{i(r-m)\tau} \sum_{k=1}^m C_l(m, k) (r-m)^{k-1} \quad (25)$$

Wertheim⁽²⁾ gives forms of the coefficients for $m=1$, and forms for $m \leq 5$ are given by Smith and Henderson,^(4,5) who include numerical comparisons of shell integrations and M_2 for several values of w ; numerical tables for $g(w; r)$ are given in ref. 6.

Corresponding forms for the C_l for $m \leq 8$ (obtained by machine computations⁽¹³⁾) are implicit in Fig. 3, which displays $g(w; r)$ to $r=9$ and $w=0.6$. The first minimum of g equals zero at $w \approx 0.61257 \approx w_0$ (for $r \approx 1.3094$), and g is negative⁽⁶⁾ and physically unrealistic at slightly larger w . [The measured⁽¹⁸⁾ values of w for loose and dense random close packing of ball bearings (0.60 ± 0.02 and 0.63 ± 0.01) bracket w_0 .]

The correlation function for r in one of the first s shells is given by

$$h^s(r) = -1 + g^s(r) = -1 + \sum_{m=1}^s g_m(r), \quad 1 \leq r \leq s+1 \quad (26)$$

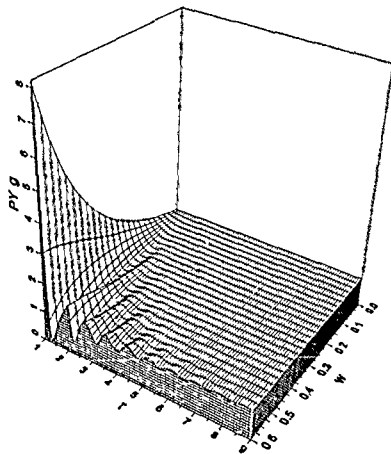


Fig. 3. Plot of PY $g(w; r)$ for $0 < w \leq 0.6$ and $1 \leq r \leq 9$. At $r=1$, the curve of $g(w; 1)$ is the PY closed form $(1+w/2)/(1-w)^2$.

We obtain s -shell approximations for the moments by numerical integration,

$$M_n[h'] \equiv \int_0^{s+1} dr h'(r) r^n \quad (27)$$

and compare with the exact M_n to obtain ranges of validity $0 \leq w \leq w(s, n)$. For given n , $w(s, n)$ increases moderately with increasing s ; for given s , $w(s, n)$ decreases markedly with increasing n . The essentials are indicated by the dashed curves $s=3-8$ in Fig. 4 for $M_2[h']$ and $M_6[h']$. (The dotted curves will be discussed subsequently.)

5. RESIDUE SERIES FOR g

Wertheim⁽²⁾ also considered the poles of $\mathcal{L}^{-1}\{G\}$ at the roots of $D(t)$ and indicated that the behavior of $h(r)$ for large r would be determined by

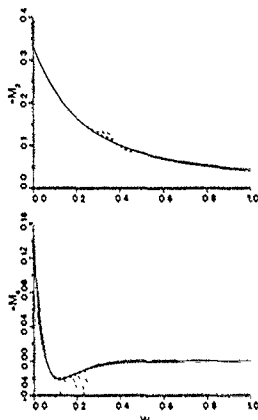


Fig. 4 The dashed curves that depart from the exact solid curves $M_2(w)$ and $M_4(w)$ at increasing values of w correspond to increasing the number of shell terms (from $s = 3$ to 8) in the approximate $M_s[h^s]$ of (27). The dotted curves that depart at larger values of w are based on the hybrid approximation $M_s[h^s + h^s]$ as in (31). The hybrid $M_s[h^s + h^s]$ is even better than $M_s[h^s]$. The hybrid $M_2[h^s + h^s]$ curves practically overlay the exact M_2 .

the pair of complex roots closest to the imaginary axis. For $r > 1$, and symbols as for (20) and (21),

$$rh(r) \approx 2 \operatorname{Re} \sum_{v=1}^{\infty} t_v L_v e^{i\theta_v} / D'_v = \sum_v U_v e^{-r\beta_v} \cos(r\beta_v + u_v) \approx r \sum_v h^{(v)} \quad (28)$$

with roots $t_v = -\alpha_v + i\beta_v$, as in Fig. 2. This residue series is rapidly convergent except in the neighborhood of $r = 1$ (the single discontinuity of h) where successive sequences exhibit a Gibbs-like effect. For any finite number (v') of terms, the peak of g occurs for $r > 1$; as v' increases (a larger v' is required for larger w), the peak approaches $r = 1$ and its magnitude overshoots the PY $g(1) = (1 + w/2)/(1 - w)^2$. Figure 5 for $w = 0.2$ and 0.6 shows the essentials for $v' = (1, 5, 10, 100)$; the overshoot at $r \approx 1.005$ for $v' = 100$ is about 9% for the smaller w and 9.4% for the larger.

For large r and $w < 1$, we need retain only the least damped exponential term

$$rh(r) \approx 2 \operatorname{Re}(t_1 L_1 e^{i\theta_1} / D'_1) = U e^{-r\beta} \cos(\beta r + u) = rh^{(1)} \approx rh^s(r) \quad (29)$$

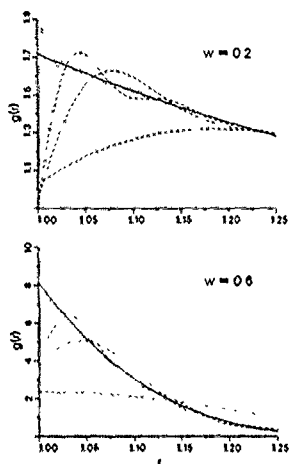


Fig. 5. Comparison of the exact $g(r)$ (solid curves) for $w=0.2$ and $w=0.6$ with v' -term residue sequence approximations (dashed or dotted curves) of (28) for $v'=(1, 5, 10, 100)$ to show the Gibbs-like effect; with increasing v' , the approximations improve except for $r \approx 1$. The peak of the dotted curves ($v'=100$) at $r \approx 1.005$ overshoots the PY g values of 1.708 and 7.805 for $w=0.2$ and 0.6 by about 8.985% and 9.395%, respectively.

The subscript 1 is suppressed, and Table I applies for U , u , α , and β . As shown in Fig. 6, h^a suffices for $r > 3$ at $w=0.2$, and for $r > 5$ at $w=0.6$. Thus, h^a supplements the shell expansion by an asymptotic tail, and provides a hybrid approximation $h \approx h^b$ for all r . For simplicity, we use

$$\begin{aligned} h^b(r) &= h^t(r) & \text{for } 1 \leq r \leq s+1 \\ h^b(r) &= h^a(r) & \text{for } r > s+1 \end{aligned} \quad (30)$$

The corresponding hybrid approximation of the moments equals

$$M_n[h^t + h^a] = M_n[h^t] + \int_{s+1}^{\infty} dr h^a(r) r^n \quad (31)$$

where we may integrate $h^a r^n$ directly. Figure 4 compares dashed curves $M_6[h^t]$ and dotted curves $M_6[h^t + h^a]$ for $s=3-8$ with the exact solid

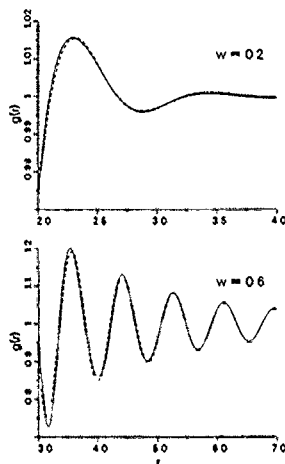


Fig. 6. Comparison of the exact g (solid curve) and leading residue term $g^{(1)} = g^*$ (dashed curve) based on (29) for $w=0.2$ and $w=0.6$. The one-term approximation g^* suffices at $w=0.2$ for $r>3$ and at $w=0.6$ for $r>5$.

curve M_6 ; for given s , the hybrid approximation holds for larger w , and $M_6[h^3 + h^s]$ is even better than $M_6[h^2]$. The hybrid dotted curves $M_2[h^s + h^s]$ in Fig. 4 practically overlay the exact solid curve M_2 . The hybrid is better than the shell approximation because h^s reduces the effects of the discontinuity of h^s at $r = s + 1$; an improved version may follow from a different match-up point than $s + 1$, but this has not been investigated.

APPENDIX. MOMENTS OF THE PY TOTAL CORRELATION FUNCTION h

$$M_1 = -\frac{10 - 2w + w^2}{10 \cdot 2(1 + 2w)}$$

$$M_2 = -\frac{(4 - w)(2 + w^2)}{8 \cdot 3(1 + 2w)^2} = -\frac{8 - 2w + 4w^2 - w^3}{8 \cdot 3(1 + 2w)^2}$$

$$M_3 = -\frac{(175 - 260w + 421w^2 - 229w^3 + 62w^4 - 7w^5)}{175 \cdot 4(1 + 2w)^3}$$

$$M_4 = -\frac{(1 - w)^4 (16 - 11w + 4w^2)}{16 \cdot 5(1 + 2w)^4}$$

$$M_5 = -(10500 - 117500w + 346930w^2 - 557372w^3 + 518840w^4 - 297700w^5 + 101255w^6 - 17130w^7 + 756w^8)/10500 \cdot 6(1 + 2w)^5$$

$$M_6 = -\frac{(1 - w)^4 (20 - 386w + 627w^2 - 494w^3 + 173w^4 - 21w^5)}{20 \cdot 7(1 + 2w)^6}$$

$$M_7 = -(404250 - 18203500w + 148479200w^2 - 507844540w^3 + 996929822w^4 - 1246675192w^5 + 1040639978w^6 - 582685390w^7 + 212379965w^8 - 46596616w^9 + 5053356w^{10} - 116424w^{11})/404250 \cdot 8(1 + 2w)^7$$

$$M_8 = -(1 - w)^4 (800 - 63540w + 620112w^2 - 1497976w^3 + 1841640w^4 - 1271145w^5 + 495980w^6 - 97656w^7 + 6048w^8)/800 \cdot 9(1 + 2w)^8$$

$$M_9 = -(500500 - 75540500w + 1560277375w^2 - 11161907350w^3 + 41072677500w^4 - 93389033916w^5 + 142984464462w^6 - 153929553204w^7 + 118569194898w^8 - 65226852406w^9 + 25074984188w^{10} - 6408278266w^{11} + 983239972w^{12} - 71735664w^{13} + 1009064w^{14})/500500 \cdot 10(1 + 2w)^9$$

$$M_{10} = -(1 - w)^4 (2800 - 743900w + 20841976w^2 - 154963970w^3 + 456008728w^4 - 745392368w^5 + 753789316w^6 - 489600083w^7 + 201915820w^8 - 49540524w^9 + 6150144w^{10} - 232848w^{11})/2800 \cdot 11(1 + 2w)^{10}$$

ACKNOWLEDGMENT

This work was supported in part by the Office of Naval Research.

REFERENCES

1. J. K. Percus and G. J. Yevick, Analysis of classical statistical mechanics by means of collective coordinates, *Phys. Rev.* **110**, 1-13 (1958).
2. M. S. Wertheim, Exact solution of the Percus-Yevick integral equation for hard spheres, *Phys. Rev. Lett.* **10**, 321-323 (1963).
3. E. Thiele, Equation of state for hard spheres, *J. Chem. Phys.* **39**, 474-479 (1963).
4. W. R. Smith and D. Henderson, Analytical representation of the Percus-Yevick hard-sphere radial distribution function, *Mol. Phys.* **19**, 411-415 (1970).
5. D. Henderson and W. R. Smith, Exact analytical formulas for the distribution functions of charged hard spheres in the mean spherical approximation, *J. Stat. Phys.* **19**, 191-200 (1978).
6. G. J. Throop and R. J. Bearman, Numerical solution of the Percus-Yevick equation for the hard sphere potential, *J. Chem. Phys.* **42**, 2408-2411 (1965); F. Mandel, R. J. Bearman, and M. Y. Bearman, Numerical solution of the Percus-Yevick equation for the Lennard-Jones (6-12) and hard sphere potentials, *J. Chem. Phys.* **52**, 3315-3323 (1970).
7. V. Twersky, Coherent scalar field in pair-correlated random distributions of aligned scatterers, *J. Math. Phys.* **18**, 2468-2486 (1977), *J. Acoust. Soc. Am.* **64**, 1710-1719 (1978).
8. H. D. Jones, Method of finding the equation of state of liquid metals, *J. Chem. Phys.* **55**, 2640-2642 (1971).
9. I. Nezbeda, Analytical solution of the Percus-Yevick equation for fluid and hard spheres, *Czech J. Phys. B* **24**, 55-62 (1974).
10. R. J. Baxter, Ornstein-Zernike relation for a disordered fluid, *Aust. J. Phys.* **21**, 563-569 (1968).
11. J. G. Kirkwood, Statistical mechanics of fluid mixtures, *J. Chem. Phys.* **3**, 300-313 (1935).
12. B. R. A. Nyboer and L. van Hove, Radial distribution function of a gas of hard spheres and the superposition approximation, *Phys. Rev.* **85**, 777-783 (1952).
13. Symbolic manipulation package Reduce, Version 3.2, Rand Corporation, Santa Monica, California (1985).
14. N. W. Ashcroft and J. Lekner, Structure and resistivity of liquid metals, *Phys. Rev.* **145**, 83-90 (1966).
15. S. W. Hawley, T. H. Kays, and V. Twersky, Comparison of distribution functions from scattering data on different sets of spheres, *IEEE Trans. Antennas Propagation* **AP-15**, 118-135 (1967).
16. H. Reiss, H. L. Frisch, and J. L. Lebowitz, Statistical mechanics of rigid spheres, *J. Chem. Phys.* **31**, 369-380 (1959).
17. P. Henrici, *Applied Computational Complex Analysis*, Vol 2 (Wiley, New York, 1977), pp. 442ff.
18. G. David Scott, Packing of spheres, *Nature* **188**, 908-909 (1960).

Coherent propagation of sound in correlated distributions of resonant spherical scatterers

N. E. Berger and V. Twersky

Mathematics Department, University of Illinois, Chicago, Illinois 60680

(Received 23 May 1990; accepted for publication 24 September 1990)

Expressions for underwater propagation in bubble regions based on the index of refraction (η) in uncorrelated random distributions of monopole resonators are restricted to sparse bubble packing (very small volume fraction w). As w increases, correlations arise, and coupling with higher-order multipoles is not necessarily negligible. To provide prototypes for data inversion, integral equations are analyzed for η in correlated distributions of spheres (including up to quadrupole coefficients) in terms of shell and moment expansions of the Percus-Yevick correlation function. Graphical results for w up to 20% indicate the decrease in magnitudes at resonance, the increase in resonance frequency, and the broadening of the resonance region relative to the uncorrelated case. A simple explicit three-moment approximation is derived for distributions of monopoles plus dipoles that provides good accord with machine computations (based on ten-moment or on eight-shell expansions) to about $w = 7.5\%$, and also holds at least qualitatively for larger w . The explicit form may also be used with the first three moments of other correlation functions.

PACS numbers: 43.30.Bp, 43.30.Ft

INTRODUCTION

The index of refraction η in uncorrelated random distributions of monopole resonators derived by Foldy^{1,2} specifies coherent propagation of sound in bubbly liquids at sparse packing (very small volume fraction w). The expression¹ for η^2 involves w only to the first order, and provides an explicit form for η in terms of a lossy monopole coefficient averaged over a distribution in bubble size, say $\eta[\bar{a}_0]$. More complete models of \bar{a}_0 are developed by Commander and Prosperetti,³ who also review recent theoretical work for the single bubble, and provide detailed comparisons of $\eta[\bar{a}_0]$ with existing data sets for $w < 1\%$. The present article uses the simplest model for a resonator, and analyzes integral equations⁴⁻⁶ for η in correlated distributions to $w = 20\%$, and obtains an explicit closed-form approximation that suffices to at least $w = 7.5\%$.

To provide prototypes for the development of data inversion routines, we consider identical spheres (specified by the relative compressibility and mass density appropriate for an air bubble in the sea⁶), and work with the Percus-Yevick (PY) correlation function⁷⁻¹¹ F . For sphere radius (a) small compared to wavelength ($2\pi/k$), and normalized frequency $x = ka$ up to 0.2, we retain not only the dominant monopole coefficient a_0 (with leading resonance⁶ $x_0 \approx 0.0140$), but also the dipole a_1 and the quadrupole a_2 . Numerical investigations of the integral equations involving only monopoles $\eta(M)$ show that the uncorrelated form $\eta[a_0]$ suffices to w about 0.1%; in turn, computations with $\eta(MD)$, which includes dipoles, show that $\eta(M)$ suffices to about 4%, and numerical results for $\eta(MDQ)$, which includes quadrupoles, substantiate $\eta(MD)$ to about 10%, the results in the remaining range to $w = 20\%$ are based primarily on $\eta(MDQ)$.

Up to $w = 12.5\%$, Figs. 1-6 on linear scales show $\text{Re } \eta^2$ and $\text{Im } \eta^2$, as well as $\text{Re } \eta$ and $\text{Im } \eta$. Figures 1 and 2 for $w = 0.1\%$ and 1% , respectively, also include the uncorrelated versions. The symmetrical curves for the elementary oscillator represented by $\eta^2[a_0]$ provide explicit reference curves and, although off scale and not included in Figs. 3-6 (at $w = 4\%$, 7.5% , 10% , and 12.5%), they serve implicitly to delineate the distortion of the curves arising from the increase in correlations with increasing w . Figures 7-10 on log-log scales compare uncorrelated and correlated results for $\text{Im } \eta$ and $1/\text{Re } \eta$.

The decrease in magnitudes at resonance and the shift in resonance frequency relative to the uncorrelated case, as well as a key difference between the correlated and uncorrelated processes, are indicated by two illustrations for the imaginary components. Writing $\text{Im } \eta^2 \equiv I$ and $\text{Im } \eta \equiv \eta_{\text{Im}}$, such that for uncorrelated distributions the peak values I_0 and $\eta_{\text{Im}0}$ increase monotonically with w , the correlated versions (I_{A} and η_{ImA}) increase to a maximum and then decrease. For $w \approx 4.6\%$, $I_{\text{A}} \approx 5500$ is maximal at $x_{\text{A}} \approx 0.0156$ (as compared to $I_0 \approx 50$ 200 at $x_0 \approx 0.0140$), for $w = 2.96\%$, $\eta_{\text{ImA}} \approx 61.4$ is maximal at $x_{\text{A}} \approx 0.0162$ (as compared with $\eta_{\text{Im}0} \approx 144$ at $x \approx 0.0141$).

The primary curves displayed to $w = 10\%$ were obtained by two different methods (shell or moment expansions) of solving the (MD) integral equation in terms of the complete a_0 and a_1 . One method used the exact first eight shells¹⁰ of F and truncated the integrals to obtain η (and then constructed η^2), the other used the first ten moments^{10,11} of F to obtain η^2 (and then constructed η). The values for both sets of η and η^2 are very close, and differ little from values obtained with the (MDQ) equation (which includes a_2) and the first 10 or 20 moments of F . For $w > 12\%$,

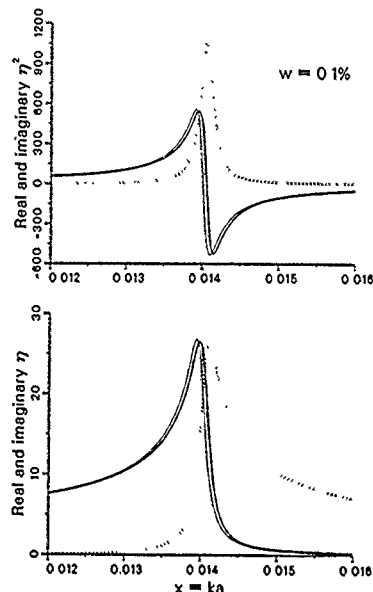


FIG. 1 The real parts are shown as solid curves, and the imaginary parts as dotted curves. The left-most curve of each pair corresponds to the uncorrelated distribution of monopoles, and the right-most curve (an overlay of several) includes correlations as well as dipoles. The effects of correlations are practically negligible, and the overlaid ten-moment curves [10(M), 10(MD)], eight-shell curves [8(M), 8(MD)], and the curves of the explicit first approximations [(M1) and (MD1)] are indistinguishable at volume fractions $w = 0.1\%$.

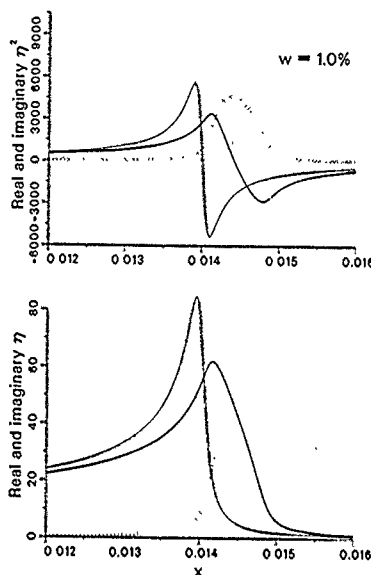


FIG. 2 Analog of Fig. 1 for a tenfold increase in volume fraction. At $w = 1\%$, the effects of correlations (the decrease in the magnitude of the extrema and their displacement to larger x , as well as the distortion of the symmetry of the simple oscillator curves) are evident. The differences in the overlaid curves of the several approximations that include correlations are negligible.

we used primarily the moment expansions. Both symbolic¹¹ and numerical procedures were used for machine computations.

To delineate the essential physics, we derive a simple explicit approximation for pure monopoles (M1) in terms of the first three moments of F_i and then generalize it to obtain a first approximation (MD1) that also includes the dipoles. The approximation (MD1) is in good accord with the ten-moment and eight-shell (MD) computations to about $w = 7.5\%$, and suffices at least qualitatively for larger w . Computations based on (MD1) involve only pocket calculator routines, and for many practical purposes we would use (MD1) instead of the ten-moment (MD) or (MDQ) to at least $w = 10\%$. Figures 1-3 include (M1), Figs 1-10 include (MD1), and Figs. 11-14 display three dimensional plots based on (MD1). The explicit form (MD1) may be used with the first three moments of other correlation functions.

The functional equation⁸ $\eta = \eta(F)$, on which our development is based, was obtained by replacing the average scattering amplitude with two obstacles fixed by that with

one fixed, analogous to Lax's procedure¹³ for the effective exciting field. Earlier explicit results⁴ for correlated resonant (or pressure release) spheres were restricted to sparse enough concentrations for the leading terms¹⁴ of F in powers of w to suffice. For other spherical scatterers and all realizable w , the correlation factor (χ) for the low-frequency scattering loss term (derived originally¹⁵ from either the scaled particle¹⁶ or identical¹⁷ PY equation of state) can be expressed in terms of the second moment of F_i , the correlation term of the associated phase¹⁸ depends on the corresponding first moment. Numerical procedures for $\eta(F)$ based on either¹⁹ three-shell or¹⁰ four shell approximations could be applied to the physical parameters⁶ of present interest, but we found that even the available⁹ five-shell approximation was inadequate for $w > 7\%$. For larger w , additional shells were required to reduce discontinuities arising from truncating infinite range integrals, our eight-shell computational procedure was stable for x to 0.1 and w to 12%. The moment expansions obviate numerical integration, and no particular difficulties arose even when the first three multipoles and the first 20 moments were retained for x to 0.2 and w to 20%.

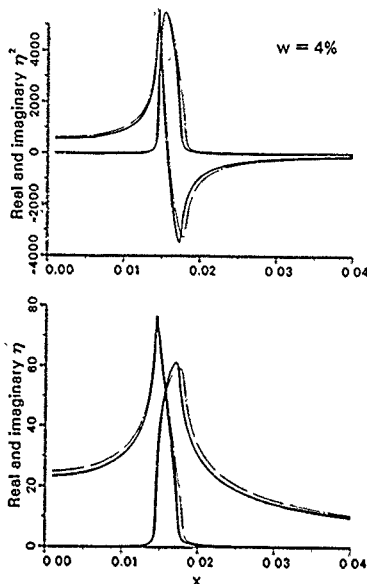


FIG. 3. Comparison of the effects of the correlations for distributions of pure monopoles, and of monopoles plus dipoles. (Note the condensed scale for x .) The chain-dot curves correspond to overlays of M results ($10(M)$, $5(M)$, $1(M)$), and the solid curves to overlays of MD results ($10(MD)$, $5(MD)$, $1(MD)$). The differences within a given set of approximations are practically negligible. In general, MD curves are displaced to smaller x than the M curves, and differences between them become more marked as w increases past 4%. The peak values of the correlated $\text{Re } \eta^2$ and $\text{Im } \eta^2$ curves are approximately equal at this value of w ; for w smaller/larger than 4%, the peak of $\text{Re } \eta^2$ is the smaller/larger of the pair.

We start with brief sketches of results for a resonant sphere (Sec. I), and of the explicit form of η^2 for uncorrelated distributions^{1,2} of monopoles (Sec. II). Then, we list integral equation approximations^{4,5} for correlated distributions and discuss moment expansions (Sec. III), and derive simplified explicit approximations for η^2 (Sec. IV). Section V describes the numerical procedures used to evaluate the shell and moment expansions for η and η^2 . Appendix A provides a simple program for computing the first 20 moments of F symbolically, and Appendix B lists the coefficients for generating the first eight shells of F .

I. PRELIMINARY CONSIDERATIONS

The forward scattering amplitude of a sphere, $g = \Sigma a_n$, is the sum of multipole coefficients of the form

$$a_n = \frac{i(2n+1)b_n}{1 - ib_n} = -\frac{2n+1}{1 + i\gamma_n}, \quad n = (0, 1, 2, \dots) \quad (1)$$

For spheres with relative compressibility C' , mass density $\rho = 1/B'$, and index of refraction $\eta' = (C'/B')^{1/2}$, we have

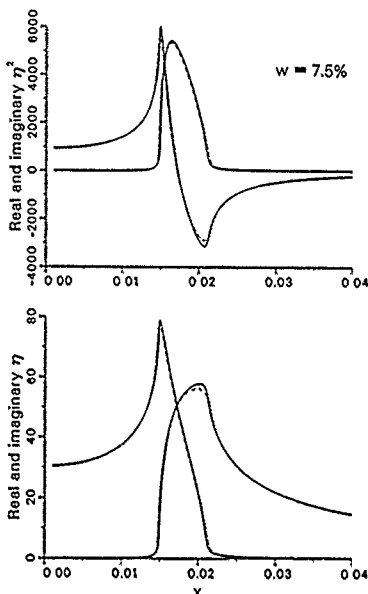


FIG. 4. The solid curves correspond to overlays of practically identical curves for $10(MD)$ and $5(MD)$, the dashed curves correspond to $1(MD)$, and the barely visible dotted curves $10(MDQ)$ include quadrupoles. The figure indicates that the explicit first approximation (MD) is satisfactory to $w = 7.5\%$, and that quadrupoles have practically no effect up to this value of w .

$$b_n = \frac{1}{\gamma_n} = \frac{R_n j_n(x) - \partial j_n(x)}{R_n n_n(x) - \partial n_n(x)}, \quad (2)$$

$$R_n = B' \eta' \frac{\partial j_n(\eta' x)}{j_n(\eta' x)},$$

where j_n and n_n are the spherical Bessel and Neumann functions, and ∂ indicates differentiation with respect to the argument $x = ka$ or $\eta' x$. We take⁶ $C' = 15.288$ and $B' = 825$ for all numerical computations and use the complete forms of a_n in general.

To delineate physical aspects for $x < 0.1$, we need retain only

$$\gamma_0 \approx \frac{3 - x^2 C'}{x^3 (C' - 1)}, \quad \gamma_1 \approx \frac{-3(B' + 2)}{x^3 (B' - 1)}, \quad (3)$$

$$\gamma_n \approx \frac{-(2n+1)!!(2n-1)!!(nB' + n + 1)}{x^{2n+1} n(B' - 1)},$$

where $(2n+1)!! = (2n+1)(2n-1)\dots 1$. These expressions provide the correct leading terms except if either $B' = 1$ or $C' = 1$. For the large values of C' and B' at hand,

$$\gamma_0 \approx \frac{x_0^2 - x^2}{x^3} \equiv \gamma,$$

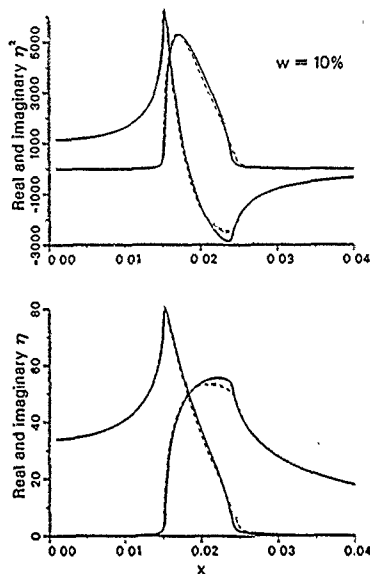


FIG 5. Analog of Fig. 4 at $w = 10\%$. Discrepancies between the solid $[10(MD)$ and $S(MD)]$ and dashed $(MD1)$ curves are more pronounced, and the dotted $10(MDQ)$ curves indicate the increasing effects of quadrupoles.

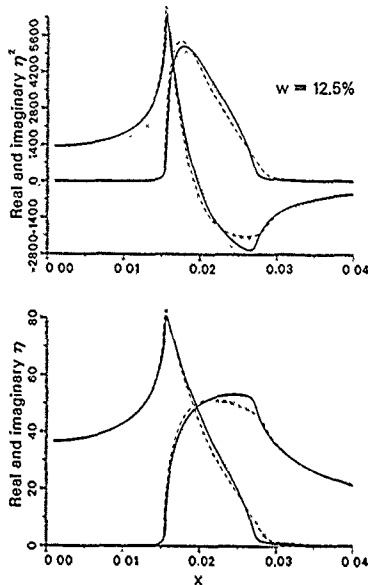


FIG 6. At $w = 12.5\%$, the solid curves consist of overlays of $10(MD)$ and $S(MD)$ results only to $x = 0.025$ (where the eight-shell computing routine becomes unstable), and of $10(MD)$ results for larger x . The dashed $(MD1)$ curves are further from the $10(MD)$ base curves in key ranges of x , and the dotted $10(MDQ)$ curves no longer substantiate $10(MD)$ in these same key regions.

$$\gamma_1 \approx \frac{-3}{x^3}, \quad \gamma_n \approx \frac{-(2n+1)!!(2n-1)!!}{x^{2n+1}}, \quad (4)$$

where $x_0 = [3/(C' - 1)]^{1/2} = 0.0140$. (We use $C' - 1$ instead of C' to obtain checks at $x \approx 0$.) The form $\gamma_0 = \gamma$ corresponds to a resonance form of a_0 , and the remaining γ_n and a_n are pressure release approximations.

II. UNCORRELATED DISTRIBUTIONS OF MONOPOLES

Foldy's systematic procedure¹ for multiple scattering by uncorrelated monopoles leads to

$$\eta^2 = 1 - iSa_0 = 1 + \frac{iS}{1 + i\gamma},$$

$$S = \frac{4\pi N}{k^3} = \frac{3w}{x^3}, \quad w = \frac{N4\pi a^3}{3}, \quad (5)$$

where N is the number density and w is the volume fraction. The corresponding bulk index of refraction η specifies the propagation of sound in sparse (very small w) random distributions of nonabsorbing resonators. In the neighborhood of the resonance frequency x_0 , the behavior of

$$\eta^2 = 1 + S\gamma/(1 + \gamma^2) + iS/(1 + \gamma^2) \equiv R + iI \quad (6)$$

is that of an elementary oscillator. The left-most curves of

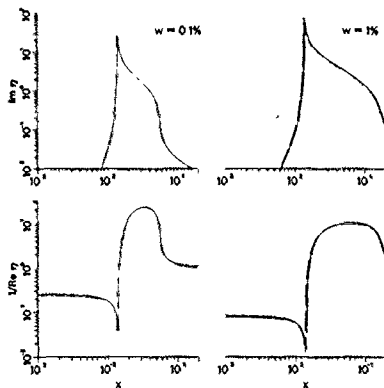


FIG 7. Logarithmic plots of $\text{Im } \eta$ (such that $2k \text{Im } \eta$ equals the attenuation coefficient) and of $1/\text{Re } \eta$ (the relative phase speed) at $w = 0.1\%$ and 1% , corresponding to values in Figs. 1 and 2. Uncorrelated monopole results are indicated by chain-dot curves, $10(MD)$ results by solid curves, $(MD1)$ results by dashed curves, and $10(MDQ)$ results by dotted curves. The effects of correlation are negligible on such scales.

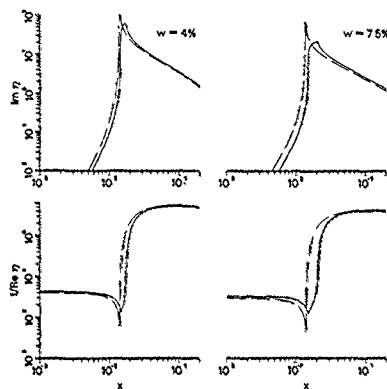


FIG. 8 Analog of Fig. 7 for values in Figs. 3 and 4 at $w = 4\%$ and 7.5% shows that the explicit first approximation (MD 1) suffices even to $x = 0.2$.

each pair in the top panels of Figs. 1 and 2 (at $w = 0.1\%$ and 1% , respectively) correspond to R to I of (6) in terms of γ_0 of (2). The shape of the curves and the location of the extrema are unchanged as w increases and the magnitudes increase linearly with w .

At resonance,

$$\gamma = 0, \quad x = x_0 \approx 0.014, \quad R = 1, \quad I = S, \quad (7)$$

where S is the maximum value. For I at half-strength,

$$\gamma = \pm 1, \quad x = x_{\pm} \approx x_0 \pm \frac{x_0^2}{2},$$

$$R = 1 \mp \frac{S}{2}, \quad I = \frac{S}{2}. \quad (8)$$

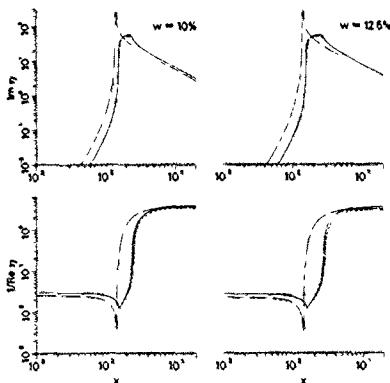


FIG. 9 Analog of Fig. 7 for values in Figs. 5 and 6 at $w = 10\%$ and 12.5% shows the increasing role of correlations. Note that (MD 1) suffices at least for $\text{Im } \eta$.

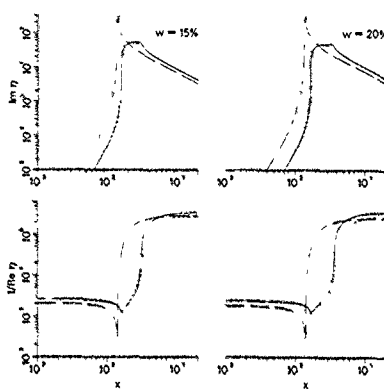


FIG. 10 Analog of Fig. 7 for values of w at which the $10(MDQ)$ results should be checked by including octupoles. The closeness of (MD 1) curves to the other correlated curves, particularly to the $10(MDQ)$ at relatively large x , is fortuitous.

and the peak width of I corresponding to x_{\pm} , $-x_{\pm} \approx x_0^2$ is very narrow. Outside of the resonance region, as $|\gamma|$ and $|x - x_0|$ increase, the magnitude of I decreases more rapidly than that of R .

On the other hand, for $x \approx 0$,

$$R \approx 1 + \frac{S}{\gamma} \approx 1 + w(C' - 1),$$

$$I \approx \frac{S}{\gamma^2} \approx \frac{w(C' - 1)^2 x^2}{3}, \quad C_0 \approx R + iI, \quad (9)$$

where C_0 is the complex bulk compressibility, with R as the elementary mixture approximation and I as the first approximation for the scattering loss term (as discussed earlier).

For $x \approx 0.1$, the forms $R \approx 1 - 3w/x^2$ and $I \approx 3w/x$ correspond to the leading terms of η^* for pressure release spheres.

In terms of R and I , the real and imaginary parts of η are given by

$$\eta = \eta_r + i\eta_i, \quad \begin{bmatrix} \eta_r \\ \eta_i \end{bmatrix} = \left(\frac{\sqrt{R^2 + I^2} \pm R}{2} \right)^{1/2}. \quad (10)$$

Since the peak width (x_0^2) of I is narrow, the influence of I in (10) is restricted to the neighborhood of x_0 , and since $R - 1 = \pm |R - 1|$ for $x \leq x_0$, we see that η_r increases relatively gradually to its peak and then falls steeply. From the values of $R - 1 \approx R$ and of I at x_{\pm} and x_0 , it follows that η_r increases to approximately $[S(\sqrt{2} + 1)]^{1/2}/2$ at x_{\pm} , and then decreases to about $(S/2)^{1/2}$ at x_0 , and to about $[S(\sqrt{2} - 1)]^{1/2}/2$ at x_{\pm} . The converse applies for η_i , which rises steeply to its peak at x_{\pm} , etc. The left-most curves of each pair in the bottom panels of Figs. 1 and 2 correspond to η_r and η_i in terms of γ_0 of (2), and Figs. 7-10 on logarithmic scales shows η_r and $1/\eta_r$ for $w = 20\%$. For uncorrelated distributions, the shape of the curves and the location of the

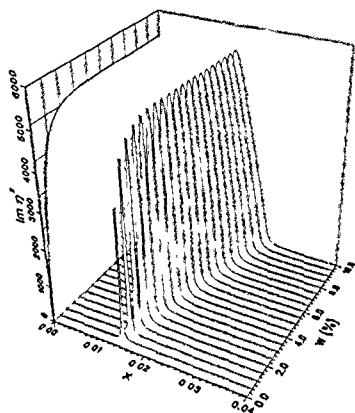


FIG. 11. Three-dimensional plot (showing 20 silhouettes) of $\text{Im } \eta^2$ based on (MD 1). The solid curve on the left wall, a projection of all peak values to $w = 10\%$, has a maximum of approximately 5350 for $x \approx 0.0157$ at $w \approx 5.2\%$; the value based on 10(MD) approximates 5500 for $x \approx 0.0156$ at $w \approx 4.6\%$.

extrema are unchanged as w increases, and the magnitudes increase as \sqrt{w} .

The right-most curves in Figs. 1 and 2 show the effects of correlations. Figs. 3-6, which are also on linear scales, display only curves that include correlations (the uncorrelated versions are far off scale); their top panels for η^2 show the

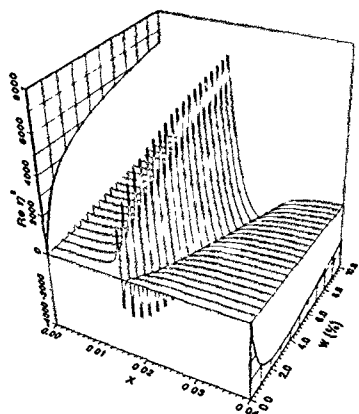


FIG. 12. Three-dimensional silhouette and projection plot of $\text{Re } \eta^2$ based on (MD 1). The solid curve on the right wall of the base, a projection of all minimum values of $\text{Re } \eta^2$, has a minimum of approximately -3550 for $x \approx 0.0163$ at $w \approx 2.9\%$; the value based on 10(MD) approximates -3480 for $x \approx 0.0167$ at $w \approx 3.3\%$.

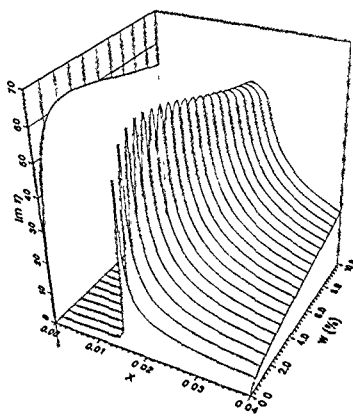


FIG. 13. Three-dimensional silhouette plot of $\text{Im } \eta$ based on (MD 1). The solid curve on the left wall, a projection of all peak values to $w = 10\%$, has a maximum of approximately 62.2 for $x \approx 0.0160$ at $w \approx 2.64\%$; the value based on 10(MD) approximates 61.4 for $x \approx 0.0162$ at $w \approx 2.96\%$.

distortion of the symmetrical oscillator curves in Figs. 1 and 2 that arises with increasing w , so that the uncorrelated cases provide implicit reference curves.

To first order in w , we may generalize (5) directly to include higher-order multipoles, i.e.,

$$\frac{-(\eta^2 - 1)}{iS} = \sum a_n = a_0 + a_1 + \dots, \quad (11)$$

but in the ranges of x and w where (5) is valid, we see from (4) that the higher-order coefficients are negligible. How-

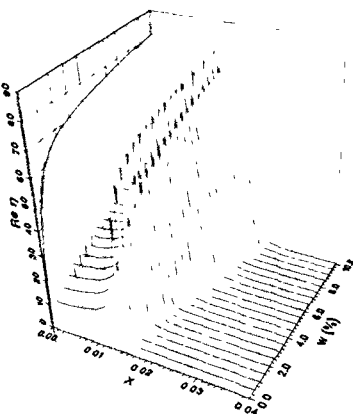


FIG. 14. Three-dimensional silhouette and projection plot of $\text{Re } \eta$ based on (MD 1).

ever, for denser packing, the maximal fluctuations implicit in (5) and (11) are decreased by the correlations in the separations of neighbors that arise from the decrease in elbow room per particle. Higher-order terms in w must be included, and the dominant a_0 is coupled with all a_n by the required functions of η and w .

III. CORRELATED DISTRIBUTIONS

The earlier⁵ development of integral equation approximations for correlated random distributions of obstacles was summarized⁴ and applied to various cases involving only a_0 and a_1 . These articles^{4,5} indicate limitations, provide full details, and cite related approximations. Now we merely list the required generalization of (11), and discuss only the forms for our numerical computations and graphical results.

As shown earlier,⁵ the index is specified by

$$\frac{\eta^2 - 1}{-iS} = \sum P_n, \quad P_n = a_n \eta^{2n} \left(1 + \sum h_n, P \right),$$

$$h_n = \frac{\mathcal{H}_n}{\eta^{2n}}, \quad (12)$$

where $\mathcal{H}_n = \mathcal{H}_{nn}$ is expressed in terms of S , η , and the correlation integrals (continuum versions of lattice sums)

$$\mathcal{H}_n = 24w \int_0^\infty F(r) f_n(\eta 2xr) h_n^{(1)}(2xr) r^2 dr$$

$$= f_n' + i f_n'', \quad (13)$$

Here, F is the correlations function,^{7,11} and $h_n^{(1)} = j_n + i n_n$ with corresponding $f'(j)$ and $f''(jn)$. For brevity, we introduce self-coupling coefficients and work with

$$p_n = \frac{a_n \eta^{2n}}{1 - a_n \eta^{2n} h_{nn}} = \mathcal{A}_n \eta^{2n},$$

$$\mathcal{A}_n = \frac{a_n}{1 - a_n \mathcal{H}_{nn}}, \quad \mathcal{H}_{nn} = \mathcal{H}_n. \quad (14)$$

Retaining a specified number of isolated scattering coefficients a_n in (12), we solve the truncated algebraic system for P_n , and construct ΣP_n to obtain integral equation approximations for η .

Thus, if we retain only the monopole a_0 , then

$$\frac{\eta^2 - 1}{-iS} = p_0 = \mathcal{A}_0 = \frac{a_0}{1 - a_0 \mathcal{H}_{00}} = \frac{-1}{1 + i\gamma_0 + \mathcal{H}_{00}}. \quad (15)$$

The self-coupling coefficient \mathcal{A}_0 includes all orders of monopole-monopole coupling. If we keep both a_0 and the dipole a_1 ,

$$\frac{\eta^2 - 1}{-iS} = \frac{p_0 + p_1 + 2p_0 p_1 h_{01}}{1 - p_0 p_1 h_{01}^2}$$

$$= \frac{\mathcal{A}_0 + \mathcal{A}_1 \eta^2 + 2\mathcal{A}_0 \mathcal{A}_1 \eta \mathcal{H}_{01}}{1 - \mathcal{A}_0 \mathcal{A}_1 \mathcal{H}_{01}^2},$$

$$\mathcal{A}_1 = \frac{a_1}{1 - a_1 \mathcal{H}_{11}} = \frac{-3}{1 + i\gamma_1 + iS + \mathcal{H}_{00} + 2\mathcal{H}_{01}}, \quad (16)$$

where we used⁴ $\mathcal{H}_{11} = (iS + \mathcal{H}_{00} + 2\mathcal{H}_{01})/3$. The coefficient

\mathcal{A}_1 includes all orders of dipole-dipole coupling, and \mathcal{A}_0 includes the cross coupling terms. If the quadrupole a_2 is also retained in (12),

$$- (\eta^2 - 1) D / iS$$

$$= p_0 + p_1 + p_2 + 2(p_0 p_1 h_{01} + p_0 p_2 h_{02} + p_1 p_2 h_{12}) + p_0 p_1 p_2 (2h_{01} h_{02} + 2h_{01} h_{12} + 2h_{02} h_{12} - h_{01}^2 - h_{02}^2 - h_{12}^2), \quad (17)$$

$$D = 1 - p_0 p_1 h_{01}^2 - p_0 p_2 h_{02}^2 - p_1 p_2 h_{12}^2$$

$$- 2p_0 p_1 p_2 h_{01} h_{02} h_{12},$$

where⁵ $\mathcal{H}_{12} = (iS 2\eta + 2\mathcal{H}_{01} + 3\mathcal{H}_{02})/5$, and $\mathcal{H}_{22} = \{iS(7 + 17\eta^2) + 7\mathcal{H}_{00} + 10\mathcal{H}_{02} + 18\mathcal{H}_{01}\}/35$. The p_n include coupling of similar multipoles, and product terms correspond to cross coupling. Since $\mathcal{H}_n = \mathcal{H}_n(\eta)$, these representations constitute integral equations for η . We refer to (15)–(17), as well as to the corresponding numerical and graphical results they lead to by M , MD , and MDQ .

The integration variable r in (13) represents distance from the center of one sphere divided by sphere diameter ($2a$). For impenetrable identical spheres, $F(r) = f(r) - 1$ (with f as the radial distribution function^{7,11}) depends only on the normalized distance r and the volume fraction w . The exact leading terms of F for small w are given by¹⁴

$$F(r) = -1, \quad 0 < r < 1, \quad (18)$$

$$F(r) = w(8 - 6r + r^3/2) + \mathcal{O}(w^2), \quad 1 < r < 2, \quad (19)$$

which also follow⁷ from the PY approximation. The region $0 < r < 1$ is the exclusion region containing the center of only one sphere; if we retain only (18) in (13), then $\mathcal{H}_n = \mathcal{H}_n(w)$ corresponds to the hole approximation. The region $1 < r < 2$ is the first shell ($s = 1$), and the successive shells correspond to $s < r < s + 1$ for integer values of s . If we retain (18) and (19), i.e., the first two terms of the virial expansion of F , then \mathcal{H}_n is correct to $\mathcal{O}(w^2)$.

Exact expressions for the PY- $F(r)$ in the first five shells (corresponding to $r < 6$) are available^{8,9} for numerical investigations, and we generated analogous expressions for the next three shells to obtain exact forms for $r < 9$, see Appendix B. Truncating the infinite range integrals in \mathcal{H}_n at $r = 9$ and solving for η numerically lead to the eight-shell results for η^2 and η that we cite subsequently as $S(M)$ and $S(MD)$; these are plotted in Figs. 1–5 (as well as in Fig. 6 to $x = 0.025$) but are overlaid by other curves. However, our most stable computing routines are based on using the moments of the PY- F .

Expanding the integrand of \mathcal{H}_n in powers of r isolates the moments

$$\int_0^\infty F(r) r^n dr = M_n(w). \quad (20)$$

These are simple rational functions of w . The first four^{10,11} equal

$$M_1 = -(10 - 2w + w^2)/10 \times 2(1 + 2w),$$

$$M_2 = -(4 - w)(2 + w^2)/8 \times 3(1 + 2w)^2,$$

$$M_3 = -(175 - 260w + 421w^2 - 229w^3 + 62w^4 - 7w^5)/175 \times 4(1 + 2w)^3, \quad (21)$$

$$M_4 = -(1-w)^4(16-11w+4w^2)/16 \times 5(1+2w)^4.$$

All PY moments are given by the recursive relation¹⁰

$$\begin{aligned} M_n(1+2w) &= L_n + \frac{12wE_{n+1}}{n(n+1)} \\ &\quad + 12w \sum_{m=1}^{n-1} \binom{n-1}{m} E_m M_{n-m}, \\ L_n &= -\frac{[2n + (n-3)w]}{2n(n+1)}, \\ E_n &= -\frac{[4 + 2m + (m-1)w]}{2(m+1)(m+2)(m+3)}. \end{aligned} \quad (22)$$

Appendix A provides a simple program for generating the first 20 moments by machine. [Note that the hole approximation (18) in (20) gives the leading term $-1/(n+1)$, and (19) gives the $\mathcal{O}(w)$ terms of M_n .]

Substituting the standard series expansions of f_n and n_n into $\mathcal{N}_n = f_n + iI_n$ as in (13), we identify simple integrals of the form (20) to construct

$$\begin{aligned} f_n &= \frac{\eta^2 x^2 24w}{[(2n+1)w]^2} \\ &\quad \times \left(M_2 - \frac{2x^2}{2n+3} (\eta^2 + 1) M_4 + \dots \right), \\ I_n &= \frac{-\eta^2 12w}{x(2n+1)} \\ &\quad \times \left[M_1 - 2x^2 \left(\frac{\eta^2}{2n+3} + \frac{1}{1-2n} \right) M_3 + \dots \right]. \end{aligned} \quad (23)$$

Using these expansions for \mathcal{N}_n in (15)–(17) leads to algebraic equations for the corresponding η^2 that can be solved¹² by machine. Computations with the correlated monopole (M) form (15) determine the range of w where the uncorrelated form (5) is valid, and similarly the MD form (16) restricts (15), and the MDQ form (17) restricts (16). We use (17) to $w = 20\%$, where the differences with (16) are relatively marked (except on log-log plots, i.e., Fig. 10), but an upper bound for its range of validity is not available. Figures 1–10 display ten-moment results for η (the first six include η^2) cited as $10(M)$, $10(MD)$, and $10(MDQ)$; we computed corresponding 20-moment values for substantiation, and found the differences to be minor.

IV. EXPLICIT APPROXIMATIONS

To delineate the essential physics, we derive a simple approximation for pure monopole resonators, and then generalize the expression to include leading dipole contributions.

From (15),

$$\eta^2 - 1 = -iS\mathcal{C}_0 = iS/[1 + f_0 + i(\gamma + f_0)] \quad (24)$$

and we may substitute the leading three or four terms of (23) for $n = 0$ to obtain a quadratic equation for η^2 that can be solved explicitly. However, we retain only the first three and work with

$$f_0 \approx 24wM_2 = (1-w)^4/(1+2w)^2 - 1 \equiv \mathcal{N} - 1,$$

$$\mathcal{N}_0 = 12wM_1/x - 8w\mathcal{M}_3/[(\eta^2 - 1) + 4] \quad (25)$$

$$\equiv Q - T/[(\eta^2 - 1) + 4],$$

where \mathcal{N} is the low-frequency limit of the structure factor. [We rewrote $\eta^2 + 3$ to make $\eta^2 - 1$ explicit, but will drop the 4 (and could drop the -1), which contributes negligibly.]

In terms of (25), \mathcal{N}_0 of (24) reduces to

$$\begin{aligned} \mathcal{N}_0 &\approx -[\mathcal{N} + i\Gamma - iT(\eta^2 - 1)]^{-1}, \\ \Gamma &= \gamma + Q - 4T \approx \gamma + Q \\ &\approx [x_0^2 - x^2(1 - 12wM_1)]/x^4, \end{aligned} \quad (26)$$

and, consequently,

$$\eta^2 - 1 = iS/[\mathcal{N} + i\Gamma - iT(\eta^2 - 1)]. \quad (27)$$

The relevant root of the quadratic for $\eta^2 - 1$ equals

$$\begin{aligned} \eta^2 - 1 &= \{\mathcal{N} + i\Gamma - [(\mathcal{N} + i\Gamma)^2 + 4ST]^{1/2}\}/2iT \\ &= 2iS/[\mathcal{N} + i\Gamma + \{(\mathcal{N} + i\Gamma)^2 + 4ST\}^{1/2}], \end{aligned} \quad (28)$$

where the final form of $\eta^2 = R + iI$ is more suggestive of the oscillator structure. To include the $\delta\tilde{M}_4$ term of f_0 , we replace \mathcal{N} by $\mathcal{N} + 2V$ and T by $T + iV$ with $V = 16x^2M_4$; however, the effects of V are minor in the range of x and w where (28) suffices. We cite (28) as (M) in the following.

For $x \approx 0$, we now have⁴

$$\begin{aligned} R &\approx 1 + w(C' - 1), \quad I \approx w\mathcal{N}(C' - 1)^2 x^3, \\ C_1 &\equiv R + iI, \end{aligned} \quad (29)$$

which differs from (9) in that $\mathcal{N}(w) = (1-w)^4/(1+2w)^2$ shows the decrease of scattering losses arising from increasing w and increasing correlations (decreasing fluctuations). Instead of increasing linearly with increasing w at fixed x , the present I increases to a maximum at $w \approx 0.129$ (where $w\mathcal{N} \approx 0.0469$), and then decreases.⁴ For the physically unrealizable bound $w = 1$, we have $\mathcal{N}(1) = 0$ and C_1 reduces to C' as required for a uniform medium.

Similarly the value of I of (28) corresponding to the resonance condition $\Gamma = 0$, i.e.,

$$\begin{aligned} I_\Lambda &= 2S/[\mathcal{N} + (\mathcal{N}^2 + 4ST)^{1/2}], \\ 4ST &= 96w^3M_3/x^2, \end{aligned}$$

$$x = x_\Lambda = x_0/(1 - 12wM_1)^{1/2} > x_0, \quad (30)$$

is smaller than the uncorrelated value $I_0 = S(x_0) = 3w/x_0^3$. Even at $w = 1\%$, where $x_\Lambda = 0.01443$ is about 3% larger than $x_0 = 0.014$, $I_\Lambda \approx 4520$ is only about 41% of $I_0 \approx 10933$. At $w = 0.04$, $x_\Lambda \approx 0.01586$ is about 13% larger than x_0 , and $I_\Lambda \approx 4718$ is about 11% of $I_0 \approx 43732$.

To help clarify the relation of (28) to the uncorrelated form, we write $(\mathcal{N} + i\Gamma)^2 + 4ST = U^2 + i2\Gamma\mathcal{N}$ and expand the square root for $2\Gamma\mathcal{N} \ll U^2$ to obtain

$$\begin{aligned} \eta^2 - 1 &\approx \frac{i2S}{(\mathcal{N} + U)(1 + i\Gamma/U)} \equiv \frac{iP}{1 + i\delta}, \\ U &= (\mathcal{N}^2 + 4ST - \Gamma^2)^{1/2}. \end{aligned} \quad (31)$$

This form reproduces (30) for $\Gamma = 0$; it suffices in the neighborhood of $x = x_\Lambda$ for small $\delta = \Gamma/U$, and indicates trends

at $\delta^2 = 1$. Thus, from $\Gamma^2 = U^2$, we have $\Gamma = \pm (2ST + \mathcal{W}^2/2)^{1/2} = \pm U$,

$$x_{\pm} \approx x_{\lambda} \pm x_{\lambda}^2 (2S_{\lambda} T_{\lambda} + \mathcal{W}^2/2)^{1/2} / 2(1 - 12w|M_1|),$$

$$\eta^2 - 1 = \frac{P_{\pm}}{2} (\mp 1 + i)$$

$$= \frac{S_{\pm} (\mp 1 + i)}{\mathcal{W} + (2S_{\pm} T_{\pm} + \mathcal{W}^2/2)^{1/2}} = R_{\pm} + iI_{\pm}, \quad (32)$$

where $S_{\lambda} = S(x_{\lambda})$, $S_{\pm} = S(x_{\pm})$, etc. For $w = 1\%$, we have $R_{-} \approx 3057$ at $x_{-} \approx 0.01416$ and $R_{+} = -2833$ at $x_{+} = 0.0147$; the extrema obtained from (28) are $R_{\lambda} = 3290$ at $x = 0.0141$ and $R_{\nu} \approx -2933$ at $x = 0.0148$. The corresponding values $I_{\pm} = \mp R_{\pm}$ are larger than $I_{\lambda}/2 = 2260$.

For very small w , (28) reduces to (5), but with increasing w the asymmetry of the oscillator at hand becomes more pronounced; see curves in Figs. 1-3. In Fig. 3 at $w = 4\%$, the chain-dot curves for the correlated cases based on $10(M)$ of (15) practically overlay $(M1)$ of (28); in Figs. 1 and 2, the correlated curves correspond to both $10(M)$ and $(M1)$, but the cases are indistinguishable.

For $w > 4\%$, the curves in Fig. 3 based on $10(MD)$ of (16) indicate that the dipoles (a_1) should be included. The decrease in bulk density (the real part of $\rho \approx B^{-1}$) with increasing w arises from the effects of dipoles, and other effects arise from cross coupling with monopoles.

Were the monopole-dipole coupling terms in (16) involving \mathcal{W}_1 negligible, then, as shown before,⁴

$$\frac{1}{\rho} = 1 + iS_{\lambda}/\rho \approx 1 - \frac{3iS}{1 + f_{\alpha} + i(\gamma_1 + S)}$$

$$= 1 + \frac{3wt}{1 - wt + i\mathcal{W}/x^{1/3}},$$

$$t \equiv (1 - \rho')/(1 + 2\rho') \quad (33)$$

[where (33) retains only the leading real and imaginary parts of the denominator of \mathcal{A}_1] gives the correct leading real and imaginary parts of

$$\rho \approx (1 - wt)/(1 + 2wt) + i[w\mathcal{W}/x^{1/3}/(1 + 2wt)^2] \equiv \rho_1. \quad (34)$$

For the physically unrealizable bound $w = 1$, we have $\rho_1 = \rho'$ as required. Similarly, from (29) and (34), $C_1\rho_1 = \eta_1^2$, in which we retain only terms to $(x')^{-1}$, reduces to $C'\rho' = \eta'^2$ at $w = 1$. Since C' dominates, we may use

$$\eta_1^2 = C_1 \text{Re} \rho_1, \quad \text{Re} \rho_1 = (1 - wt)/(1 + 2wt) \quad (35)$$

to obtain the corresponding η , and η , for very low-frequency applications. Discounting large values of w for the case $\rho' = 1/825$ at hand, we have $t \approx 1$ and

$$\rho_1 \approx \tilde{\rho} + i[w\mathcal{W}/x^{1/3}/(1 + 2w)^2], \quad \tilde{\rho} \equiv (1 - w)/(1 + 2w). \quad (36)$$

We retain only $\tilde{\rho}$ in the following

More generally, however, the monopole-dipole coupling terms in \mathcal{W}_1 cannot be neglected. To generalize (28) to include leading dipole effects, we rewrite (16) as⁴

$$\eta^2 = (1 - iS_{\lambda}/\rho)/D,$$

$$D \equiv 1 + iS_{\lambda}/\rho \{1 + \mathcal{A}_0 [2h_{01} - (\eta^2 - 1)h_{01}^2/iS]\}. \quad (37)$$

Using the x -independent approximation $iS_{\lambda}/\rho \approx 3w/(1 - w)$, and replacing $h_{01} = \mathcal{W}_1/\eta$ by its leading term $i4w|M_1|/x = iQ/3$, yields

$$D = 1 + \frac{3w}{1 - w} \left[1 + \mathcal{A}_0 \left(\frac{2iQ}{3} - i \frac{(\eta^2 - 1)x^2 Q^2}{27w} \right) \right]$$

$$= \frac{1 - 2w}{1 - w} \left[1 + i \frac{\mathcal{A}_0}{1 + 2w} \left(2wQ - (\eta^2 - 1) \frac{x^2 Q^2}{9} \right) \right]. \quad (38)$$

Thus (37) reduces to

$$\eta^2 = \frac{\tilde{\rho}(1 - iS_{\lambda}/\rho)}{1 + iS_{\lambda}/\rho [2wQ - (\eta^2 - 1)x^2 Q^2/9]/(1 + 2w)}. \quad (39)$$

Substituting \mathcal{A}_0 of (26) into (39), and subtracting $\tilde{\rho}$ from each side of the equation, we approximate the numerator by its x^{-1} term and write the result as

$$\eta^2 - \tilde{\rho} \approx \frac{iS_1}{\mathcal{W} + i\Gamma_1 + iT_1(\eta^2 - 1)}$$

$$\approx \frac{iS_1}{\mathcal{W} + i\Gamma_1 + iT_1(\eta^2 - \tilde{\rho})}, \quad (40)$$

where

$$S_1 = S\tilde{\rho} = 3w(1 - w)/x^3(1 + 2w),$$

$$\Gamma_1 = \Gamma - \frac{2wQ}{1 + 2w} = \gamma + \frac{Q}{1 + 2w} = \gamma + \frac{12w|M_1|}{x(1 + 2w)},$$

and

$$T_1 = T - x^2 Q^2/9(1 + 2w)$$

$$= 8xw[|M_1| - 2w|M_1|^2/(1 + 2w)].$$

Since (40) is the same form as (27), it follows that

$$\eta^2 - \tilde{\rho} \approx 2iS_1/[\mathcal{W} + i\Gamma_1 + \{(\mathcal{W} + i\Gamma_1)^2 + 4S_1 T_1 \}^{1/2}]. \quad (41)$$

which suffices for a much larger range of w than (28). This first approximation ($MD1$) is used to construct the three-dimensional plots in Figs. 11-14.

Had we dropped the term "1" in the parentheses of the numerator of (39) and replaced $\eta^2 - 1$ by η^2 in the denominator, then we would have obtained (41) with $\eta^2 - \tilde{\rho}$ replaced by η^2 (which suffices for our primary purpose). However, (41) as it stands reduces to $\eta^2 \approx \tilde{\rho}C_1$ for $x \approx 0$, and provides a check. To delineate the dipole effects more explicitly, we would start with $iS_{\lambda}/\rho \approx 3wt/(1 - wt)$ based on (33), which leads to (39) with $\tilde{\rho}$ replaced by $\text{Re} \rho_1$ of (35), and $(1 + 2w)^{-1}$ replaced by $(1 + 2wt)^{-1}$. Then (40) and (41) would involve $\text{Re} \rho_1$ instead of $\tilde{\rho}$, the final form of Γ_1 would contain $(1 + 2wt)^{-1}$ instead of $(1 + 2w)^{-1}$, and T_1 would contain $2wt(1 + 2wt)^{-1}$ instead of $2w(1 + 2w)^{-1}$.

Although we could obtain more complete approximations than (41) by using it in an iteration procedure for (37), this explicit first approximation ($MD1$) is in good accord with $10(MD)$ to $w = 7.5\%$, and suffices at least qualitatively for larger w . See dashed curves (where perceptible) in Figs. 3-10, in which $10(MD)$ and $10(MDQ)$ are represented

by solid and dotted curves, respectively. Computations based on (MD 1) involve only pocket-calculator routines, and for various practical purposes we would use (MD 1) instead of 10(MD) or even 10(MDQ) to at least $w = 10\%$. The figures show that in some ranges (MD 1) is fortuitously closer to 10(MDQ) than to 10(MD).

At resonance, $\Gamma_1 = 0$ and $\text{Im}(\eta^2 - \bar{p})$ reduces to

$$I_\lambda = \frac{2S_1}{\eta^2 + (\eta^2 + 4S_1 T_1)^{1/2}},$$

$$x_\lambda^2 = \frac{x_0^2}{1 - 12w|M_1|/(1 + 2w)} > x_0^2, \quad (42)$$

where the present I_λ is larger and x_λ is smaller than the corresponding (M 1) results based on (30) for the pure monopole case. The present analog of (31),

$$\eta^2 - \rho \approx \frac{i2S_1}{(\eta^2 + U_1)(1 + i\Gamma_1/U_1)} = \frac{iP_1}{1 + i\delta_1},$$

$$U_1 = (\eta^2 + 4S_1 T_1 - \Gamma_1^2)^{1/2}, \quad (43)$$

is sufficient for a relatively smaller range in the neighborhood of $x = x_\lambda$, i.e., for relatively small values of $\delta_1 = \Gamma_1/U_1$.

V. NUMERICAL AND SYMBOLIC PROCEDURES

Both symbolic and numerical procedures were used to solve the integral equations (15)–(17) in terms of the integrals (13) for $\mathcal{Y}_\lambda(\eta)$ based on the PY correlation function F . The coefficients for the eight shells (which provide the exact F for $r < 9$) and the first 20 moments $M_n(w)$ were obtained symbolically, and stored in the machine.

The shell approximations $S(M)$ of (15) and $S(MD)$ of (16) were computed by truncating the integrals (13) at $r = 9$, and using a 48-point Gauss integration formula in each of the shells. We solved the numerical integral equations for η at fixed values of $w < 0.20$ using Müller's method (IMSL 9.2 routine ZANLYT) by starting at $x = 0.001$ and progressing to $x = 0.1$ in 1000 steps. The numerical procedure was robust for $w < 0.075$. The solutions were not dependent on perturbations of the initial value of η at $x = 0.001$; i.e., we could start with the uncorrelated value or with the value of an explicit approximation (M 1) or (MD 1), stay on the same solution branch, and get identical results through $x = 0.1$. For $w > 0.075$, after starting with an initial value (M 1 or MD 1), we used a polynomial extrapolation of $\text{Re } \eta$ and $\text{Im } \eta$ based on values of η at four successive steps in x , as the initial guess to compute η at the next step in x . This procedure was stable and insensitive to small perturbations in the starting values at $x = 0.001$ for w up to about 0.12, and sufficed for computations to $x = 0.1$. However, for $0.125 \leq w < 0.2$, it sufficed for computations only for $x \leq x_m$, with x_m as the value of x where $\text{Im } \eta$ reached its maximum; for larger x , the corresponding curves behaved erratically. (Initially we sought to compute with only the available five-shell approximation,⁹ but instabilities were present for $w > 0.07$.)

Müller's method was also used for computations of (15) to (17) based on the moment expansions¹⁰ of F , but numerical integration was not involved. Using symbolic methods,

the spherical functions in the integrand of \mathcal{Y}_λ were expanded and regrouped as polynomials in r , the integrals in r were identified as moments M_n , and the result was regrouped as a polynomial in η^2 . The order of the highest moment and the highest multipole retained determined a polynomial equation for η^2 , and the algebraic equation was then solved numerically over the domain $0.001 \leq x < 0.1$ (at 1000 steps) and $0 \leq w < 0.20$. If more than the first ten moments were retained, extended precision was used. The computation was robust for $w < 0.20$; perturbations in the starting values did not change the branch of the solution to the polynomial in η^2 , and it was not necessary to use extrapolation techniques to stay on the stable branch. The solution is the only one in the neighborhood of the corresponding shell solution for $w < 0.12$ to $x = 0.1$, and for larger w to $x \approx x_m$. Our most elaborate computations, involving the first 20 moments and the first three multipole coefficients of the sphere, posed no special problems (but required more time). For the construction of the log-log plots in Figs. 7–10, we extended the domain to $x = 0.20$.

Both of the above computational procedures were based on the complete multipole coefficients as in (1) and (2). On the other hand, for the explicit approximations M 1 as in (28) and MD 1 as in (41), we used only the leading terms based on (4). Computations for M 1 and MD 1 can be done on a pocket calculator.

ACKNOWLEDGMENT

This work was supported in part by the Office of Naval Research.

APPENDIX A: SYMBOLIC¹² PROGRAM TO COMPUTE THE PY MOMENTS

```
FOR ALL m, w LET
  E(w,m) = -(4 + 2*m + (m - 1)*w)/
    (2*(m + 1)*(m + 2)*(m + 3)),
  L(w,m) = -(2*m + (m - 3)*w)/(2*m*(m + 1)),

Procedure Fact(N);
  Begin
    Scalar M;
    M := 1;
    L: If N = 0 then Return M;
    M := M*N; N := N - 1;
    Go to L;
  End;

Procedure CC(I,J);
  Begin
    Return Fact(I)/(Fact(I - J)*Fact(J)),
  End;

Nmax. = 20, Llength 60, Off Exp, on Gcd,
For I := 1 Step 1 Until Nmax do
  Begin
    A := For J := 1 Step 1 Until I - 1
      Sum <- CC(I - 1,J)*E(w,I)*M(w,I - J) > >;
    M(w,I) := (1/(1 + 2*w))*L(w,I)
```

$$+ 12w * E(w, I + 1) / (I * (I + 1))$$

$$+ 12w * A;$$

On Factor;

ans: = M(w, I); Write "(", I, ") = ";

Write ans; Off Factor;

End;

Quit;

APPENDIX B: COEFFICIENTS OF THE FIRST EIGHT PY SHELLS

As discussed by Wertheim,⁸ $F(r) = f(r) - 1$ can be obtained in closed form for given r from the inverse Laplace transform

$$rf(r) = \mathcal{L}^{-1}\{tL(t)/[12wL(t) + S(t)e^t]\},$$

$$S(t) = (1-w)^2 t^3 + 6w(1-w)t^2$$

$$+ 18w^2 t - 12w(1-w),$$

$$L(t) = (1+w/2)t + 1 + 12w,$$

by expanding the operand in powers of S^{-1} and evaluating the residues at the roots ($t_0 = t_0, t_1, t_2 = t_1^*$) of $S(t)$. The roots may be written as⁹

$$t_1 = [-2w + (2wq)^{1/3} (Y_+ J^1$$

$$+ Y_- J^{-1}) / (1-w),$$

$$q = 3 + 3w - w^3, \quad J = \exp(2\pi i/3),$$

$$Y_{\pm} = [1 \pm \sqrt{1 + 2(w^2/q)^2}]^{1/3}.$$

Thus, for $1 < r \leq 1$,

$$f(r) = \sum_{j=1}^3 f_m(r),$$

such that $f_m(r) = 0$ for $r < m$, and for $r > m$,

$$rf_m(r) = \frac{(-12w)^{m-1}}{(m-1)!} \sum_{l=0}^2 \lim_{t \rightarrow t_l} \frac{d^{m-1}}{dt^{m-1}} \times \{(t-t_l)^m t \{L(t)/S(t)\}^m e^{t(r-m)}\},$$

where $f_m(m) = 0$ for $m > 1$. The results may be expressed as

$$rf_m(r) = \sum_{l=0}^2 C_l(m, 0) e^{t_l(r-m)} \\ \times \sum_{k=1}^m C_l(m, k) (r-m)^{k-1}.$$

Forms of the coefficients for $1 \leq m \leq 5$ are given by Smith and Henderson,⁹ whose notation we follow in essentials.

The coefficients $C(m, k)$ are listed sequentially for the first eight shells ($m = 1-8$); these serve to construct $f(r)$ for $1 \leq r \leq 9$. The entries through $C(5, 5)$ are equivalent to those of Ref. 9. The symbols needed to construct the sets of C 's for particular shells are defined in advance. The C 's are to be evaluated at the three roots $t = t_l$ of S , but the l is suppressed in the following:

$$A = L/S_1,$$

$$S_1 = 3(1-w)^2 t^2 + 12w(1-w)t + 18w^2,$$

$$S_2 = 6(1-w)^2 t + 12w(1-w), \quad S_3 = 6(1-w)^2,$$

$$L_1 = (1 + w/2),$$

$$C(1, 0) = 1, \quad C(1, 1) = tA,$$

$$C(2, 0) = -12wA/S_1, \quad C(2, 1) = -tS_2A + 2tL_1 + L, \quad C(2, 2) = tL,$$

$$C(3, 0) = 72w^2A/S_1^2, \quad C(3, 1) = A^2 t(3S_2^2 - S_1S_3) - 3AS_2(L + 3tL_1) + 6L_1(L + tL_1),$$

$$C(3, 2) = [6tL_1 + L(2 - 3tS_2/S_1)]L, \quad C(3, 3) = tL^2,$$

$$D_1 = 15S_2^2 - 4S_1S_3, \quad D_2 = L + 4tL_1, \quad D_3 = AS_2,$$

$$D_4 = 7L + 3tL_1,$$

$$C(4, 0) = -288w^3A/S_1^3,$$

$$C(4, 1) = 5tA^3S_2(2S_1S_3 - 3S_2^2) + A^2D_1D_2 - 24L_1D_3D_4 + 12L_1^2(3L + 2tL_1),$$

$$C(4, 2) = [tA^2D_1 - 12(D_2D_3 - L_1D_4)]L,$$

$$C(4, 3) = (3D_2 - 6tD_3)L^2, \quad C(4, 4) = L^3,$$

$$E_1 = 7S_2t - 4S_1,$$

$$E_2 = 3E_1S_1S_2S_3 - 2S_2^2S_1^2t - 21S_1^2t + 21S_2^2S_1,$$

$$E_3 = 3S_2t - S_1, \quad E_4 = 4E_1S_1S_3 - 21S_1^2t + 18S_2^2S_1,$$

$$E_5 = 2S_1S_3t - 9S_2^2t + 6S_2S_1, \quad E_6 = 5S_2t - 2S_1,$$

$$C(5, 0) = -864Aw^4/S_1^4,$$

$$C(5, 1) = 5(E_2A^4 - 5E_4A^3L_1 + 20E_6A^2L_1^2 + 24E_6L_1^3 - 24tL_1^4),$$

$$C(5, 2) = -5(E_4A^3 - 10E_6A^2L_1 - 24E_6AL_1^2 + 48tL_1^3)L,$$

$$C(5, 3) = 5(E_6A^2 + 6E_6AL_1 - 24tL_1^2)L^2,$$

$$C(5,4) = 2(E_0 A - 10L_1)L^3, \quad C(5,5) = -L^4 t,$$

$$F_1 = 27S_2^2 t - 27S_2^4 S_1 - 36S_2^2 S_3 S_1 t + 24S_2^2 S_3 S_1^2 + 8S_2 S_3^2 S_1^2 t - 2S_3^2 S_1^3,$$

$$F_2 = 27S_2^2 t - 24S_2^2 S_1 - 24S_2^2 S_3 S_1 t + 12S_2 S_3 S_1^2 + 2S_3^2 S_1^2 t,$$

$$F_3 = 28S_2^2 t - 21S_2^2 S_1 - 14S_2 S_3 S_1 t + 4S_3 S_1^2,$$

$$F_4 = 21S_2^2 t - 12S_2 S_1 - 4S_3 S_1 t, \quad F_5 = 3S_2 t - S_1,$$

$$C(6,0) = 10368Aw^5/(5S_1^5),$$

$$C(6,1) = 5(7F_1 A^5 - 42F_2 A^4 L_1 - 120F_3 A^3 L_1^2 + 90F_4 A^2 L_1^3 + 360F_5 A L_1^4 - 144L_1^5 t),$$

$$C(6,2) = -5(7F_2 A^4 - 36F_3 A^3 L_1 + 90F_4 A^2 L_1^2 - 480F_5 A L_1^3 + 360L_1^4 t)L,$$

$$C(6,3) = 15(F_3 A^3 - 6F_4 A^2 L_1 + 60F_5 A L_1^2 - 80L_1^3 t)L^2,$$

$$C(6,4) = -5(F_4 A^2 - 24F_5 A L_1 + 60L_1^2 t)L^3,$$

$$C(6,5) = 5(F_5 A - 6L_1 t)L^4, \quad C(6,6) = -L^5 t,$$

$$G_1 = 8S_1^2 S_1^3 - 180S_1^2 S_2^2 S_1^2 + 495S_1 S_2 S_2^2 - 297S_2^3,$$

$$G_2 = G_1 t + 72S_1^2 S_2^2 S_1 - 360S_1^2 S_2 S_1^2 + 297S_1 S_2^2,$$

$$G_3 = 8S_1^2 S_2^2 - 108S_1 S_2 S_2^2 + 135S_2^3,$$

$$G_4 = 4S_1 S_2 - 9S_2^2, \quad G_5 = G_1 t + 12G_2 S_1 S_2,$$

$$G_6 = S_1 S_2 - 6S_2^2, \quad G_7 = G_4 t S_2 - G_6 S_1,$$

$$G_8 = G_6 t + 3S_1 S_2,$$

$$G_9 = 72S_1^2 S_2^2 S_1 - 360S_1 S_2 S_2^2 + 297S_2^3 - 16S_1^2 S_2^2 + 216S_1^2 S_2 S_1^2 - 270S_1 S_2^2,$$

$$G_{10} = 7tS_2 - 2S_1,$$

$$C(7,0) = -20736Aw^6/(5S_1^6),$$

$$C(7,1) = 35(G_2 A^6 + 7G_3 A^5 L_1 - 42G_4 A^4 L_1^2 - 840G_5 A^3 L_1^3$$

$$+ 840G_6 A^2 L_1^4 + 216G_{10} A L_1^5 - 144L_1^6 t),$$

$$C(7,2) = -35(-G_3 A^5 + 14G_4 A^4 L_1 + 504G_5 A^3 L_1^2 - 840G_6 A^2 L_1^3 - 360G_{10} A L_1^4 + 432L_1^5 t)L,$$

$$C(7,3) = -35(G_4 A^4 + 84G_5 A^3 L_1 - 252G_6 A^2 L_1^2 - 180G_{10} A L_1^3 + 360L_1^4 t)L^2,$$

$$C(7,4) = -140(G_5 A^3 - 7G_6 A^2 L_1 - 9G_{10} A L_1^2 + 30L_1^3 t)L^3,$$

$$C(7,5) = 35(G_6 A^2 + 3G_{10} A L_1 + 18L_1^2 t)L^4,$$

$$C(7,6) = 3(G_{10} A - 14L_1 t)L^5, \quad C(7,7) = -L^6 t,$$

$$H_1 = 9S_2 + 2tS_1, \quad H_2 = 3S_2 + 2tS_1,$$

$$H_3 = S_2 + 2tS_1,$$

$$H_4 = 220H_1 S_1^2 S_2^2 - 1980H_2 S_1^2 S_2^2 S_1 + 3861H_3 S_1 S_2^2 - 80S_1^2 S_2^2 - 3861S_2^2 t,$$

$$H_5 = 9S_2 + tS_1, \quad H_6 = 3S_2 + 5tS_1,$$

$$H_7 = 2S_2 + tS_1,$$

$$H_8 = 80H_1 S_1^2 S_2^2 + 1188H_2 S_1 S_2^2 - 1980H_3 S_1^2 S_2 - 3861S_2^2 t,$$

$$H_9 = 6S_2 + tS_1, \quad H_{10} = S_2 + tS_1,$$

$$H_{11} = 8H_2 S_1^2 S_2 - 120H_{10} S_1 S_2^2 + 165S_2^2 t,$$

$$H_{12} = 3S_2 + 4tS_1, \quad H_{13} = 3S_2 + tS_1,$$

$$H_{14} = 55H_{12} S_1 S_2^2 - 40H_{13} S_1^2 S_2 S_1 + 8S_1^2 S_2^2 - 198S_2^2 t,$$

$$H_{15} = 9H_2 S_1 S_2 - 4S_1^2 S_2 - 45S_2^2 t,$$

$$H_{16} = 4H_{15} S_1 - 27S_2^2 t, \quad H_{17} = S_1 - 4S_2 t,$$

$$C(8,0) = 248832Aw^7/(35S_1^7),$$

$$C(8,1) = -35(H_4 A^7 - 8H_5 A^6 L_1 + 504H_{13} A^5 L_1^2 + 1008H_{14} A^4 L_1^3 + 3360H_{15} A^3 L_1^4$$

$$- 2688H_{16} A^2 L_1^5 + 4032H_{17} A L_1^6 + 1152L_1^7 t),$$

$$C(8,2) = 35(H_5 A^6 - 144H_{14} A^5 L_1 - 504H_{15} A^4 L_1^2$$

$$- 2688H_{16} A^3 L_1^3 + 3360H_{17} A^2 L_1^4 - 8064H_{17} A L_1^5 - 4032L_1^6 t)L,$$

$$\begin{aligned}
C(8,3) &= -105(3H_{14}A^3 + 24H_{11}A^4L_1 + 224H_{13}A^3L_1^2 \\
&\quad - 448H_{10}A^2L_1^3 + 1680H_{17}AL_1^4 + 1344iL_1^5)L^2, \\
C(8,4) &= -35(3H_{11}A^4 + 64H_{13}A^3L_1 - 224H_{10}A^2L_1^2 \\
&\quad + 1344H_{17}AL_1^3 + 1680iL_1^4)L^3, \\
C(8,5) &= -70(H_{15}A^3 - 8H_{16}A^2L_1 + 84H_{17}AL_1^2 + 168iL_1^3)L^4, \\
C(8,6) &= 14(H_{16}A^2 - 24H_{17}AL_1 - 84iL_1^2)L^5, \\
C(8,7) &= \frac{1}{2}7(H_{17}A + 8iL_1)L^6, \quad C(8,8) = -L^7i.
\end{aligned}$$

¹ L. L. Foldy, "The multiple scattering of waves," *Phys. Rev.* **67** (2), 107-119 (1954).

² L. Spitzer, Jr., "Acoustic properties of gas bubbles in a liquid," NDRC Rep. No. 6.1-sr-20-918 (1943). Acoustic theory of bubbles, in *Physics of Sound in the Sea*, edited by R. Wildt (U.S. Navy, Washington, DC, 1946), NDRC Summary Tech. Rep. Div. 6, Vol. 8, Part 4, Chap. 28.

³ K. W. Commander and A. Prosperetti, "Linear pressure waves in bubbly liquids: Comparisons between theory and experiments," *J. Acoust. Soc. Am.* **85**, 732-746 (1989).

⁴ V. Twersky, "Acoustic bulk parameters in distributions of pair-correlated scatterers," *J. Acoust. Soc. Am.* **64**, 1710-1719 (1978).

⁵ V. Twersky, "Coherent scalar field in pair-correlated random distributions of aligned scatterers," *J. Math. Phys.* **18**, 2468-2486 (1977). Equation (154), a homogeneous algebraic system, is reduced to the inhomogeneous system (89), reproduced by the present (12), in order to facilitate physical interpretation and computations.

⁶ G. C. Gaunaud and H. Ueberall, "Resonance theory of bubbly liquids," *J. Acoust. Soc. Am.* **69**, 362-370 (1981).

⁷ J. K. Percus and G. J. Yevick, "Analysis of classical statistical mechanics by means of collective coordinates," *Phys. Rev.* **110**, 1-13 (1958).

⁸ M. S. Wertheim, "Exact solution of the Percus-Yevick integral equation for hard spheres," *Phys. Rev. Lett.* **10**, 321-323 (1963).

⁹ W. R. Smith and D. Henderson, "Analytical representation of the Percus-Yevick hard-sphere radial distribution function," *Mol. Phys.* **19**, 411-415 (1970); D. Henderson and W. R. Smith, *J. Stat. Phys.* **19**, 191-200 (1978).

¹⁰ N. E. Berger and V. Twersky, "Moments of the Percus-Yevick hard sphere correlation function," to appear in *J. Stat. Phys.* **61**, 1189-1203 (1990).

¹¹ M_L is given in H. D. Jones, *J. Chem. Phys.* **55**, 2640-2642 (1971), and M_L

in Ref. 9 (1970), M_L may be obtained from I. Nezbeda, *Czech J. Phys B* **24**, 55-62 (1974).

¹² RI DUCI, Version 3.2, Rand Corporation, Santa Monica, CA (1985).

¹³ M. Lax, "Multiple scattering of waves," *Rev. Mod. Phys.* **23**, 287-310 (1951); "The effective field in dense systems," *Phys. Rev.* **88** (2), 621-629 (1952).

¹⁴ J. G. Kirkwood, "Statistical mechanics of fluid mixtures," *J. Chem. Phys.* **3**, 300-313 (1935).

¹⁵ V. Twersky, "Transparency of pair-correlated, random distributions of small scatterers with applications to the concha," *J. Opt. Soc. Am.* **65**, 524-530 (1975).

¹⁶ H. Reiss, H. L. Frisch, and J. L. Lebowitz, "Statistical mechanics of rigid spheres," *J. Chem. Phys.* **31**, 369-380 (1959).

¹⁷ V. Twersky, "Wavelength dependent bulk parameters for coherent sound in correlated distributions of small spaced scatterers," *J. Acoust. Soc. Am.* **77**, 29-37 (1985).

¹⁸ L. Tsang, J. A. Kong, and T. Habashy, "Multiple scattering of acoustical waves by random distributions of discrete spherical scatterers with quasi-crystalline and Percus-Yevick approximation," *J. Acoust. Soc. Am.* **71**, 552-558 (1982). Their (14), equivalent to (154) of Ref. 5, is used for three-shell numerical computations and physical parameters that represent typical values encountered in ultrasonic probing of the granular structure of rocks.

¹⁹ Y. Ma, V. K. Varadan, and V. V. Varadan, "Application of Twersky's multiple scattering formalism to a dense suspension of elastic particles in water," *J. Acoust. Soc. Am.* **75**, 335-339 (1984). We surmise that their numerical computations were based on Henderson's four-shell program for a modified PY function reproduced by D. A. McQuarrie, *Statistical Mechanics* (Harper and Row, New York, 1976), pp. 600-603.

Polydisperse scattering theory and comparisons with data for red blood cells

N E. Berger, R J. Lucas,^{*)} and V. Twersky
Mathematics Department, University of Illinois, Chicago, Illinois 60680

(Received 15 May 1990; accepted for publication 15 November 1990)

Recent results for low-frequency scattering by polydisperse distributions of correlated low-refracting particles averaged over orientation are analyzed numerically. The roles of shape and correlations (parameterized by c) and polydispersity (specified by the normalized variance d in size governed by the gamma probability density) are investigated. The key variable is the net volume fraction w occupied by the particles. The incoherent scattering is determined by $\Delta = PS(c,d,w)$ with P as a particle population factor that is independent of w , and S as the fluctuation-correlation function of w . Earlier applications of monodisperse ($d=0$) theory emphasized the influence of c on the peak $\Delta = \Delta_\lambda$ and its location $w = w_\lambda$ in order to invert ultrasonic scattering data of Shung and his associates for red blood cell suspensions under different flow conditions. For $d>0$, comparable curves for $\Delta(w)$ decrease more gradually with w increasing past w_λ (because of additional scattering arising from polydispersity) and thereby provide better fits to data for the more controlled flows over broader ranges of hematocrit.

PACS numbers: 43.80.Ev, 43.35.Bf

INTRODUCTION

The low-frequency incoherent scattering (proportional to $\Delta = PS$) for correlated distributions of randomly oriented low-refracting particles depends on a population factor (P) and on a fluctuation-correlation function (S) of the volume fraction (w) occupied by the particles. A recent article¹ generalized earlier results² for identical particles (with shape and correlations parameterized by c) to mixtures of differently sized particles by applying scaled particle statistical mechanics theory^{3,4} for the corresponding isotropic fluids of hard convex particles. For a continuous (polydisperse) distribution in the size variable (R) with normalized variance d (based on the gamma probability density) the resulting Δ is specified by a simple explicit form $S(c,d,w)$, a rational function of the net volume fraction w . The population factor P , based on Rayleigh's results⁵ for a low-refracting particle, is independent of w .

Our earlier heuristic applications of monodisperse ($d=0$) theory to invert data records of Shung⁶ and his associates for scattering of ultrasound by red blood cells (RBC) versus hematocrit (w) under different flow conditions, emphasized the influence of c on the peak $\Delta = \Delta_\lambda$ and its location $w = w_\lambda$. We obtained⁷ good accord with major data trends of the more controlled flow processes for $0 < w \leq w_\lambda + 0.1$, but in general the curves were below the data points at larger w . The increase of the discrepancy with increasing w for uniform flow could arise from an additional fluctuation mechanism leading to additional scattering, and

motivated the present heuristic applications of polydisperse theory.¹ For $d>0$ comparable curves $\Delta(w)$ based on $S(c,d,w)$ decrease more gradually for w increasing past w_λ , and the systematic discrepancies for uniform flow noted earlier⁷ are reduced by taking polydispersity of cell size into account. We use nonlinear least-squares⁸ fits for data records versus w to isolate effective values of the parameters, and compare the resulting curves with the original data records.⁶

In the following, for brevity, we write Fig. 6.4 for Fig. 4 of Ref. 6, etc. Section I includes key forms for three-, two-, and one-dimensional scattering problems with a view to bioacoustical applications to distributions of cells, aligned fibers, and parallel tissues. To emphasize essential features and indicate restrictions, we sketch the evolution of the present S by comparing the original result for correlated identical spheres,⁹ the extension to identical nonspherical particles² averaged over orientation, and the recent generalization¹ to mixtures of similarly shaped but differently sized particles. Section II specializes the mixture results to polydisperse (continuous) distributions in size governed by the gamma probability density function^{10,11} with skewness determined by the normalized variance d (as illustrated in Fig. 1). Key features of $S(c,d,w)$ are displayed in Figs. 2 to 7 for three- and two-dimensional problems. Figure 8 illustrates that the same values of Δ_λ and w_λ can arise for different curves generated by different sets of values $\{P,c,d\}$. Section III applies least-squares procedures to obtain effective values of $\{P,c,d\}$ from the RBC data records.⁶ Figures 9 to 12 overlay the resulting PS curves (shown solid), and the earlier monodisperse curves⁷ (shown dashed) obtained by emphasizing data near w_λ , as well as monodisperse least-squares curves (shown dotted), on all data records given in Ref. 6.

^{*)} Visiting from the Department of Mathematical Sciences, Loyola University, Chicago, IL.

I. KEY FORMS

The low-frequency differential scattering cross section of a particle with acoustic parameters close to those of the embedding medium may be written in $\{1,2,3\}$ dimensions as^{5,2}

$$\sigma(\theta) = pv^2, \\ p = |C' - 1 - (B' - 1)\cos\theta|^2 \left\{ \frac{k^2}{4}, \frac{k^1}{8\pi}, \frac{k^3}{16\pi^2} \right\}. \quad (1)$$

Here θ is measured from the direction of incidence, and v = {width, area, volume}. The relative parameters C' and B' (compressibility and inverse mass density for the simplest cases) are complex in general. For radially symmetric particles with R as the half-width or radius small compared to wavelength ($\pi 2/k$), we have $v = \{2R, \pi R^2, \pi 4R^3/3\}$. More generally, we use R as a size measure⁴ for arbitrary convex particles. In two dimensions, $v = \ell(R^2)$ represents an area with perimeter $s = \ell(R)$ and average radius of curvature $\bar{r} = s/2\pi$, such that $s\bar{r}/v = c > c_0 = 2$. In three dimensions, $v = \ell(R^3)$ is a volume with surface area $s = \ell(R^2)$, and $\bar{r} = \ell(R)$ as the average over all angles of the mean of the particle's principal radii of curvature, for such cases, $s\bar{r}/v = c > c_0 = 3$. For $c = c_0$, a particle is radially symmetric.

The incoherent single scattering from unit volume of a central region (V_c) containing an average number $\langle n \rangle$ of identical randomly distributed correlated particles is proportional to σ and to the variance (fluctuation) in particle number. The corresponding differential scattering cross section² equals

$$\Delta = \frac{\sigma(\langle n^2 \rangle - \langle n \rangle^2)}{V_c} \approx \frac{\sigma \langle n \rangle W}{V_c} = \sigma p W, \quad (2)$$

where $\rho = \langle n \rangle/V_c$ is the number density, and

$$W = 1 + \rho \int h(r) dV \quad (3)$$

is the correlation (or packing) factor with $h(r)$ as the total correlation function. To first order in ρ it follows that

$$\Delta \approx \Delta_0 = \sigma p p v^2 = p w = P w, \quad w = \rho v, \quad P = p v, \quad (4)$$

where Δ_0 is uncorrelated, and increases linearly with the volume fraction w occupied by particles (convex or not). The population factor $P = p v$ is independent of w . In terms of P we rewrite (2) as

$$\Delta = P S, \quad S = w W, \quad (5)$$

where S is the fluctuation-correlation function (or fluctuation factor).

To emphasize essential features and indicate restrictions, we start with S for a distribution modeled as a statistical mechanics fluid of identical hard spheres. Using the scaled particle equation of state¹⁷ (identical to and derived earlier than the Percus-Yevick equation of state¹⁸), it was shown¹² that

$$S = \frac{w(1-w)^4}{(1+2w)^2}, \quad w_\infty = \frac{\sqrt{73}-7}{12} \approx 0.129, \\ S_\infty \approx 0.0469 \quad (6)$$

(which, by geometry, also applies for aligned similar ellipsoids). As w increases from zero, S increases relatively steeply to S_∞ at w_∞ , and then decreases more gradually to zero (no fluctuations) at the unrealizable bound $w = 1$ corresponding to full packing.

More generally, for an isotropic fluid of hard convex particles (represented by $c > c_0 = 3$) averaged over orientation, it was shown² from the corresponding scaled particle equation of state⁴ that

$$S = \frac{w(1-w)^4}{\{1 + (c-1)w\}^2}, \\ w_\infty = \frac{2}{4 + c + (4 + 20c + c^2)^{1/2}}. \quad (7)$$

For given w_∞ ,

$$c = 1 + \frac{1 - 5w_\infty}{w_\infty(1 + 3w_\infty)}, \quad (8)$$

$$S_\infty = w_\infty(1 - w_\infty)^2(1 + 3w_\infty)^2/4.$$

For c increasing above 3, the values of S_∞ and w_∞ at the peak decrease below the values in Eq. (6). However, we also considered $3 > c > 0$ formally, in which range S_∞ increases to $4/27$ and w_∞ to $1/3$. Such larger values could be interpreted physically as arising from additional neighbors at small separations of particles, by comparison of leading terms of S with the first two virial coefficients for more attractive weakly repulsive models than the hard model (unattractive at all separations and repulsive on contact).

For an N -component isotropic fluid of similarly shaped (same c) but differently sized (R_i for $i = 1$ to N) hard convex particles, the analog of Eq. (2) involves the covariance of the numbers of i -type and j -type particles. Thus¹

$$\Delta \approx \rho \sum_{ij} v_i v_j [\langle n_i n_j \rangle - \langle n_i \rangle \langle n_j \rangle] / V_c \\ = \rho \sum v_i v_j \sqrt{\rho_i \rho_j} W_{ij} \quad (9)$$

where $\rho_i = \langle n_i \rangle / V_c$ is the partial number density (i.e., $\sum \rho_i = \rho$), and

$$W_{ij} = \delta_{ij} + \sqrt{\rho_i \rho_j} \int h_{ij} dV \quad (10)$$

in terms of the Kronecker delta and the partial correlation functions. The key variable is the net volume fraction

$$w = \sum \rho_i v_i = \rho \sum \frac{\rho_i}{\rho} v_i \equiv \rho \langle v \rangle, \quad \rho = \sum \rho_i. \quad (11)$$

Henceforth, we use the angular brackets only to indicate an average over size.

To lowest order in ρ , the analog of Eq. (4) is given by

$$\Delta_0 = \rho \sum \rho_i v_i^2 = \rho p \langle v^2 \rangle = p \langle \langle v^2 \rangle / \langle v \rangle \rangle w = P w, \quad (12)$$

and the analog of Eq. (5) may be written as

$$\Delta \approx P S, \quad P = p v, \quad v \equiv \langle v^2 \rangle / \langle v \rangle > \langle v \rangle, \quad (13)$$

where P represents a population factor that is independent of w .

All averages over size, e.g., as in Eqs. (11) and (12), can be expressed in terms of the moments of the size distribution,

$$\langle R^n \rangle = \sum_p \frac{\rho_p}{\rho} R_p^n = \int_0^\infty F(R) R^n dR. \quad (14)$$

Here $F(R)$ is a set of weighted delta functions for a discrete N-component mixture, or a probability density function for a continuous (polydisperse) distribution.

From the scaled particle chemical potentials for mixtures of convex particles^{3,4} (potentials which for spheres are identical to those obtained from the earlier Percus-Yevick equation for mixtures¹⁴), it was shown¹ that

$$S = \frac{w(1-w)^2}{[1+(c-1)w]^2} \{ (1-w)^2 + (1-w)wc2A + w^2c^2B \}, \quad (15)$$

$$A = 1 - \frac{\langle R^4 \rangle \langle R^2 \rangle}{\langle R^3 \rangle \langle R^6 \rangle},$$

$$B = 1 - \frac{2\langle R^4 \rangle \langle R^4 \rangle}{\langle R^3 \rangle \langle R^6 \rangle} + \frac{\langle R^4 \rangle^2}{\langle R^3 \rangle^2 \langle R^6 \rangle}.$$

In Eq. (15), S equals the one-component form as in Eq. (7) plus two additional terms that depend on the size distribution and decrease more slowly as w increases: the first term in brackets decreases rapidly to zero with increasing w , the second term is parabolic around $w = 1/2$, and the third term increases as w^2 . The value $c = 3$ corresponds to mixtures of spheres (or aligned similar ellipsoids). For the one-component case, the ratios involving the moments equal unity, and $A = B = 0$.

The corresponding two dimensional result (based on the scaled particle potentials for convex disks¹⁵) is given by¹

$$S = \frac{w(1-w)^2}{1+(c-1)w} \{ (1-w) + wcA \}, \quad (16)$$

$$A = 1 - \frac{\langle R^3 \rangle^2}{\langle R^2 \rangle \langle R^4 \rangle}.$$

In Eq. (16), S equals the one-component form discussed earlier,² plus an additional term that depends on the size distribution and decreases more gradually with increasing w . The value $c = 2$ corresponds to mixtures of parallel circular cylinders (or similar elliptic cylinders with aligned principal diameters). For the one-component case, the ratio involving three moments reduces to unity, and $A = 0$; then²

$$w_\lambda = 1/[2 + (1 + 3c)^{1/2}], \quad c = 1 + (1 - 4w_\lambda)/3w_\lambda^2, \\ S_\lambda = 3w_\lambda^2 (1 - w_\lambda)^2.$$

For the one dimensional case (based on exact hard-rod statistical mechanics results, which either the scaled particle or Percus-Yevick theory reproduces),

$$S = w(1-w)^2; \quad w_\lambda = 1/3, \quad S_\lambda = 4/27. \quad (17)$$

This form of S for parallel slabs is independent of the size distribution, and is also the special result obtained from either Eq. (15) or Eq. (16) for $c = 0$. Except for Eq. (17), which is valid for $w = 1$, no upper realizable bound is known analytically for any of the cases considered. For identical spheres, measurements show that the upper bound approximates 0.63, and for circular cylinders, the analog 0.84 is also an approximation based on measurements, see citations in Ref. 9.

Results for the single scattered differential scattering cross section $\Delta(\theta) = \rho(\theta) v S$, provide analogs for the total scattering cross section, Δ , by integrating over all appropriate values of θ . Thus in $\{1,2,3\}$ dimensions,

$$\Delta = \rho v S = P, S,$$

$$P = \left[|C'| - 1 \right]^2 \quad (18)$$

$$+ \left\{ 1, \frac{1}{2}, \frac{1}{3} \right\} |B' - 1|^2 \left\{ \frac{k^2}{2}, \frac{k^4}{4}, \frac{k^4}{4\pi} \right\},$$

and the corresponding absorption coefficient equals²

$$\gamma = \rho \sum_p \frac{\rho_p}{\rho} \sigma_p = (\text{Im} C' + |\text{Im} B'|) w k. \quad (19)$$

The sum $\gamma + \Delta = 2 \text{Im} K$ is the attenuation coefficient per unit length for the coherent intensity, and $\text{Re} K = k + \text{Re}(C' - B') w k / 2$ specifies the associated phase.⁹ The multiple scattered version of $\Delta(\theta)$ is proportional to exponential translational factors in γ and Δ , and such factors as well as transducer factors are required to determine $\Delta(\theta)$ by measurements, e.g., by the Sigelmann-Reid substitution method.¹⁶ The region V_c , introduced for Eqs. (2) and (9), corresponds to a homogeneous region in which the same value of w is appropriate not only for $\Delta(\theta)$ but also for the translational factors that account for attenuation of the incident and radiated fields in passage through the distribution.

II. POLYDISPERSE DISTRIBUTIONS

The forms (13)-(17) can be applied to discrete N-component (binary, ternary, etc.) mixtures, or to polydisperse cases (parabolic, Gaussian, etc.). Essentially as before, we consider the gamma probability density function¹⁰

$$F(R) = \frac{\beta}{\Gamma(\alpha)} (\beta R)^{\alpha-1} \exp(-\beta R); \quad R > 0, \beta > 0, \alpha > 0, \quad (20)$$

where $\Gamma(\alpha) = (\alpha-1)\Gamma(\alpha-1)$ is the gamma function, if $\alpha-1$ is an integer, then F is also known as the Schulz density function,¹¹ but the restriction is not appropriate for data inversion purposes. Using Eq. (20) in Eq. (14) yields the corresponding moments

$$\langle R^n \rangle = \beta^{-n} \{ \alpha(1+\alpha)(2+\alpha) \dots [(n-1)+\alpha] \}. \quad (21)$$

Equivalently, in terms of the mean value (\bar{R}) and normalized variance (d),

$$\langle R \rangle = \alpha/\beta \equiv \bar{R}, \quad (\langle R^2 \rangle - \bar{R}^2)/\bar{R}^2 \equiv d \geq 0, \quad (22)$$

we obtain¹

$$\langle R^n \rangle = \bar{R}^n (1+d)(1+2d) \dots [1+(n-1)d] \quad (23)$$

which indicates explicitly how all moments increase with increasing \bar{R} and d .

For $d \ll 1$, the maximum value of F is attained for $R = R_\lambda = \bar{R}(1-d)$, so that the distribution is skewed positively. For small d , F is Gaussian around R_λ , if $d \rightarrow 0$, then $R_\lambda \rightarrow \bar{R}$ and $F \rightarrow \delta(R - \bar{R})$ to reproduce one-component results. For $d = 1$, F reduces to $[\exp(-R/\bar{R})]/\bar{R}$ for the simplest Poisson case. Representative plots of F are given in Fig. 1.

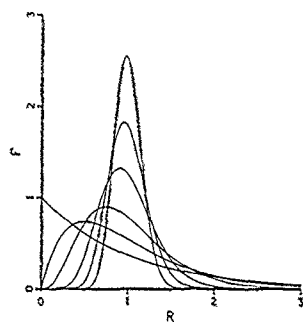


FIG. 1. Plots of the gamma probability density function $F(R)$ normalized so that $F(R) = 1$ with d as the parameter. The higher curves at $R = 1$ apply for the smaller values of $d = 0.025, 0.05, 0.1, 0.25, 0.5$ and 1 . As d approaches zero, F approaches $\delta(R - 1)$ corresponding to the monodisperse case.

In terms of \bar{R} and d , the averages of v in $\{1, 2, 3\}$ dimensions are given by

$$\begin{aligned} \langle v_1 \rangle &= v_1(\bar{R}) = 2\bar{R}, & \langle v_2 \rangle &= v_2(\bar{R})(1 + d), \\ \langle v_3 \rangle &= v_3(\bar{R})(1 + d)(1 + 2d), \end{aligned} \quad (24)$$

and we write the corresponding forms of $v = \langle v^2 \rangle / \langle v \rangle$ as

$$\begin{aligned} v_1 &= \langle v_1 \rangle (1 + d), & v_2 &= \langle v_2 \rangle \frac{(1 + 2d)(1 + 3d)}{(1 + d)}, \\ v_3 &= \langle v_3 \rangle \frac{(1 + 3d)(1 + 4d)(1 + 5d)}{(1 + d)(1 + 2d)}. \end{aligned} \quad (25)$$

Data for w and for ρ determine $\langle v \rangle = w/\rho$.

For distributions of particles with size governed by F of Eq. (20), we obtain two-parameter forms of Eqs. (15) and (16) in terms of c and d , and display their coupling interactions graphically in Figs. 2 to 8. To delineate curve shapes,

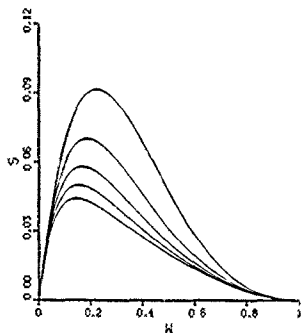


FIG. 2. Plots of the three-dimensional fluctuation-correlation function $S(c, d, w)$ of Eq. (26) versus volume fraction w for $d = 0.2$ with c ranging from 1.0 (the highest curve) to 5.0 (the lowest) in steps of 1.0 .

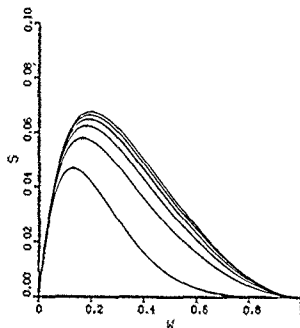


FIG. 3. The three-dimensional $S(c, d, w)$ of Eq. (26) for $c = 3.0$ with d ranging from $d = 0.0$ for the lowest curve to $d = 1.0$ for the highest in steps of 0.2 . For hard particles the value $c = 3$ corresponds to spheres.

we plot for the complete range of w from 0 to 1 .

For the three dimensional case Eq. (15) in terms of Eq. (23), we have¹

$$\begin{aligned} S(c, d; w) &= \frac{w(1-w)^2}{[1 + (c-1)w]^2} \left\{ (1-w)^2 \right. \\ &\quad \left. + (1-w)w \frac{4cd}{1+5d} + \frac{w^2 c^2 d}{1+4d} \right\}. \end{aligned} \quad (26)$$

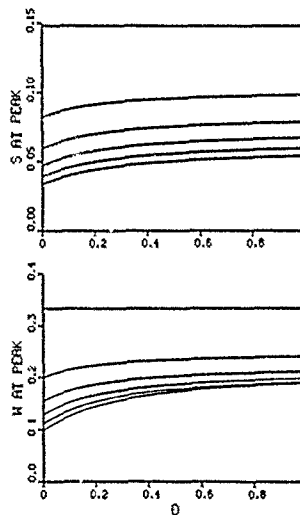


FIG. 4. Peak S and its location w^* for S of Eq. (26) versus d . The parameter c ranges from 0.0 (the highest curve in each panel) to 5.0 (the lowest) in steps of 1.0 . For $c = 0$, the slab results $S = 4/27$ and $w^* = 1/3$ are independent of d .

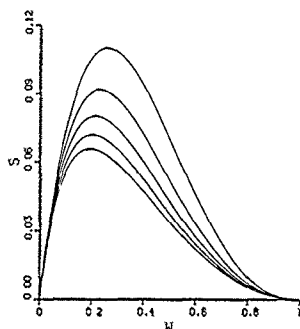


FIG. 5 The two-dimensional fluctuation-correlation function $S(c, d, w)$ of Eq. (27) for $d = 0.2$ with c ranging from 1.0 (for the highest curve) to 5.0 (the lowest) in steps of 1.0. The value $c = 2$ corresponds to hard circular cylinders.

It is clear by inspection of Eqs. (26) and (7) that the additional terms in d reduce the falloff of S with increasing w , and perturbation expansions for small d indicate that for given c the peak and its location have values larger than S_A and w_A of Eq. (7). Figure 2 plots $S(c, 0.2; w)$ with c as a parameter; as c increases from 1 to 5, the peak S_A decreases from 0.19 to 0.044, and w_A decreases from 0.22 to 0.14. Figure 3 plots $S(3, d; w)$ with d as the parameter; as d increases from 0 to 1, the peak S_A increases from 0.047 to 0.067, and w_A increases from 0.13 to 0.2. The value $c = 3$ was chosen to stress that a polydisperse distribution of spheres gives rise to a higher peak at a larger volume fraction than predicted by the monodisperse results Eq. (6). Figure 4 plots S_A and w_A vs d with c as the parameter, the horizontal lines for $c = 0$ are the same as for the one dimensional case Eq. (17). Form (26) and the related curves are appropriate for suspensions of cells, at least for cases where the cells correspond to randomly oriented hard convex particles.

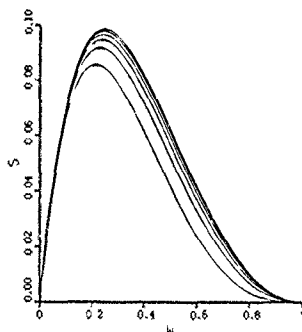


FIG. 6 The two-dimensional S of Eq. (27) for $c = 2.0$ with d ranging from 0.0 for the lowest curve to $d = 1.0$ for the highest in steps of 0.2

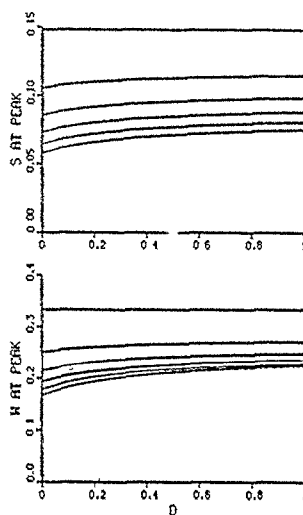


FIG. 7 Peak S and its location w_A for S of Eq. (27) vs d . The parameter c ranges from 0.0 (the highest curve) to 5.0 (the lowest) in steps of 1.0. The results for $c = 0$ are as discussed for Fig. 4

Analogous results for the two dimensional case (16) in terms of Eq. (23),

$$S(c, d; w) = \frac{w(1-w)^2}{1 + (c-1)w} \left\{ (1-w) + \frac{wcd}{1+3d} \right\} \quad (27)$$

are displayed in Figs. 5 to 7. Form (27) and the related curves are appropriate for parallel fibers, at least for hard convex cases.

Figure 8 shows curves for $\Delta(w) = PS$ based on Eq. (26)

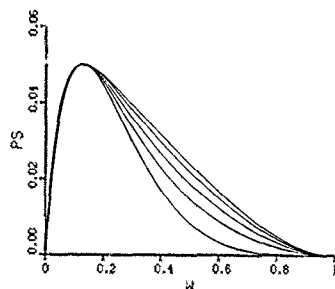


FIG. 8. Plots of PS based on the three-dimensional $S(c, d, w)$ of Eq. (26) for several sets of $\{P, c, d\}$ which yield the same Δ at w . From the highest curve to the lowest, the values used are $\{P, c, d\} = \{1.427, 0.0, 18\}$, $\{1.32, 6.0, 15\}$, $\{1.23, 5.0, 11\}$, $\{1.15, 4.0, 0.06\}$, and $\{1.07, 3.0, 0.0\}$. The last set corresponds to identical spheres.

that indicate the same values of Δ_λ and w_λ can arise for different curves generated by different sets of values $\{P, c, d\}$. The curves are practically indistinguishable for $0 < w < w_\lambda + 0.05$, and only the shape of the lowest curve at relatively large values of w enables us to identify the original curve for monodisperse spheres (as in Fig. 21, Ref. 9, 1967). No simple inversion procedure emphasizing data near the peak suffices, and scattering data at large w is essential if the parameters P and d that specify cell population (cell volume and size distribution for given C' and B') cannot be obtained by more direct methods.

III. COMPARISON WITH DATA

Shung and his associates^{6,17-20} obtained extensive reduced¹⁶ data records for ultrasonic backscattering (Δ) vs hematocrit (equated to w) for bovine and human RBC suspensions under different flow conditions. Each data record for $0 \leq w \leq 0.5$ shows a marked peak (Δ_λ) at a value $w = w_\lambda > 0.13$, i.e., at a larger w_λ than exhibited by S of (6) for identical hard spheres.⁶ We applied⁶ Eq. (8) heuristically to all available data records^{6,17-20} and obtained initial estimates $c(w_\lambda)$ and $P = \Delta_\lambda / S_\lambda$, that were sharpened by considering all data points with explicit bias (EB) on those near the peak, and then refined to determine a common value of P for each cell population subjected to three or two different flow processes. The present article restricts consideration to Ref. 6 which provides the most comprehensive data under conditions which minimize formation of clusters.

The dashed curves in Figs. 9 to 12 show EB fits⁷ to all the data records of Ref. 6 for RBCs in isotonic saline for four different processes, uniform (u) or turbulent (t) flowing suspensions in a conduit system, and stationary (s) or stirred (s') confined suspensions. Figures 9 to 11 correspond to two different bovine cell populations with nominal value⁶ $P_b = 2.57 \times 10^{-4}$ (in cm^3/sr^2). Fig. 9 for the smaller cells shows the three data records (s, u) of Fig. 6.5 and the

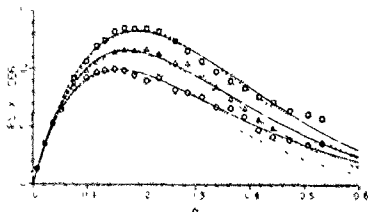


FIG. 9 Backscattering data of Fig. 6.5 (i.e., of Ref. 6, Fig. 5) for bovine red blood cells in saline under turbulent flow (squares), stationary (triangles), and uniform flow (circles) conditions compared with PS curves versus volume fraction w . (The flow rate 60 ml/s applies to both flow processes, and the frequency 7.5 MHz, and temperature 23°C also apply for subsequent figures.) The EB curves of Fig. 7.1 (shown dashed) are based on $P = 1.7 \times 10^{-4}$, $d = 0$, and $c = (1.1, 1.5, 2.1)$ for the highest, central, and lowest, respectively. The dotted monodisperse LS curves are based on $P = 1.64 \times 10^{-4}$, $d = 0$, and $c = (1.01, 1.35, 1.77)$. The solid polydisperse LS curves are based on $P = 1.79 \times 10^{-4}$, $d = 0.088$, and $c = (1.50, 2.05, 2.74)$. The trends of the c sets are consistent for all sets of curves. The dotted LS curves use a 4-parameter least-squares fit to all data points to Eq. (7), and the solid use a 5-parameter fit to (26)]

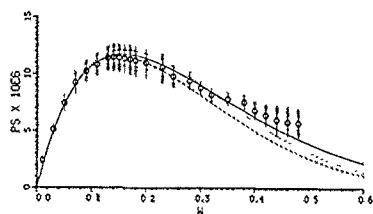


FIG. 10 Comparison of PS curves with uniform flow scattering data of Fig. 6.4 for larger bovine cells than in Fig. 9. The circled points are averages of five measurements, and the vertical segments are the standard deviations. The EB curve of Fig. 7.3 (shown dashed) is based on $P = 2 \times 10^{-4}$, $d = 0$, and $c = 2.1$, the dotted LS curve is based on $P = 1.91 \times 10^{-4}$, $d = 0$, and $c = 1.765$, the solid polydisperse LS curve is based on $P = 2 \times 10^{-4}$, $d = 0.07$, and $c = 2.43$.

EB curves (dashed) of Fig. 7.1, Figs. 10 and 11 for the larger cells show the u data of Fig. 6.4 and the EB curve (dashed) of Fig. 7.3, and s and s' data of Fig. 6.8 and EB curves (dashed) of Fig. 7.4. Figure 12, corresponding to human RBC with nominal⁶ $P_h = 5.17 \times 10^{-4}$, shows s and s' data of Fig. 6.9 and EB curves (dashed) of Fig. 7.10. Except for the stirred suspensions (for which the anomalous range of low data points suggested a vortex inhomogeneity⁷ and were discounted in the fitting), the EB monodisperse ($d = 0$) curves are in accord with the major data trends to at least $w \approx w_\lambda + 0.1$.

The consistency of the uniform flow process, and the discrepancy of the EB curves (too low) at large w , were highlighted by Fig. 7.5 which compares u records of Figs. 6.4 and 6.5 with corresponding EB curves. The systematic increase of the discrepancy with increasing w could arise from an additional fluctuation mechanism leading to more scattering than indicated by the monodisperse S of Eq. (7). The effects of polydispersity shown by $S(c, d; w)$ of Eq. (26) would reduce the falloff with increasing w , and motivated the present heuristic applications. Preliminary computa-

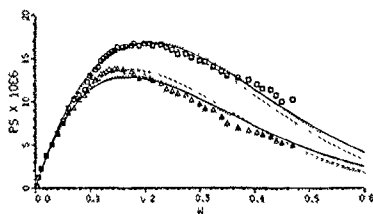


FIG. 11 Data of Fig. 6.8 for stationary (higher points) and stirred bovine cells in saline corresponding to Fig. 10 compared with PS curves. For the EB curves of Fig. 7.4 (shown dashed), $P = 2 \times 10^{-4}$, $d = 0$, and $c = (0.95, 1.5)$ for the higher and lower respectively, for the dotted LS curves, $P = 1.91 \times 10^{-4}$, $d = 0$, and $c = (0.818, 1.520)$, for the solid polydisperse curves $P = 2 \times 10^{-4}$, $d = 0.07$, and $c = (1.085, 2.023)$. The trends of the c sets of Figs. 10 and 11 are consistent for all three sets of curves. (The LS curves for the three data records in Fig. 10 plus Fig. 11, were obtained as for Fig. 9)

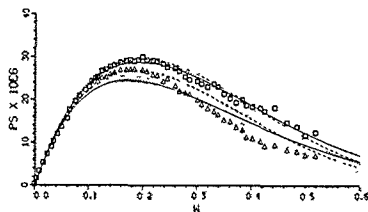


FIG. 12 Data of Fig. 6.9 for stationary (higher points) and stirred human red blood cells in saline. The EB curves of Fig. 7.10 (shown dashed) are based on $P = 3.6 \times 10^{-4} = 0.70P_s$, $d = 0$, and $c = (1, 1, 25)$ for the higher and lower curve, respectively. The dotted LS curves are based on $P = 3.74 \times 10^{-4}$, $d = 0$, and $c = (1.101, 1.523)$ obtained from a 3-parameter LS fit to all data points. The solid curve for the stationary process is based on a 3-parameter LS fit for $P = 3.75 \times 10^{-4}$, $d = 0.107$, and $c = 1.455$; these same values of P and d were used for the solid curve for the stirred process in a 1-parameter LS fit for $c = 2.077$.

tions for $d > 0$, and the curves in Fig. 8, demonstrated that any inversion procedure emphasizing data near the peak would yield ambiguous results for $\{P, c, d\}$, data points at large w were essential. We obtained representative values for the effective parameters by fitting to all data points of the records using multiparameter nonlinear least-squares (m -LS) procedures.⁶ The solid LS curves in Figs. 9-12 resulted by fitting to Eq. (26); the dotted LS curves obtained by fitting to Eq. (7) are included to distinguish the effects of polydispersity from artifacts of the fitting procedures.

Although there are only three parameters $\{P, c, d\}$ in the polydisperse PS based on Eq. (26), and each data record of Ref. 6 can be better fitted by a 3-LS routine, the set of three solid curves in Fig. 9 for one cell population, and the set of three in Figs. 10 and 11 for the other, were obtained by a generalized $(2+3)$ -LS routine. Thus all data points in Fig. 6.5 for the smaller cells were fitted to isolate common values of P and d , and three distinct values of c representative of the three different (u, s, t) process. The $(2+3)$ -LS routine minimized the total sum of the squares of the errors between data points of all three records and three corresponding curves based on PS of Eq. (26); see the Appendix. The same $(2+3)$ -LS procedure was followed for the larger cells of Figs. 6.4 and 6.8 to isolate common values of P and d , and three values of c representing the different (u, s, t) processes. Similarly, for the dotted LS curves based on the two parameter monodisperse form for $d = 0$, we used a $(1+3)$ -LS routine to isolate a common P and different values of c . These values provide checks on the consistency of trends in c , as well as more appropriate curves than the EB curves for assessing the role of the polydispersity parameter d .

Better fitting curves were obtained for each of the six bovine data records by an independent 3-LS routine, but some of the values of d were unrealistically high (e.g., as large as 0.35) for distributions of individual RBCs, and the trends in P and c were erratic as compared with trends shown by corresponding 2-LS values obtained for $d = 0$. Since the $(2+3)$ -LS values of P and d are based on all data points of three data records, they correspond to a population

sample essentially three-fold larger than for a single record, and we may expect them to be more representative. For the $(2+3)$ -LS effective parameters, the values of d are less than 0.09, and the trends of c for the different processes are consistent with the trends of the $(1+3)$ -LS and EB monodisperse values.

Figure 9 shows that the differences between the solid and dotted curves for turbulent and stationary processes are minor, but the solid curves are somewhat better for $w < w_A$ and for large w . For the uniform process, the solid curve is by far the better. Comparison of the two LS curves for uniform flow delineates the marked improvement of the overall fit arising from the inclusion of polydispersity in the theory, and the effects of an additional parameter in an LS fit of data to a more suitable curve. The same applies in Fig. 10 for the larger bovine cells in uniform flow. In Fig. 11 the differences of the solid and dotted curves for the stationary process are minor, for the stirred process, none of the curves is suitable for fitting the anomalous sigmoidal set of data points.

Figure 12, the human cell analog of Fig. 11, also indicates that the stirred process is anomalous. The $(2+2)$ -LS routine for common values of P and d , and two distinct values of c , gave an unrealizable negative value of d , as did an independent 3-LS routine for the stirred data points. Consequently, although the dotted curves for $d = 0$ correspond to a $(1+2)$ -LS fit for both data records in Fig. 6.9, the solid curves do not correspond to a simultaneous fit for both data records. The solid polydisperse curve for the s data, based on an independent 3-LS routine, is better than the others at large w . The solid curve for the s' data, based on the s values of P and d in a 1-LS fit for c , serves primarily to display the anomaly more symmetrically.

Thus polydisperse scattering theory¹ provides markedly better accord for all w than monodisperse theory⁷ for the uniform flow process, and somewhat better accord for the turbulent and stationary processes. However, we maintain our earlier detailed reservations⁷ on the heuristic applications of theory developed for homogeneous distributions of similar hard convex particles to the different processes⁶ involving flexible deformable biconcave discs. In addition, although the present unweighted LS inversion routines are more systematic than the earlier EB procedure,⁷ more suitable weighted LS routines could be evolved by experimentalists working with statisticians. The effective values of the parameters we isolated by the present procedure are sufficiently representative to help delineate major data trends of the more controlled processes for the full ranges⁶ of w that were considered.

ACKNOWLEDGMENTS

Work supported in part by the Office of Naval Research.

APPENDIX: NONLINEAR LEAST-SQUARES ROUTINES

All least-squares curve fitting⁸ was done with IMSL 1000 subroutine BCLSF which solves a nonlinear least

squares problem subject to bounds on the variables using a modified Levenberg-Marquardt algorithm and a finite-difference Jacobian.

In order to fit a data record (a set of data points for a particular cell population involved in a specific flow process) of Ref. 6 by a curve based on Eq. (26), this iterative routine required upper and lower bounds on the values of the parameters $\{P, c, d\}$ as well as initial guesses. It was sufficient to take P and c as nonnegative and d in the range -0.1 to 0.7 . Practically any such values of P and c could be used as initial guesses for $d = 0$, and the resulting values of P and c were then used as initial guesses to determine $\{P, c, d\}$ for $d \neq 0$.

For n sets of data ($n \approx 3$) on the same population of cells we fitted to n curves based on Eq. (26) for $2 + n$ parameters, i.e., we assumed that all n curves had common values of P and d , but that each curve had a different c . The routine minimized the total sum of the squares of the errors between the data points of all n sets and their n corresponding curves.

The routines for either $d = 0$ or $d \neq 0$ were extremely stable and insensitive to initial guesses, and converged rapidly (in 10 iterations or less) to unique output values of P , c , and d .

A 4-parameter fit to all stationary and stirred data points for human cells, and a 3-parameter fit to just the stirred data points, gave unrealizable negative values of d as outputs. We settled for a 3-parameter fit to the stationary points, and used the resulting values of P and d in a 1-param-

eter fit to the stirred data to determine the corresponding c . See caption for Fig. 12.

- ¹V Twersky, *J. Acoust. Soc. Am.* **84**, 409 (1988).
- ²V Twersky, *J. Acoust. Soc. Am.* **81**, 1609 (1987).
- ³J. L. Lebowitz, E. Helfand, and E. Praestgaard, *J. Chem. Phys.* **43**, 774 (1965).
- ⁴R. M. Gibbons, *Mol. Phys.* **17**, 81 (1969); *Mol. Phys.* **18**, 809 (1970).
- ⁵Lord Rayleigh, *Theory of Sound* (Cambridge U.P., London, 1878, reprinted by Dover, New York, 1954), Sec. 296 of Dover reprint.
- ⁶K. K. Shung, Y. W. Yuan, D. Y. Fei, and J. M. Tarbell, *J. Acoust. Soc. Am.* **75**, 1265 (1984).
- ⁷R. J. Lucas and V. Twersky, *J. Acoust. Soc. Am.* **82**, 794 (1987).
- ⁸IMSL 10.0 subroutine BCLSF, an iterative nonlinear least-squares numerical procedure based on the Levenberg-Marquardt algorithm.
- ⁹V. Twersky, *J. Acoust. Soc. Am.* **64**, 1710 (1978); *J. Opt. Soc. Am.* **65**, 524 (1975); S. W. Hawley, T. H. Kays, and V. Twersky, *IEEE Trans. Ant. and Prop.* **AP-15**, 118 (1967), see Eqs. (16)-(19).
- ¹⁰I. Olkin, L. J. Gleser, and C. Derman, *Probability Models and Applications* (Macmillan, N.Y., 1980) p. 267ff.
- ¹¹S. R. Aragon and R. Pecora, *J. Chem. Phys.* **64**, 2395 (1976).
- ¹²H. Reiss, H. L. Frisch, and J. L. Lebowitz, *J. Chem. Phys.* **31**, 369 (1959); E. Helfand, H. L. Frisch, and J. L. Lebowitz, *J. Chem. Phys.* **34**, 1037 (1961).
- ¹³M. S. Wertheim, *Phys. Rev. Lett.* **10**, 321 (1963); E. Thiele, *J. Chem. Phys.* **39**, 474 (1963).
- ¹⁴J. L. Lebowitz, *Phys. Rev.* **133**, A895 (1964).
- ¹⁵T. Boublik, *Mol. Phys.* **29**, 421 (1975).
- ¹⁶R. A. Sigelmann and J. M. Reid, *J. Acoust. Soc. Am.* **53**, 1351 (1973).
- ¹⁷K. K. Shung, R. A. Sigelmann, and J. M. Reid, *IEEE Trans. Biomed. Eng.* **BME-23**, 460 (1976).
- ¹⁸K. K. Shung, *J. Cardiovas. Ultrason.* **2**, 401 (1983).
- ¹⁹Y. W. Yuan and K. K. Shung, *IEEE Ultrason. Symp. Proc.* **Pub. 84**, CH2112-1 (IEEE, NY, 1984) pp. 666-669.
- ²⁰Y. W. Yuan and K. K. Shung, *J. Acoust. Soc. Am.* **84**, 52 (1988).

High-frequency reflection and scattering by multicomponent rough surface distributions

R. J. Lucas^{a)} and V. Twersky

Mathematics Department, University of Illinois, Chicago, Illinois 60680

(Received 23 July 1989; accepted for publication 4 January 1990)

Earlier forms for the coherent reflection and incoherent scattering by multicomponent mixtures of bosses on rigid or free base planes [V. Twersky, J. Acoust. Soc. Am. 29, 209-225 (1957)] are applied to recent high-frequency results for aligned hemiellipsoidal bosses [R. J. Lucas and V. Twersky, J. Acoust. Soc. Am. 83, 2005-2011 (1988)] to investigate continuous distributions in boss size. Approximations for the coherent reflected intensity and incoherent differential scattering cross sections are obtained in terms of integrals of simple functions and a general probability density. To provide illustrations, numerical computations and graphical results are based on truncating the two-parameter gamma probability density function $P(t; m, v)$ with t as a dimensionless variable that scales one or more boss dimensions, m as the mean value of t , and v as the normalized variance (ranging from zero to unity). For v small, P is Gaussian and reduces to a delta function as v approaches zero (to reproduce one-component results). More generally, the curve of P is skewed, and as v approaches unity P reduces to the exponential for the simplest Poisson case. Graphs are shown for cases where one (e.g., keel depth), two (e.g., base axes), or all three dimensions of the protuberances are randomized. The essentials are indicated by plots versus angle of incidence, with v as the parameter. The coherent intensity and the associated forward and backscattered incoherent differential scattering cross sections per unit area are emphasized.

PACS numbers: 43.20.Fn

INTRODUCTION

In a previous article,¹ results^{2,3} for the coherent reflection and incoherent scattering by random distributions of relatively arbitrary bosses on rigid or free (pressure release) base planes were specialized to identical aligned hemiellipsoidal bosses with semidiameters large compared to wavelength. The present paper applies the earlier² energy conserving forms for reflection and scattering by mixtures of different type bosses to investigate continuous multicomponent distributions in boss size. As before,^{1,4} we emphasize the coherent reflected intensity (R) and the forward-scattered (specular) and backscattered incoherent differential cross sections per unit areas [$\sigma(f)$ and $\sigma(b)$]. Approximations for R and σ are obtained in terms of integrals of simple functions and a general distribution function that specifies the statistical aspects.

Graphical illustrations of R , $\sigma(f)$, and $\sigma(b)$ are based on a truncated version of the Schulz⁵ form for the two-parameter gamma probability density function⁶ $P(t; m, v)$. Here, t is a dimensionless parameter that scales one or more boss axial dimensions (e.g., bosses with base semidiameters a , b and height tc), m is the mean value of t , and v is the normalized variance ranging from zero to unity. For v small, P is approximately Gaussian, and reduces to a delta function as v approaches zero to reproduce one-component results. More generally, v determines the skewness of P . As v approaches unity, P reduces to the exponential for the simplest

Poisson density. The resulting plots of R , $\sigma(f)$, and $\sigma(b)$ versus angle (α) of incidence, with v as the parameter, exhibit the essential aspects of the statistical distribution in boss size.

In the following, for brevity, we use (1.3) for Eq. (3) of Ref. 1, etc.

I. NOTATION AND KEY FORMS

We take the incident wave for a rigid (+) or free (-) base plane as $\pm \phi' e^{-ik'z}$, where

$$\begin{aligned}\phi' &= \exp(ik' \cdot r) = \exp(ikr \hat{k} \cdot \hat{r}), \\ \hat{r}(\theta, \varphi) &= (\hat{x} \cos \varphi + \hat{y} \sin \varphi) \sin \theta + \hat{z} \cos \theta, \\ \hat{k}' &= \hat{r}(\pi - \alpha, \beta),\end{aligned}\quad (1)$$

with \hat{k}' as the direction of incidence and $\lambda = 2\pi/k$ as the wavelength. The corresponding wave reflected from a smooth plane at $z = 0$ is the image

$$\phi = \exp(ik \cdot r), \quad k = k\hat{k}, \quad \hat{k} = \hat{r}(\alpha, \beta), \quad (2)$$

with \hat{k} as the direction of specular reflection. For ϕ incident on an isolated rigid or free ellipsoid at the phase origin, we use $g_{\pm}(\hat{r}, \hat{k})$ for the scattering amplitude. The scattering amplitude for the corresponding boss on a rigid or free base plane excited by $\pm \phi'$ follows by superposition:²

$$f_{\pm}(\hat{r}, \hat{k}') = g_{\pm}(\hat{r}, \hat{k}) \pm g_{\pm}(\hat{r}, \hat{k}'). \quad (3)$$

A multicomponent mixture of $i = 1$ to N distinct types of bosses is specified if each type is characterized by a parameter t_i , partial number density n_i , and net number density $n = \sum n_i$. The average of a boss attribute (say F_i) is given by

^{a)}Visiting from the Department of Mathematical Sciences, Loyola University, Chicago, IL 60626.

$$\langle F \rangle \equiv \sum_{i=1}^N \frac{n_i}{n} F_i, \quad n = \sum_{i=1}^N n_i, \quad (4)$$

where F_i is weighted by n_i/n in the average $\langle F \rangle$ for the mixture. The fraction of the plane covered by bosses of base area A_i is $w_i = n_i A_i$, and the net packing fraction equals

$$w = \sum w_i = n \sum \frac{n_i}{n} A_i = n \langle A \rangle, \quad (5)$$

with $\langle A \rangle$ as the average.

For a corresponding continuous distribution in boss types, the average is given by

$$\langle F \rangle = \int_0^\infty P(t) F(t) dt, \quad (6)$$

with $P(t)$ as a probability density function. The results (4) and (5) for N distinct types correspond to

$$P(t) = \sum_{i=1}^N \frac{n_i}{n} \delta(t - t_i), \quad (7)$$

a weighted sum of delta functions.

The coherent reflected field for the base plane plus bosses is given by²

$$\phi(1 + Z)/(1 - Z), \quad Z = \pi n \langle f(\hat{k}, \hat{k}') \rangle / k^2 \cos \alpha. \quad (8)$$

As before, we suppress subscripts \pm where feasible. The coherent power reflection coefficient equals

$$R = [1 + Z]/[1 - Z]^2, \quad (9)$$

and the net incoherent differential scattering cross section per unit area is given by

$$\sigma(\hat{k}, \hat{k}') = n \langle |f(\hat{k}, \hat{k}')|^2 \rangle / k^2 [1 - Z]^2. \quad (10)$$

We use the same symbols Z , R , and σ as before,¹ but here they involve $\langle f \rangle$ and $\langle |f|^2 \rangle$, as indicated after (1.12) these forms neglect pair correlations.

The forms given above account for all orders of coherent multiple scattering and are mutually consistent in exhibiting energy conservation for lossless bosses. See Ref. 2 for a complete discussion.

II. LARGE ELLIPSOIDAL BOSSES

For ellipsoids with principal semidiameters a, b, c (along x, y, z) large compared to wavelength,¹ we have $g_{\pm} = g_2 \pm g_1$, where $\pm g_1$ represents geometrical reflection, and g_2 diffraction (shadow formation). From (3) and (1.13)-(1.18) evaluated in the specular ($\hat{r} = \hat{k}$) direction, the forward-scattered amplitude for an isolated boss is given by

$$f_{\pm}(\hat{k}, \hat{k}') = g_2(\hat{k}, \hat{k}') \pm g_1((\hat{k}, \hat{k}') + g_1(\hat{k}, \hat{k}')) \\ = \frac{-k^2 ab}{2} \left(c\Gamma \pm \frac{c\Delta^2 \sin^2 \alpha J_1(2ku \cos \alpha)}{\Gamma k u \cos \alpha} \right. \\ \left. - \frac{i}{kc} e^{-2ikc \cos \alpha} \right),$$

$$\Gamma^2 = (\Delta \sin \alpha)^2 + (\cos \alpha)^2 / c^2, \\ \Delta^2 = (\sin \beta)^2 / b^2 + (\cos \beta)^2 / a^2, \quad (11)$$

$$u^2 = (L_1 \hat{z})^2 + (L_2 \hat{s})^2;$$

the L_i (the directed semidiameters of the elliptic disk de-

fined by the shadow boundary) are obtained from (1.19)-(1.21), and J_1 denotes the Bessel function. For near-grazing incidence, $\alpha = \pi/2 - \tau$, $\tau \approx 0$, we replace $g_1(\hat{k}, \hat{k}')$ by the alternate form given in (1.16) for $\hat{k}' \approx \hat{k}$.

In the backscattered direction ($\hat{r} = -\hat{k}'$), we have

$$f_{\pm}(-\hat{k}', \hat{k}') \\ = g_2(-\hat{k}', \hat{k}') \pm g_1(-\hat{k}', \hat{k}') + g_1(-\hat{k}', \hat{k}') \\ = \frac{-k^2 ab}{2} \left(\frac{2J_1(U) \cos^2 \alpha}{c\Gamma U} + \frac{ic}{k\delta^2} e^{-2ik\delta \sin \alpha} \right. \\ \left. - \frac{ic}{kD^2} e^{-2ikD} \right); \\ D^2 = (\delta \sin \alpha)^2 + (c \cos \alpha)^2, \\ \delta^2 = (a \cos \beta)^2 + (b \sin \beta)^2, \\ U^2 = (L_1 s)^2 + (L_2 s)^2, \\ s = 2 \sin \alpha (\hat{x} \cos \beta + \hat{y} \sin \beta).$$

For near-normal incidence ($-\hat{k}' \approx \hat{k}$), we replace $g_1(-\hat{k}', \hat{k}')$ by the alternate form (1.15).

For a continuous distribution in size, the coherent reflected intensity R and the forward and backscattered cross sections per unit area, $\sigma(f)$ and $\sigma(b)$, follow from (8)-(10) in terms of (11) and (12). In particular, the present Z based on the average of (11) may be written as

$$Z_{\pm} = \frac{-w}{2(ab) \cos \alpha} \\ \times \left(\langle abc\Gamma \rangle \pm \frac{\sin^2 \alpha}{k \cos \alpha} \left(\frac{abc\Delta^2 J_1(2ku \cos \alpha)}{\Gamma u} \right) \right. \\ \left. - \frac{i}{k} \left(\frac{ab}{c} e^{-2ikc \cos \alpha} \right) \right). \quad (13)$$

To facilitate comparisons, we may fix w and average over one or more boss semidiameters.

Up to moderately large values of α , we keep only the first term of Z to obtain

$$R \approx \left(\frac{1 - w \langle abc\Gamma \rangle / 2(ab) \cos \alpha}{1 + w \langle abc\Gamma \rangle / 2(ab) \cos \alpha} \right)^2; \quad (14)$$

if the numerator is small, then we retain additional terms. For $\alpha \approx 0$, near-normal incidence, (14) approximates

$$R \approx \left(\frac{1 - w \langle ab(1 + \epsilon) \rangle / 2(ab)}{1 + w \langle ab(1 + \epsilon) \rangle / 2(ab)} \right)^2, \\ \epsilon = (c\Delta \tan \alpha)^2 / 2. \quad (15)$$

This simple form reduces to the one-component result for $\alpha = 0$, but the complete expression based on (13) does not.

If R based on (14) is very small, we restore the exponential term of Z of (13); as α increases towards grazing, we retain all terms. For $\alpha \approx \pi/2$ (near grazing), we replace the third term of Z of (13) by that obtained from $g_1(\hat{k}, \hat{k}')$ of (1.16). For small-grazing angle $\tau = \pi/2 - \alpha$, it follows that

$$R_{+} \sim 1 + 4(ab)\tau/w \langle abc\Delta \rangle, \\ R_{-} \sim 1 - k^2 w \langle abc\Delta \rangle \tau / \langle ab \rangle. \quad (16)$$

As before,^{1,2} the difference from unity is $O(\tau)$ for either case.

The corresponding differential scattering cross sections for arbitrary \hat{r} are based on (1.30). In particular, in the for-

ward direction for α not near grazing, we base σ on $|f_{\pm}|^2$ of (11). The dominant term is

$$\sigma_{\pm}(f) \approx \frac{w\langle |g_2(\hat{k}, \hat{k}')|^2 \rangle}{\pi k^2 \langle ab \rangle |1 - Z_{\pm}|^2} \approx \frac{wk^2 \langle (abc\Gamma)^2 \rangle}{4\pi \langle ab \rangle (1 + w(abc\Gamma)/2 \langle ab \rangle \cos \alpha)^2} \quad (17)$$

In the backscattered direction for α not near 0 or $\pi/2$, we base σ on $|f_{\pm}|^2$ of (12). The dominant terms are

$$\sigma_{\pm}(b) \approx \frac{w\langle |g_1(-\hat{k}', \hat{k})|^2 + |g_1(-\hat{k}, \hat{k}')|^2 \rangle}{\pi k^2 \langle ab \rangle |1 - Z_{\pm}|^2} \approx \frac{w\langle (abc)^2 (\delta^{-4} + D^{-4}) \rangle}{4\pi \langle ab \rangle (1 + w(abc\Gamma)/2 \langle ab \rangle \cos \alpha)^2}, \quad (19)$$

where the rapidly oscillating terms were dropped to provide a simple common baseline for both cases.

At normal incidence both $\sigma(f)$ and $\sigma(b)$ correspond to backscattering

$$\begin{aligned} \sigma_{\pm}(f) &= \sigma_{\pm}(b) \\ &\approx \frac{wk^2 \langle (ab)^2 |1 - (i/kc)e^{-2ikc}|^2 \rangle}{4\pi \langle ab \rangle |1 + w/2 - iw\langle (ab/c)e^{-2ikc} \rangle / 2k \langle ab \rangle|^2} \\ &\approx \frac{wk^2 \langle (ab)^2 \rangle}{4\pi \langle ab \rangle (1 + w/2)^2}. \end{aligned} \quad (20)$$

For α near grazing, the forward-scattering cross sections approximate

$$\sigma_{+}(f) \approx \frac{k^2 \tau^2 \langle (abc\Delta)^2 \rangle \langle ab \rangle}{\pi w (abc\Delta)^2}, \quad (21)$$

$$\sigma_{-}(f) \approx \frac{wk^6 \tau^4 \langle c^6 (ab\Delta)^2 \rangle}{16\pi \langle ab \rangle}. \quad (22)$$

The near-grazing approximations for the backscattering are given by

$$\begin{aligned} \sigma_{+}(b) &\approx \frac{\tau^2 \langle (abc)^2 / \delta^4 \rangle \langle ab \rangle}{\pi w (abc\Delta)^2}, \\ \sigma_{-}(b) &\approx \frac{wk^2 \tau^4}{\pi \langle ab \rangle} \left\langle a^2 b^2 \left[\frac{c^3}{2\delta^3} e^{-2ik\delta} - \frac{J_1(U)}{\Delta c U} \right]^2 \right\rangle \\ &\approx \frac{wk^2 \tau^4}{\pi \langle ab \rangle} \left\langle a^2 b^2 \left[\frac{c^6}{4\delta^6} + \left(\frac{J_1(U)}{\Delta c U} \right)^2 \right] \right\rangle, \\ U &= k |(a^2 - b^2) \sin 2\beta| / (ab\Delta). \end{aligned} \quad (23)$$

As before,^{1,2} both the forward and backscattering cross sections are $O(\tau^2)$ for the rigid surface and $O(\tau^4)$ for the free.

III. PROBABILITY DENSITY FUNCTION

Many essential features of R , $\sigma(f)$, and $\sigma(b)$ for a continuous distribution in boss size can be illustrated by numerical computations based on the Schulz⁵ version of the two-parameter gamma probability density function^{6,7} $P(t)$. The variable t serves as a dimensionless parameter multiplying one or more semidiameters of a boss; thus, for example, we consider bosses of fixed base area (fixed a and b) and randomized height (or depth tc), or fixed height c and randomized bases specified by ta and tb (a family of similar ellipses), as

The two-parameter gamma probability density function

$$P(t) = (1/\ell!) [(\ell + 1)/m]^{\ell+1} t^{\ell} e^{-(\ell+1)t/m}, \quad \ell = 0, 1, 2, \dots, \quad (25)$$

with m as the mean, is general enough to cover many of the cases of practical interest. The numbers ℓ and m specify all moments of the distribution,

$$\langle t \rangle = m, \quad \langle t^n \rangle = \langle t \rangle^n (\ell + n) / (\ell + 1)^n \ell!. \quad (26)$$

In terms of the normalized variance

$$\langle t^2 \rangle - \langle t \rangle^2 / \langle t \rangle^2 = 1/(\ell + 1) \equiv v, \quad 0 < v \leq 1, \quad (27)$$

we may rewrite the moments in the product form

$$\langle t^n \rangle = m^n (1 + v)(1 + 2v) \cdots [1 + (n - 1)v]; \quad (28)$$

all moments increase with increasing m and v . The magnitude of $v = 1/(\ell + 1)$ also determines the skewness of P .

The maximum value of P , attained for

$$t_{\Lambda} = m\ell/(\ell + 1) = m(1 - v) < m, \quad (29)$$

is given by

$$P_{\Lambda} = (\ell! + \ell/\ell!) e^{-\ell}. \quad (30)$$

For ℓ large ($v \approx 0$), P is Gaussian around $t = t_{\Lambda}$,

$$P \sim \frac{1}{(2\pi t_{\Lambda}^2 / \ell)^{1/2}} \exp \left(-\frac{(t - t_{\Lambda})^2}{2t_{\Lambda}^2 / \ell} \right). \quad (31)$$

If $\ell \rightarrow \infty$ ($v \rightarrow 0$), then $t_{\Lambda} \rightarrow m$ and P reduces to $\delta(t - m)$ to reproduce one-component results. More generally, the curve of P is skewed positively ($t_{\Lambda} < m$), and for $\ell = 0$ ($v = 1$), P reduces to $(1/m)e^{-t/m}$ for the Poisson case. In Fig. 1, we plot P vs t for several values of v and $m = 1$.

For computational purposes, we take $m = 1$ (so that t serves as a simple scaling factor) and restrict the range of t to $t > 0.5$. We work with

$$P(t) = (t'/P_0) e^{-(t'/P_0)}, \quad t' > 0.5,$$

$$P_0 = \int_{0.5}^{\infty} t' e^{-t'/P_0} dt'. \quad (32)$$

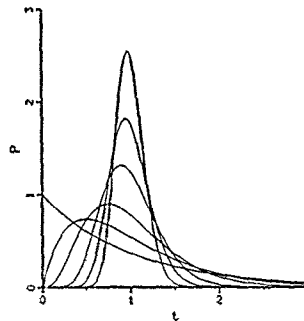


FIG. 1 Plot of the gamma probability density function P of Eq. (25) with mean $m = 1$ and normalized variance $v = 1/(\ell + 1)$ as the parameter. The higher curves at $t = 1$ apply for the smaller values of $v = 0.025, 0.05, 0.1, 0.25, 0.5$, and 1.0 . As v approaches zero, P approaches $\delta(t - 1)$.

To provide benchmark curves, we consider a one-component ($v=0$) distribution of aligned ellipsoidal bosses having semidiameters $(a,b,c) = (1,4,2)$ with $ka=20$ and $w=0.2$. For the continuous multicomponent cases, one or more semidiameters are multiplied by the dimensionless parameter t ; the required averages are based on (32). The restriction on the range of t insures that $ka>10$ for all bosses in the distribution, with d denoting any semidiameter; thus integration is restricted to ranges where the present high-frequency approximations suffice, and spurious contributions for small ka cannot arise. Physical considerations also require that boss size be bounded away from infinity; such truncation is implicit in the Gaussian quadrature routine used in the numerical integrations.

In the illustrations for R and the forward and back-scattered cross sections, $\sigma(f)$ and $\sigma(b)$, [written as $S(F)$ and $S(B)$ on the graphs to facilitate comparisons with earlier one-component versions], we plot versus angle (α) from the normal for rigid (+) and free (-) surfaces with v as the parameter. Curves for the rigid and free surfaces are overlaid; the rigid are shown solid and the free are dotted. Four values of $v = 1/(\ell+1)$ are considered:

$$v = 0.0, 0.25, 0.5, 1.0, \quad (33)$$

corresponding to $\ell = \infty, 3, 1, 0$. The one-component case is represented by $v=0$.

Although large numerical values are indicated for some of the $\sigma(f)$ curves, experimental design factors must be considered in determining the relative importance of coherent reflection and incoherent scattering contributions. For plane-wave incidence the net normalized energy flux is given by²

$$Rk + \int \int \frac{\sigma(\hat{s}, \hat{k}')}{|\mathbf{r} - \mathbf{r}_i|^2} \hat{s} \cdot d\mathbf{x}_i \cdot d\mathbf{y}_i,$$

where \hat{s} is a unit vector from a point \mathbf{r}_i on the surface to the observation point \mathbf{r} [see (2:75) ff]. Practical transducer beam factors are required for comparison with measurements.³

IV. NUMERICAL ILLUSTRATIONS

All graphs for R , $\sigma(f)$, and $\sigma(b)$ are based on computations with the complete forms of (11)–(13) supplemented by (1:15).

Figures 2–7 correspond to aligned bosses with fixed base semidiameters $(a,b) = (1,4)$ and height (or depth) tc as a random variable. Figures 2–4 apply for the azimuthal angle $\beta = 0^\circ$ (broadside incidence ± 1 grazing). The essentials for the R curves of Fig. 2 are indicated by the simple approximations (14)–(16). For this case, (15) reduces to

$$R \approx \left[1 - \frac{w}{2} \left(1 + \frac{c^2}{2a^2} \langle t^2 \rangle \tan^2 \alpha \right) \right]^2 \times \left[1 + \frac{w}{2} \left(1 + \frac{c^2}{2a^2} \langle t^2 \rangle \tan^2 \alpha \right) \right]^{-2}. \quad (34)$$

Although (34) is independent of statistics for $\alpha = 0$, the more complete form of R used for computations is not,

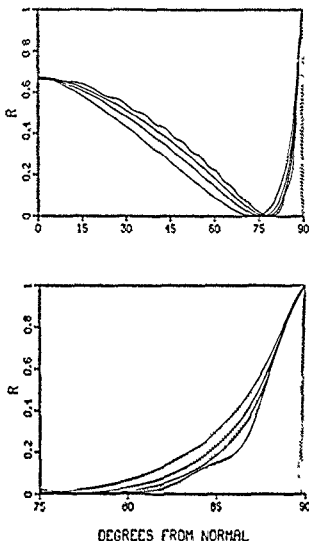


FIG. 2. Graphs of the reflection coefficient R of Eq. (9) for a continuous distribution of bosses having semidiameters $(a, b, tc) = (1, 4, t2)$, with probability density for t as in Eq. (32). The upper panel shows the full range of angle of incidence (α), while the lower shows the near-grazing region. The azimuthal angle is $\beta = 0^\circ$, corresponding to broadside incidence at grazing. The solid and dotted curves represent rigid (+) and free (-) surfaces, respectively. For α not near 0° or 90° , the higher curves apply for the smaller values of $v = 0.0, 0.25, 0.5$, and 1.0 ; near grazing the higher solid curves as well as the higher peaked dotted curves apply for the larger values of v .

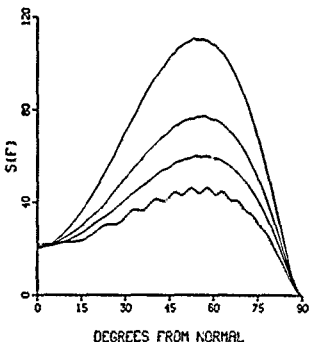


FIG. 3. The forward-scattering curves from Eq. (10) associated with R of Fig. 2. In general, the higher curves correspond to the larger values of v .

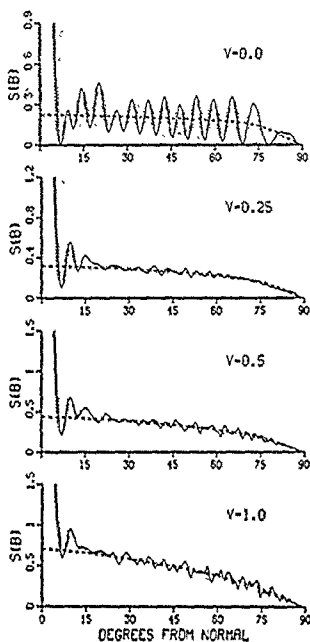


FIG. 4. The backscattering curves from Eq. (10) and dashed bases from Eq. (17) associated with R of Fig. 2. At normal incidence $S(B) = S(F)$ of Fig. 3.

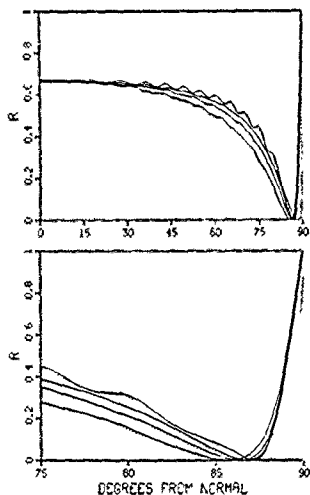


FIG. 5. Graphs of R for a distribution of bosses as in Fig. 2, but with azimuthal angle $\beta = 90^\circ$, corresponding to nose-on incidence at grazing. The higher curves for α not near grazing apply for the smaller values of $v = 0.0, 0.25, 0.5$, and 1.0 . Near grazing the higher solid curves and higher peaked dotted curves apply for the larger values of v .

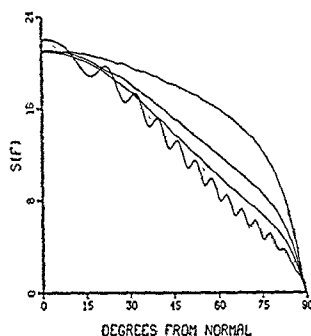


FIG. 6. The forward-scattering curves associated with Fig. 5. In general, the higher curves correspond to the larger values of v .

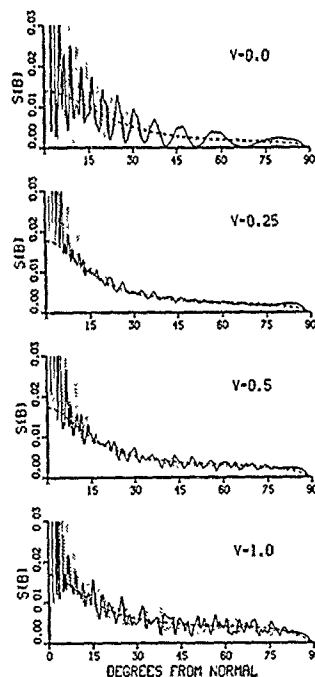


FIG. 7. The backscattering curves associated with Fig. 5.

which accounts for the slight difference in the curves at normal incidence. For $\alpha \neq 0$, R of (34) decreases with increasing v ; from (32), corresponding to the sequence for v in (33), we have $\langle r^2 \rangle = (1.0, 1.43, 2.0, 3.25)$. Near grazing, R_+ of (16) increases with v increasing

$$R_+ \sim 1 - 4a\tau/wc(t); \quad (35)$$

from (32), $\langle t \rangle = (1.0, 1.11, 1.25, 1.5)$. For α not too close to grazing, R_- also increases with v but the trend reverses very close to grazing where

$$R_- \sim 1 - k^2 wc^3 \langle t^3 \rangle \tau / a; \quad (36)$$

from (32), $\langle t^3 \rangle = (1.0, 2.18, 4.06, 9.88)$. The associated forward and backscattering are shown in Figs. 3 and 4. Except near normal incidence for the forward scattering, both $\sigma(f)$ and the base curves for the oscillations of $\sigma(b)$ increase with v . Analogous plots of R , $\sigma(f)$, and $\sigma(b)$ for $\beta = 90^\circ$ (nose-on incidence at grazing) are shown in Figs. 5-7

Figures 8-10 apply for a base semidiameter ta as a random variable and the remaining two semidiameters fixed. For α not near 90° , R of Fig. 8 increases with v , reversing the trend shown in the previous plots. For larger α , R_+ decreases with increasing v ; for α near grazing,

$$R_+ \sim 1 - 4a \langle t \rangle \tau / wc. \quad (37)$$

For the free surface, R_- decreases with increasing v for α not too close to grazing and then increases for larger α . For α close to grazing,

$$R_- \sim 1 - k^2 wc^3 \tau / a \langle t \rangle. \quad (38)$$

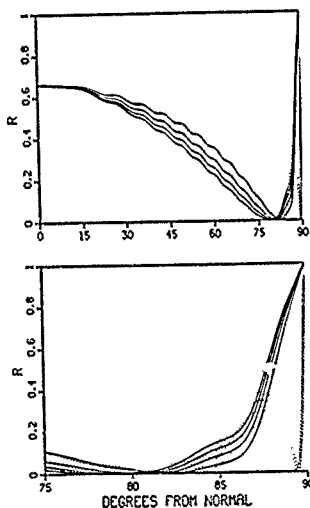


FIG. 8. Graphs of R for $(ta, b, c) = (1, 4, 2)$ with $\beta = 0^\circ$. The higher curves for α not near 90° apply for the larger values of $v = 0.0, 0.25, 0.5$, and 1.0 . In the lower panel, the higher solid curves near grazing and the higher peaked dotted curves correspond to the smaller values of v .

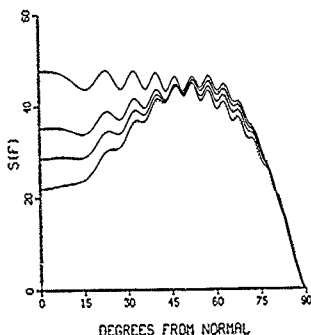


FIG. 9. The forward-scattering curves associated with Fig. 8. In general, the higher curves apply for the larger values of v .

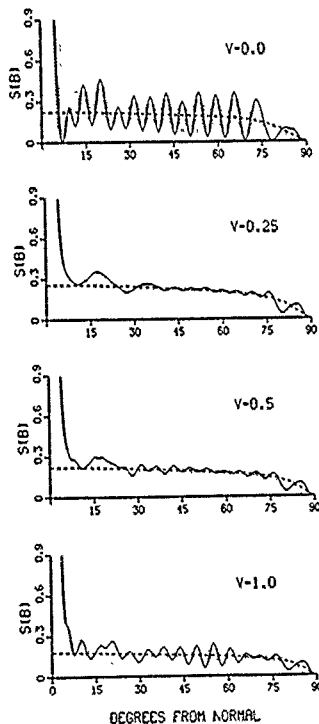


FIG. 10. The backscattering curves associated with Fig. 8

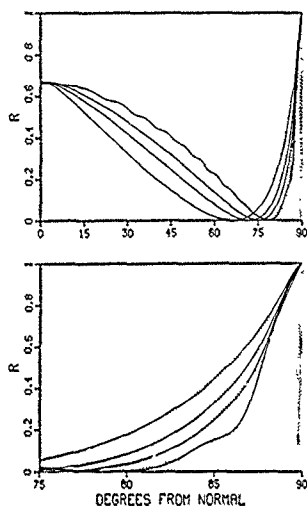


FIG. 11. Plots of R for $(a, b, c) = (1, 1, 2)$ with $\beta = 0^\circ$. For α not near 0° or 90° , the higher curves apply for the smaller values of $v = 0.0, 0.25, 0.5$, and 1.0 . In the lower panel, the higher solid curves and the higher peaked dotted curves apply for the larger values of v .

The associated forward and backscattering are shown in Figs. 9 and 10. At normal incidence,

$$\sigma_{\pm} \approx \omega k^2 ab \langle t^2 \rangle / 4\pi(t) (1 + \omega/2)^2, \quad (39)$$

with $\langle t^2 \rangle / \langle t \rangle$ increasing from 1.0 to 2.17 as v increases from zero to unity. The trend of increased scattering for the larger values of v continues for $\sigma(\alpha)$ until α is close to grazing (Fig. 9). The base curves for $\sigma(b)$ of Fig. 10 differ slightly, but the pattern of oscillations is altered as v changes.

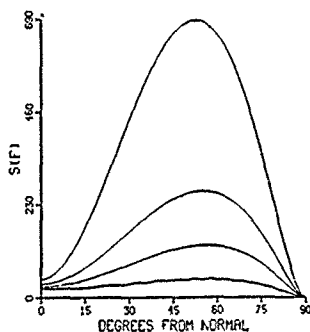


FIG. 12. The forward-scattering curves associated with Fig. 11. The higher curves apply for the larger values of v .

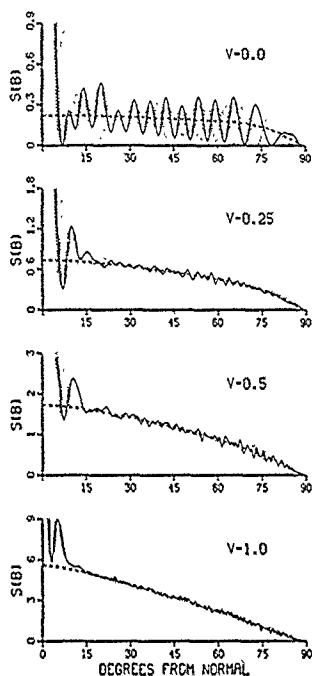


FIG. 13. The backscattering curves associated with Fig. 11.

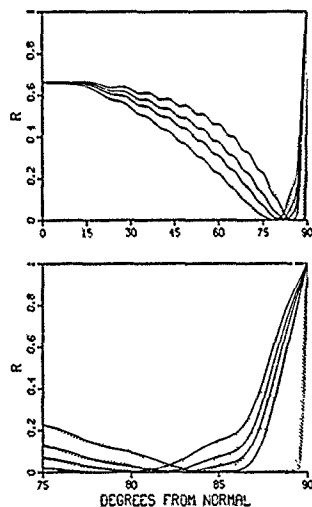


FIG. 14. Graphs of R for a distribution of bosses $(a, b, c) = (1, 1, 2)$ with $\beta = 0^\circ$. For α not near 90° , the higher curves apply for the larger values of $v = 0.0, 0.25, 0.5$, and 1.0 .

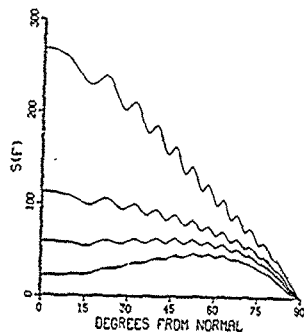


FIG. 15. The forward-scattering curves associated with R of Fig. 14. The higher curves apply for the larger values of v .

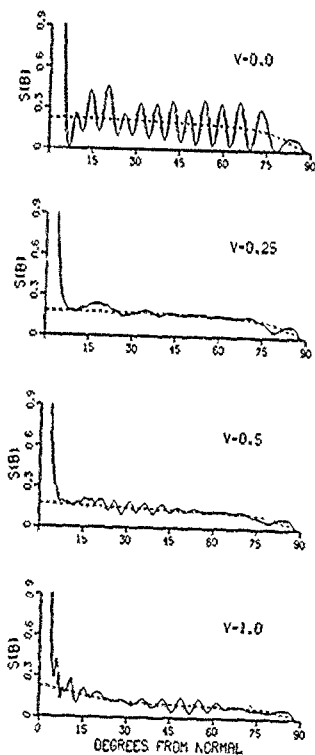


FIG. 16. The backscattering curves associated with R of Fig. 14.

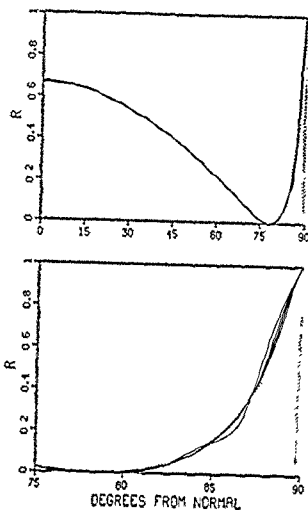


FIG. 17. Graphs of R for a distribution of bosses $(t_a, t_b, t_c) = (t_1, t_4, t_2)$ with $\beta = 0^\circ$. The curves differ little for α not near 90° . The higher solid curves for α near 90° apply for the smaller values of $v = 0.0, 0.25, 0.5, 1.0$; the higher peaked dotted curves apply for the larger values of v .

In Figs. 11–16, we fix one of the boss semidiameters and scale the remaining two by t . Figures 11–13 apply for base semidiameter a fixed and the remaining two specified by t_b and t_c (a family of similar ellipses in the yz plane). In Figs. 14–16, the boss height c is fixed and the base semidiameters are specified by t_a and t_b . In all cases, the essentials are indicated by the approximations (14)–(24).

The generalization (t_a, t_b, t_c) for a family of similar el-

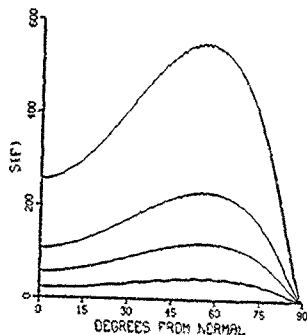


FIG. 18. The forward-scattering curves associated with R of Fig. 17. The higher curves apply for the larger values of v .

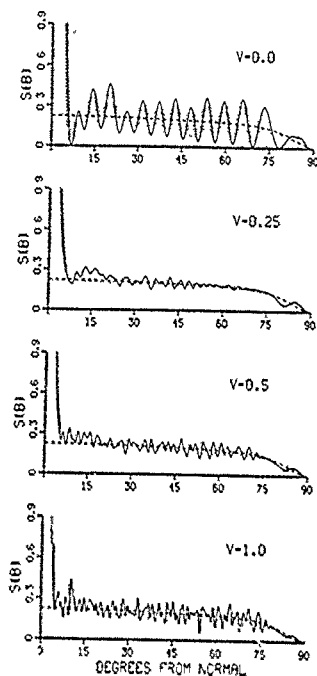


FIG. 19. The backscattering curves associated with R of Fig. 17.

lipsoids is illustrated in Figs. 17–19. For moderate values of α , (14) shows that R is independent of t , i.e., t cancels in $\langle abc\Gamma \rangle / \langle ab \rangle$; in this range, the R curves of Fig. 17 differ little, but additional structure appears for α close to grazing. The corresponding incoherent scattering, shown in Figs. 18 and 19, involves no such cancellation.

ACKNOWLEDGMENT

This work was supported in part by the Office of Naval Research.

¹R. J. Lucas and V. Twersky, "High-frequency reflection and scattering of sound by ellipsoidally embossed surfaces," *J. Acoust. Soc. Am.* **83**, 2005–2011 (1988).

²V. Twersky, "On scattering and reflection of sound by rough surfaces," *J. Acoust. Soc. Am.* **29**, 209–225 (1957).

³V. Twersky, "Reflection and scattering of sound by correlated rough surfaces," *J. Acoust. Soc. Am.* **73**, 85–94 (1983).

⁴R. J. Lucas and V. Twersky, "Low-frequency reflection and scattering by ellipsoidally embossed surfaces," *J. Acoust. Soc. Am.* **78**, 1838–1850 (1985).

⁵S. R. Aragon and R. Pecora, "Theory of dynamic light scattering from polydisperse systems," *J. Chem. Phys.* **64**, 2395–2404 (1976).

⁶I. Olkin, L. J. Gleser, and C. Derman, *Probability Models and Applications* (Macmillan, New York, 1989), p. 267 ff.

⁷V. Twersky, "Low-frequency scattering by mixtures of correlated non-spherical particles," *J. Acoust. Soc. Am.* **84**, 409–415 (1988).

⁸C. I. Beard, T. H. Kays, and V. Twersky, "Scattered intensities for random distributions, microwave data and optical applications," *Appl. Opt.* **4**, 1299–1315 (1965).

Regular polygonal arrays of resonant scatterers

Victor Twersky

Mathematics Department, University of Illinois, Chicago, Illinois 60680

(Received 20 May 1990; revised 21 October 1990; accepted 11 November 1990)

Numerical results for the scattering cross section (S) of $N = 3-26$ equally spaced monopole resonators on a circle (of radius b) indicate regularities in the values of the normalized diameter ($2kb = 4\pi b/\lambda = \rho$ with λ as the wavelength) corresponding to maximal scattering for symmetrical excitation. The peaks $S_\lambda(N)$ occur for $\rho = \rho_\lambda(N)$ between N and $2N$, i.e., for circle circumference between $N\lambda/2$ and $N\lambda$. With increasing N , the values of $\rho_\lambda(N)$ in successive alternating sets (shells) of three or four values of N are close to $\rho_m = 2m\pi - \pi/4$; shell-1 consists of $N = 3-5$, shell-2 of $N = 6-9$, shell-3 of $N = 10-12$, etc. The basis for the shell structure is delineated by a simple asymptotic approximation (for large ρ and N in the range $\rho < 2N$) of a cylindrical wave representation for a sum of spherical waves. A simple approximation is also derived for the shift in resonance frequency that occurs for ρ small enough for the array to respond as a collective monopole.

PACS numbers: 43.20.Fn, 43.30.Hw, 43.20.Bi

INTRODUCTION

A recent paper¹ on multiple scattering by regular arrays of N identical monopole resonators (of radius a and minimum separation $d > 2a$) analyzed seven cases including the first four polygonal arrays ($N = 3-6$) for arbitrary direction of incidence \mathbf{k} . It was shown that the scattering cross section S of each array² is less than twice its maximal single scattered value, and that the peak value S_λ for polygonal arrays occurs for broadside incidence ($\mathbf{k} = \mathbf{z}$). An introductory section¹ (II A), based on an earlier² tutorial illustration, indicated that similar results had been obtained numerically for $N = 24$ (and asymptotically for larger N), but reserved discussion of symmetrically excited polygonal arrays for this sequel. Initially, we consider numerical and graphical results for $N = 3-26$ resonators (on a circle of radius b) based on the original spherical wave form of the propagator set¹ $\mathcal{N} = \mathcal{J} + i\mathcal{I}$. Then we derive a cylindrical wave representation of \mathcal{J} and an asymptotic¹ approximation ($\tilde{\mathcal{J}}$) for large N that delineates the basis for the regularities indicated by computations for increasing N . The regularities suggested by data to $N = 12$ were substantiated to $N = 26$, and preserved in the asymptotic results.

The key variable is the normalized diameter $\rho = 2kb = 4\pi b/\lambda$ with λ as the wavelength. The peak $S_\lambda(N)$ occurs for $\rho = \rho_\lambda(N)$ between N and $2N$, i.e., for circle circumference between $N\lambda/2$ and $N\lambda$. With increasing N , successive alternating sets of three or four values of N are grouped into shells in the sense that the corresponding $\rho_\lambda(N)$ are close to

$$\rho_m = 2m\pi - \pi/4 = \pi(8m - 1)/4; \quad m = 1, 2, 3, \dots \quad (1)$$

Shell-1 consists of $N = 3-5$, shell-2 of $N = 6-9$, shell-3 of $N = 10-12$, etc. A peak $S_\lambda(N)$ in shell- m corresponds to the m th local minimum of the associated \mathcal{J} .

We start with a brief sketch of the spherical wave form development,¹ and then derive $\tilde{\mathcal{J}}$. The normalized frequency $x = ka$ at the peak is determined by its single scattered value x_λ and by $\mathcal{I}(\rho)$. The location ρ_λ of the lowest minimum of $\mathcal{J}(\rho)$ and the value $\mathcal{J}(\rho_\lambda) = \mathcal{J}_\lambda$ determine $x_\lambda(\rho_\lambda)$ and S_λ . Figures 1-7 correspond to shells 1-7 (and the captions provide the essential data at the peaks), they display \mathcal{J} as solid curves for $0 < \rho < 50$, and $\tilde{\mathcal{J}}$ as dashed curves for $4 < \rho < 2N$. The $\tilde{\mathcal{J}}(\rho)$ show the essentials to $\rho \leq \rho_\lambda$, at least for the larger values of N in a given shell.

The peaks S_λ occur for $x_\lambda \approx x_c$ and relatively large values of $\lambda d = y \gg x$, i.e., $\pi < y_\lambda < 2\pi$ corresponding to $\lambda/2 < d < \lambda$. For all cases $S_\lambda < 2N\sigma_s$, where σ_s is the maximum scattering cross section of an isolated resonator.

On the other hand, a large shift from x_c yielding $S = O(\sigma_s)$ occurs for small $y = x/p$ with $p = a/d < 1/2$. For small y , the array acts as a collective monopole with resonance frequency $x_0 < x_c$. Explicit results are given for $x_0(N, x, p)$, and a simple approximation for large N is included and compared with analogs.^{3,4} (The label resonance is used as in the acoustics scattering literature.^{5,6})

I. REGULAR POLYGONAL ARRAYS

A regular polygon with $s = 1$ to N vertices at $\mathbf{b}_s = b\hat{\mathbf{b}}_s$, respectively, is specified by

$$\begin{aligned} \hat{\mathbf{b}}_s &= \hat{x} \cos \mu_s + \hat{y} \sin \mu_s, \quad \mu_s = (s-1)2\mu, \quad \mu = \pi/N; \\ \sum_{s=1}^N \hat{\mathbf{b}}_s &= 0, \quad \sum_{s=1}^N e^{i\mu_s} = \sum_{m=0}^{N-1} e^{im(2\pi/N)} = 0. \end{aligned} \quad (2)$$

The smallest separation of vertices $|\mathbf{b}_{s+1} - \mathbf{b}_s| = 2b \sin \mu = d$ (an edge) subtends the angle 2μ at the center ($\mathbf{r} = 0$) of the circle of radius b . For $N = 2\nu$ or $2\nu + 1$ (even or odd), ν is the member of different separations of vertices that arise. All separations are expressed in terms of

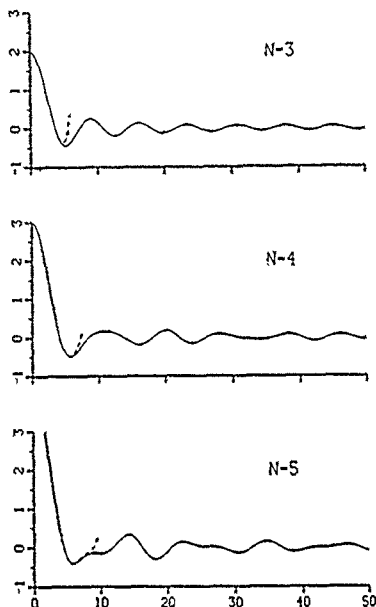


FIG. 1. Shell-1; the lowest minimum of f vs ρ for $N = (3, 4, 5)$ is the first $f \approx - (0.4345, 0.4820, 0.4071)$ at $\rho \approx (5.189, 5.666, 5.851)$ for which $\gamma \approx (0.0967, 0.1799, 0.2856)$. From these values, $B \approx - (1.768, 1.931, 1.687)$, $\gamma = (4.493, 4.006, 3.439)$, and $10^4 \chi = (137.49, 137.57, 137.67)$.

the smallest by $|b_i - b_j| = 2b \sin m\mu = (d/\sin \mu) \sin m\mu$, where $m = 1$ to v .

For a plane wave $\phi(r) = e^{ikr}$ incident on an isolated monopole at one of the vertices b_i , we write the scattered field for $|r - b_i| > a$ as

$$u(r - b_i) \phi(b_i) = a_0 h(k|r - b_i|) e^{i\alpha}, \quad (3)$$

$$h(\alpha) = h_0^{(1)}(\alpha) = e^{i\alpha}/i\alpha, \quad \delta_i = k \cdot b_i.$$

For a lossless resonator, and $x = ka \leq 0.1$,

$$a_0 = -\frac{1}{1 + i\gamma}, \quad \gamma = \frac{x_c^2 - x^2}{x^3}, \quad x_c^2 = \frac{3}{C}, \quad (4)$$

where C is the relative compressibility. At resonance, $x = x_c$, so that $\gamma = 0$ and $a_0 = -1$. The scattering cross section (σ) and its resonance value (σ_r) are given by

$$\sigma = -Re a_0 4\pi/k^2 = |a_0|^2 4\pi/k^2, \quad (5)$$

$$\sigma_r = 4\pi/k_c^2 = 4\pi a^2/x_c^2,$$

where σ reduces to σ_r at $x = x_c$. As before,¹ for illustrations we take $C = 1.589 \times 10^4$ and $x_c = 0.01374$ (appropriate for an air bubble in the sea^{6,7}) so that $\sigma_r \approx 2.12 \times 10^4 \pi a^2$. The peak width at half-power ($|a_0|^2 = 1/2$) is $\omega_1 \approx |x_c|^2$.

For ϕ incident on a polygonal array of N identical monopoles, we write the scattered field as

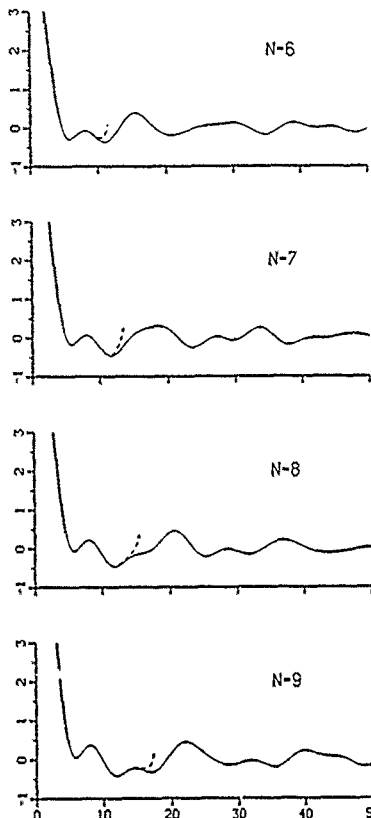


FIG. 2. Shell-2; the lowest minimum of f vs ρ for $N = (6, 7, 8, 9)$ is the second $f \approx - (0.3697, 0.4691, 0.4666, 0.4171)$ at $\rho \approx (11.10, 11.67, 11.96, 12.06)$ for which $\gamma \approx (-0.0733, -0.0070, 0.1136, 0.2138)$. From these, $B \approx - (1.586, 1.884, 1.875, 1.716)$, $\gamma = (5.551, 5.065, 4.578, 4.123)$, and $10^4 \chi = (137.33, 137.39, 137.51, 137.60)$.

$$u(r; \hat{k}) = \sum_i D_i(\hat{k}) h(k|r - b_i|) e^{i\alpha_i}, \quad (6)$$

$$D_i(\hat{k}) = a_0 \left(1 + \sum_{j \neq i} D_j(\hat{k}) h(k|b_i - b_j|) e^{-i(\delta_i - \delta_j)} \right). \quad (7)$$

The N coefficients $D_i(\hat{k})$ can be obtained by elementary algebra, and expressed in terms of $v + 1$ collective \hat{k} -independent oscillator mode coefficients B_n times \hat{k} -dependent exponentials.¹

For normal incidence ($\hat{k} = \hat{z}, \hat{z} \cdot \hat{b}_i = 0$), $D_i = D$ and

$$D = \frac{a_0}{1 - a_0 N_0} \equiv B, \quad N_0 = \sum_{i,j} h(k|b_i - b_j|) \equiv N, \quad (8)$$

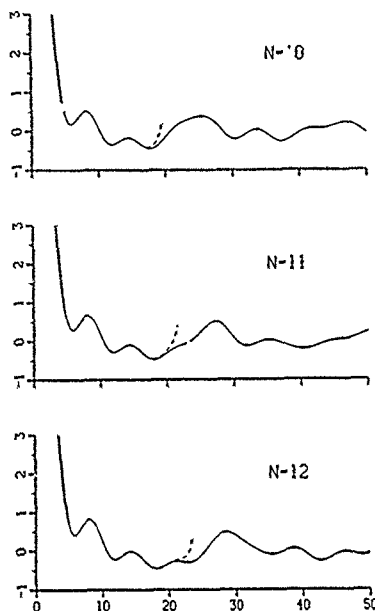


FIG. 3. Shell-3; the lowest minimum of f vs ρ for $N = (10, 11, 12)$ is the third. $f \approx (0.4469, 0.4773, 0.4670)$, $\rho \approx (17.74, 18.11, 18.26)$ for which $\epsilon \approx (-0.1000, -0.0012, 0.0983)$. From these, $B \approx (1.808, 1.913, 1.842)$, $y = (5.483, 5.102, 4.726)$, and $10^4 x = (137.3, 137.4, 137.49)$.

where $B = B_0$ is also the coefficient of mode 0. Although an individual $D_s(\hat{k})$ is not observable by measurements of \mathcal{H} for $r \gg b$, $D = B$ is observable since the corresponding scattered field is directly proportional to B :

$$\mathcal{H}(r; \hat{z}) = B \sum h(k|r-b_s|). \quad (9)$$

The field along the center line ($r = z$), and at the geometrical center ($r = 0$) are given by

$$\mathcal{H}(z; \hat{z}) = Bh(k\sqrt{z^2 + b^2})N, \quad \mathcal{H}(0; \hat{z}) = Bh(kb)N. \quad (10)$$

For arbitrary \hat{k} , we sum $D_s e^{i\mathbf{k} \cdot \mathbf{r}}$ over s and solve (7) directly for the sum to obtain

$$\sum D_s(\hat{k}) e^{i\mathbf{k} \cdot \mathbf{r}} = B \sum e^{i\mathbf{k} \cdot \mathbf{r}}.$$

Thus the corresponding field along the center line equals¹

$$\mathcal{H}(z; \hat{k}) = Bh(k\sqrt{z^2 + b^2}) \sum e^{i\mathbf{k} \cdot \mathbf{r}}, \quad \delta_s = k b_s, \quad (11)$$

so that B also suffices for this special case of nonsymmetrical excitation.

In the far field, r/b and kr large, (9) reduces to $\mathcal{H} \sim h(kr)\mathcal{S}$ where the scattering amplitude satisfies

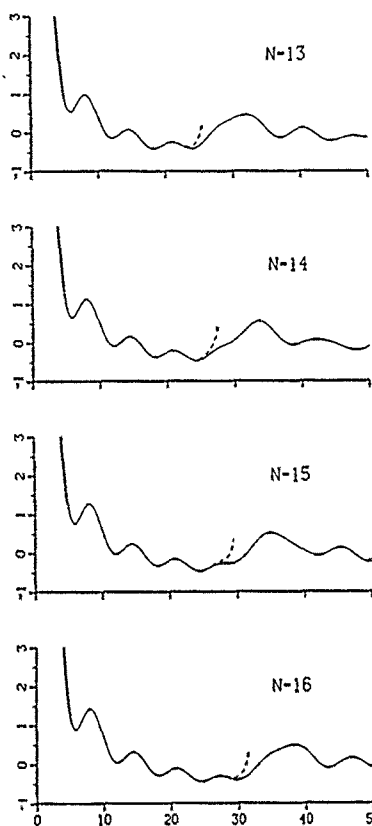


FIG. 4. Shell-4, the lowest minimum of f vs ρ for $N = (13, 14, 15, 16)$ is the fourth. $f \approx (0.4237, 0.4747, 0.4735, 0.4488)$, $\rho \approx (23.84, 24.26, 24.47, 24.54)$ for which $\epsilon \approx (-0.1785, -0.0869, 0.0096, 0.0945)$. From these, $B \approx (1.735, 1.904, 1.899, 1.814)$, $y = (5.705, 5.399, 5.088, 4.788)$, and $10^4 x = (137.23, 137.32, 137.41, 137.49)$.

$$\mathcal{S}(\hat{r}; \hat{z}) = \mathcal{S}(-\hat{z}, -\hat{r}) = B \sum e^{i\mathbf{k} \cdot \mathbf{r}}, \quad \Delta_s = k\hat{r} \cdot \mathbf{b}_s. \quad (12)$$

The forward scattered ($\hat{r} = \hat{z}$) and back scattered ($\hat{r} = -\hat{z}$) values are equal:

$$\mathcal{S}(\hat{z}; \hat{z}) = \mathcal{S}(-\hat{z}; \hat{z}) = BN. \quad (13)$$

The scattering cross section for the array is given by

$$S = R 4\pi/k^2 = R \sigma_s(x_s/x)^2, \quad R = -\text{Re } \mathcal{S}(\hat{z}; \hat{z}) = \int \frac{1}{4\pi} \mathcal{S}(\hat{r}; \hat{z}) \mathcal{S}^*(\hat{r}) d\Omega(\hat{r}). \quad (14)$$

The final form of S is normalized with respect to isolated monopole resonance values to provide benchmarks for comparisons.

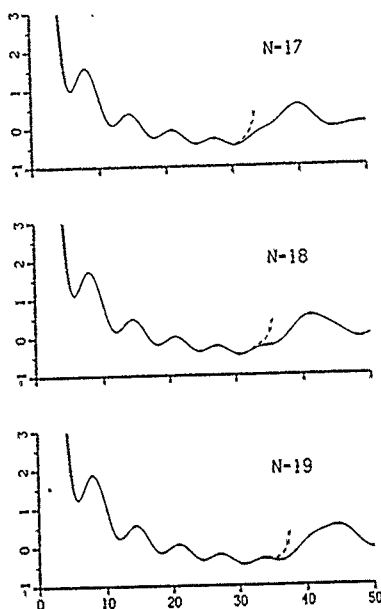


FIG. 5. Shell-5; the lowest minimum of f vs ρ for $N = (17, 18, 19)$ is the fifth. $f = (0.4664, 0.4797, 0.4659)$, $\rho = (30.42, 30.68, 30.79)$ for which $t = (-0.1556, -0.0624, 0.0228)$. From these, $B = (1.874, 1.922, 1.872)$, $\gamma = (5.59, 5.327, 5.067)$, and $10^3 x = (137.25, 137.34, 137.42)$.

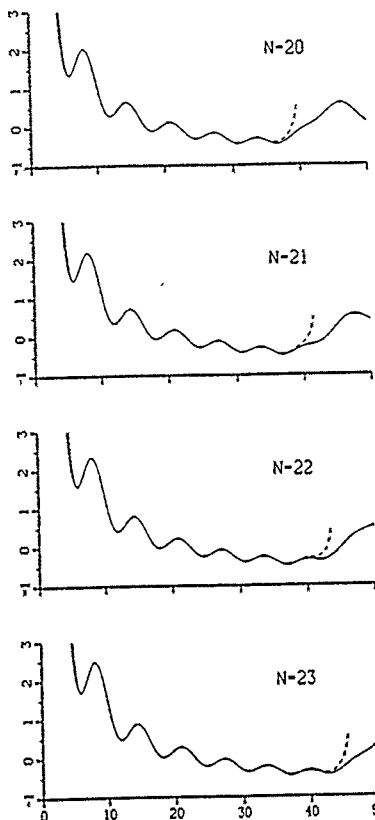


FIG. 6. Shell-6; the lowest minimum of f vs ρ for $N = (20, 21, 22, 23)$ is the sixth; $f = (0.4552, 0.4804, 0.4757, 0.4581)$, $\rho = (36.58, 36.88, 37.03, 37.08)$ for which $t = (-0.2131, -0.1233, -0.383, 0.0341)$. From these, $B = (1.836, 1.925, 1.907, 1.845)$, $\gamma = (5.723, 5.497, 5.269, 5.049)$, and $10^3 x = (137.2, 137.28, 137.36, 137.43)$.

II. MAXIMAL SCATTERING

For $N = 2v$ or $2v + 1$ (even or odd) in terms of $\epsilon_\infty = 1$ or 2, respectively, we write

$$\mathcal{H}(\rho) = \sum_{s=1}^{N-1} h(\rho_s) = 2 \sum_{s=1}^{N-1} h(\rho_s) + \epsilon_\infty h(\rho_s), \quad (15)$$

$$\rho_s = \rho \sin s\mu, \quad \rho = 2kb.$$

The real and imaginary parts are given by

$$\mathcal{H} = \sum j(\rho_s) + i \sum n(\rho_s) = \mathcal{J}(\rho) + i \mathcal{I}(\rho), \quad (16)$$

with $j(\alpha) = j_0(\alpha) = (\sin \alpha)/\alpha$ and $n(\alpha) = n_0(\alpha) = -(\cos \alpha)/\alpha$. Substituting (4) and (16) into (8) yields

$$B = -\frac{1}{1 + i\gamma + \mathcal{H}} = -\frac{1}{(1 + \mathcal{J})(1 + i\mathcal{I})},$$

$$\Gamma = \frac{\gamma + i\mathcal{I}}{1 + \mathcal{J}} = \Gamma(x, \rho), \quad (17)$$

which represents a more general resonator than a_0 .

We have

$$-N \operatorname{Re} B = N[(1 + \mathcal{J})(1 + \Gamma^2)]^{-1}$$

$$\leq N(1 + \mathcal{J})^{-1} \equiv R(\rho), \quad (17')$$

as well as $N|B| \leq R(\rho)$. Thus peak scattering requires minimal $1 + \mathcal{J}$ and

$$\Gamma = 0, \quad \gamma + i\mathcal{I} = (x_1^2 - x^2)/x^3 + i = 0. \quad (18)$$

Then, for any value of N ,

$$-\operatorname{Re} \mathcal{H}(\hat{z}, \hat{z}) = |\mathcal{H}(\hat{z}, \hat{z})|$$

$$= N/[1 + \mathcal{J}(\rho)] = R(\rho) = N|B(\rho)| \quad (19)$$

at the associated frequency

$$x = x_1/[1 - x_1 \mathcal{I}(\rho)]^{1/2}. \quad (20)$$

The peak magnitude $R_\Lambda = N|B_\Lambda|$ is determined by the value $\rho = \rho_\Lambda$ that minimizes $\mathcal{J}(\rho)$; the resulting value

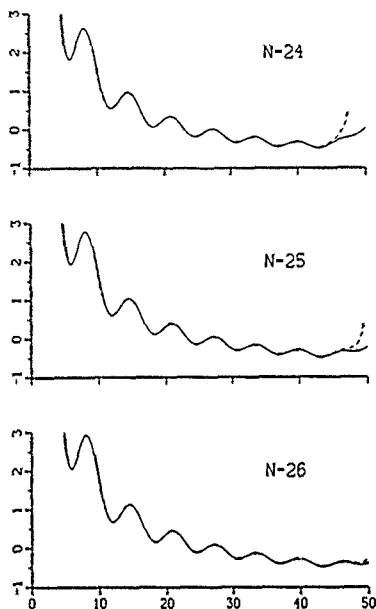


FIG. 7. Shell-7; the lowest minimum of f vs ρ for $N = (24, 25, 26)$ is the seventh. $f = -(0.4777, 0.4811, 0.4690)$, $\rho = (43.09, 43.26, 43.34)$ for which $f = -(0.1762, 0.0920, 0.0183)$. From these values, $B = -(1.915, 1.927, 1.883)$, $y = (5.624, 5.423, 5.224)$, and $10^3 x = (137.23, 137.31, 137.38)$.

$f(\rho_\lambda)$ then specifies the corresponding frequency x_λ , and from $\rho_\lambda/x_\lambda = 2b_\lambda/a = d_\lambda/a \sin \mu$ we obtain the appropriate circle diameter $2b_\lambda$, as well as the separation d_λ of neighbors.

The function f that determines R of (19), i.e.,

$$f(\rho) = \sum_{n=1}^N f_n(\rho) = \sum_{n=1}^N \frac{\sin[\rho \sin(n\pi/N)]}{\rho \sin(n\pi/N)}, \quad (21)$$

has maximum value $N-1$ for $\rho \approx 0$ (for which case $R \approx 1$), and vanishes as $\rho \rightarrow \infty$ (to yield $R \sim N$, the single scattered value).⁸ The solid curves in Figs. 1-7 for $N = 3-26$ (in successive alternating sets of three or four successive values of N) show f vs ρ for $\rho = 0-50$. As ρ increases, f decreases to its first local minimum, and then oscillates around an N -dependent base curve that also oscillates around zero. The zeros of the base curve are near ρ equal to integer multiples of N , and the lowest minimum f_λ occurs for $N < \rho_\lambda < 2N$ (between the first two zeros). The values of f_λ range from about -0.482 to about -0.37 (and of $|B_\lambda|$ from about 1.93 to about 1.59) with smallest and largest f_λ for $N = 4$ and 6 , respectively. The values of $\rho_\lambda/2N$ range from about 0.585 (for $N = 5$) to about 0.925 (for $N = 6$); the $y = 2\pi d/\lambda$ satisfy $3.439 < y_\lambda < 5.723$ with the smallest

value of d/λ about 0.547 (for $N = 5$), and the largest about 0.911 (for $N = 20$).

Each figure m corresponds to shell- m containing those values of N for which f_λ is the m th local minimum. The values of ρ_λ in shell- m are near ρ_m of (1), and the mean of ρ_λ for shell- m is even closer to ρ_m , the mean is within 1.3% of $\rho_1 = \pi/4$ for shell-1, and within 1% of ρ_m for the remaining shells. The captions list f_λ, ρ_λ , etc., but suppress the subscript. (The dashed curves for $4 < \rho < 2N$ are discussed subsequently.)

The resonance frequencies determined by (20) in terms of

$$f(\rho) = - \sum_{n=1}^{N-1} \frac{\cos[\rho \sin(n\pi/N)]}{\rho \sin(n\pi/N)}, \quad \rho = \rho_\lambda, \quad (22)$$

differ little from $x_\lambda = 0.01374$. The largest value of $f(\rho_\lambda)$ is about 0.286 for $N = 5$, and the smallest is about -0.213 for $N = 20$. The associated resonance frequencies obtained from $x_\lambda \approx x_c(1 + x_c f/2)$ are about 0.013767 and 0.013732 ; the departures from x_c are within 0.2% for $N = 3-26$. Thus $S_\lambda = R_\lambda(x_c/x_\lambda)^2$ approximates $R_\lambda = N|B_\lambda|$ to within 0.4% . The peak width at half-power $(|B|^2 = |B_\lambda|^2/2, \Gamma = \pm 1)$,

$$w_\lambda \approx x_\lambda^2(1 + f_\lambda)/(1 - x_\lambda f_\lambda) \\ = w_c(1 + f_\lambda)/(1 - x_\lambda f_\lambda)^2, \quad (23)$$

approximates $w_c(1 + f_\lambda)(1 + 2x_c f_\lambda)$, thus w_λ is of order $w_c/2$.

From the values in the figure captions for $N = 3-26$ (and for larger N based on the asymptotic form in the next section),

$$f_\lambda > -0.5, \quad -\text{Re } B_\lambda = |B_\lambda| < 2,$$

$$R_\lambda = -\text{Re } S_\lambda = |S_\lambda| < 2N, \quad S_\lambda < 2N\sigma_c. \quad (24)$$

The values of $|S_\lambda|$ and S are in accord with elementary considerations of interference processes. The central value (or values) of $|B_\lambda|$ in a given shell are the highest, and only the mean of shell values for m odd or even show consistent trends; the sequence of means for m odd (1.795, 1.854, 1.889, 1.908) and for m even (1.765, 1.848, 1.878) appear to increase slowly toward 2. A similar trend applies for the mean of shell values for y_λ : the sequence of means for m odd (3.979, 5.104, 5.328, 5.429) and for m even (4.829, 5.245, 5.384) appear to increase toward 2π .

III. ASYMPTOTIC FORM

We start with (21) plus $f(\rho_\lambda) - 1 = 0$, i.e.,

$$f(\rho) = -1 + \sum_{n=1}^N f_n(\rho), \quad \rho = \rho \sin \mu, \quad \rho = \rho \sin \frac{\pi}{N}, \quad (25)$$

and derive an alternative exact representation in terms of cylindrical functions.

Expressing $f(\rho)$ as

$$f(\rho) = \frac{\sin(\rho \sin \mu)}{\rho \sin \mu} = \frac{1}{\rho} \int_0^\pi \cos(v \sin \mu) dv, \quad (26)$$

and expanding the integrand in terms of Bessel functions

$$\cos(v \sin \mu_r) = J_0(v) + 2 \sum_{n=1}^{\infty} J_{2n}(v) \cos \frac{2n\pi}{N}, \quad (27)$$

enables us to sum over s

$$\sum_{s=1}^N \cos \frac{s2n\pi}{N} = N\delta_{n/N}, \quad l=0,1,2,\dots, \quad (28)$$

to obtain

$$\begin{aligned} \tilde{f} &= -1 + \frac{N}{\rho} \int_0^{\rho} dv \left[J_0(v) + 2 \sum_{l=1}^{\infty} J_{2l/N}(v) \right] \\ &\approx -1 + I_0 + \sum I_{2l/N}. \end{aligned} \quad (29)$$

This expression is exact for all ρ and N , but the range $N < \rho < 2N$ for large N is of primary interest.

To approximate I_0 for large ρ , we write

$$\int_0^{\rho} J_0(v) dv = \int_0^{\rho} J_0(v) dv - \int_{\rho}^{\infty} J_0(v) dv = 1 - \int_{\rho}^{\infty} J_0(v) dv, \quad (30)$$

and use the leading term of the Poisson asymptotic form¹ for large v ,

$$J_0(v) \sim (2/\pi v)^{1/2} \cos(v - \pi/4). \quad (31)$$

Thus

$$I_0 \sim (N/\rho) \{1 + (2/\pi\rho)^{1/2} \sin(\rho - \pi/4)\} \approx \tilde{I}_0(\rho). \quad (32)$$

The remaining terms I_l with $v = 2lN$ for $0 < \rho < v_l$ can be expressed in terms of the Carlini asymptotic form¹ for large v_l

$$\begin{aligned} J_l &\sim \frac{\xi^{1/2} \exp(\sqrt{1-\xi^2})}{(2\pi v_l)^{1/2} (1-\xi^2)^{1/4} (1+\sqrt{1-\xi^2})^{1/4}} \\ &\approx \tilde{J}_l, \quad \xi = \frac{\rho}{v_l} < 1. \end{aligned} \quad (33)$$

For $\rho \approx 0$, $\tilde{J}_l \approx (\rho/2)^{1/2} [e^{1/2} / \sqrt{2\pi v_l}]$ which differs from $J_l \approx (\rho/2)^{1/2} v_l^{-1}$ in that v_l has been replaced (appropriately) by Sterling's approximation. The asymptotic form of I_l follows from Watson,¹

$$I_l = \frac{\rho}{2} \int_0^1 J_l(v) dv \sim \frac{\tilde{J}_l}{\sqrt{1-\xi^2}}. \quad (34)$$

For $\rho < 2N$, we need retain only the $l=1$ term corresponding to $v=2N$.

The essentials are shown by the leading terms for $4 < \rho < 2N$:

$$\begin{aligned} \tilde{f} &\sim -1 + \tilde{I}_0 + \tilde{I}_{2/N} \approx \tilde{f}, \\ \tilde{f} &= -1 + \frac{N}{\rho} \left[1 + \left(\frac{2}{\pi\rho} \right)^{1/2} \sin\left(\rho - \frac{\pi}{4}\right) \right] \\ &\quad + \frac{1}{2(\pi N)^{1/2} (1-\xi^2)^{1/4}} \left[\frac{\xi \exp(\sqrt{1-\xi^2})}{1+\sqrt{1-\xi^2}} \right]^{2N}, \end{aligned} \quad (35)$$

where $\xi = \rho/2N < 1$. As ρ increases, the oscillatory decreasing term \tilde{I}_0 is positive with minima for $\sin(\rho - \pi/4) = -1$ at $\rho = \rho_m$ of (1). The positive monotonically increasing term $\tilde{I}_{2/N}$ increases slowly as ρ increases through N and is

practically negligible until ρ nears the vicinity of ρ_A where it rises rapidly to truncate the oscillations and delineate the smallest value of \tilde{f} . The lowest local minimum of \tilde{f} (the dashed curves in Figs. 1-7) corresponds to the largest or next to the largest value of ρ_m before ρ gets close enough to $2N$ for \tilde{f} to rise more steeply than \tilde{f} toward zero. The figures indicate that $\tilde{f}_A > \tilde{f}'_A > -1/2$, and computations with \tilde{f} for much larger values of N also yield $\tilde{f}_A > -1/2$.

For very large N , we have $\xi = \rho/2N \approx y/2N \times \sin(\pi/N) \sim y/2\pi$. Since (35) requires $\xi < 1$, it follows that $\pi/y > 1/2$. Thus with increasing N and ρ ,

$$\tilde{f} \sim -1 + N/\rho \sim -1 + \pi/y > -1/2 \quad (36)$$

and $\{B\} < 2$. For the infinite periodic line of monopoles⁴ and the case of one propagating mode, the results $y = kd < 2\pi$ and

$$\tilde{f}' = 2 \sum_l j(sy) = -1 + \pi/y > -1/2 \quad (37)$$

are rigorous. See Appendix A.

IV. LARGE SHIFTS OF RESONANCE FREQUENCY

For small ρ , corresponding to very small $y \approx x/\rho > 2x$, the array amplitude $\mathcal{S}(\hat{r}, \hat{z})$ reduces to that of a collective monopole (A_0) with $S = O(\sigma_c)$ at a resonance frequency x_0 , relatively far from the isolated resonance value x_c . Expanding \tilde{f} and y to $O(\rho^2)$ and evaluating the elementary sums yields

$$\tilde{f} + 1 = N [1 - \rho^2/12 + O(\rho^4)] \approx N, \quad (38)$$

$$I' = -\frac{1}{y} \left[C_N - \rho^2 \cos^2 \frac{\mu}{2} + O(\rho^4) \right] \approx -\frac{C_N}{y}, \quad (39)$$

$$C_N = \sum_{l=1}^N \frac{\sin(\pi/N)}{\sin(s\pi/N)} > 2, \quad N = 3, 4, \dots, \quad (40)$$

where the leading terms suffice for sufficiently small ρ and moderately large C_N .

For such cases,

$$\begin{aligned} \mathcal{S}(\hat{r}, \hat{z}) &\approx NB = A_0, \quad A_0 = -1/(1 + i\Gamma_0), \\ \Gamma_0 &= \frac{\gamma - C_N/y}{N} = \frac{x_c^2 - x^2(1 + \rho C_N)}{Nx^4}, \end{aligned} \quad (41)$$

with resonance frequency

$$x_0 = x_c / (1 + \rho C_N)^{1/2} < x_c. \quad (42)$$

At resonance, $\Gamma_0 = 0$ and $-\text{Re } \mathcal{S} = |\mathcal{S}| = 1$. The corresponding scattering cross section of the array satisfies

$$S = \sigma_c (x_c/x_0)^2 = \sigma_c (1 + \rho C_N) > \sigma_c. \quad (43)$$

At half-power, $\Gamma_0(x_c) = \pm 1$; the first approximation for the peak width $w_0 = x_+ - x_-$, i.e.,

$$w_0 \approx Nx_0^2 / (1 + \rho C_N) = Nx_c^2 / (1 + \rho C_N)^{3/2}, \quad (44)$$

suffices to indicate the trend with increasing N , but more complete results follow from (41). Discounting the immediate neighborhood of the contact value $\rho = 1/2$ (for which higher-order multipole coupling terms are required) we use $\rho = 1/4$ for illustrations. Inclusion of the leading monopole-dipole coupling effects leads to

$$p \Rightarrow p(1 - \beta p^3), \quad (45)$$

where $\beta = 1.5; 1.3536, 1.1180, 0.9137$ for $N = 3, 4, 5, 6$. However, the larger values of N and coupling with higher-order multipoles have not been investigated.

For $N = 3-9$, C_N (rounded off in general) is given by

$$C_N \approx 2, 2.707, 3.236, 3.665, 4, 4.293, 4.549, \quad (46)$$

For $p = 1/4$, S/σ_c increases from 1.5 to 2.137, x_0/x_c decreases from 0.816 to 0.684, and w_0/w_c increases from 1.33 to 1.97. For $N = 10-16$,

$$C_N \approx 4.774, 4.976, 5.16, 5.327, 5.482, 5.625, 5.758. \quad (47)$$

For $p = 1/4$, S/σ_c increases from 2.194 to 2.44, x_0/x_c decreases from 0.675 to 0.642, and w_0/w_c increases from 2.08 to 2.69. For $N = 17-23$,

$$C_N \approx 5.583, 6.001, 6.111, 6.216, 6.316, 6.411, 6.501. \quad (48)$$

For $p = 1/4$, S/σ_c increases from 2.471 to 2.647, x_0/x_c decreases from 0.636 to 0.617, and w_0/w_c increases from 2.78 to 3.34. All values of w_0/w_c are based on (44).

The increase of C_N with increasing N is essentially logarithmic, as shown explicitly by a simple approximation based on the leading terms of Euler's formula:

$$\sum_{j=1}^N f(s) \sim \frac{1}{2} f(1) + \frac{1}{2} f(N-1) + \int_1^N f(s) ds. \quad (49)$$

Thus

$$C_N \sim \left(\sin \frac{\pi}{N} \right) \left(\frac{1}{\sin(\pi/N)} + 2 \int_1^{N-1} \frac{ds}{\sin(\pi s/N)} \right) \\ = 1 + \frac{2N}{\pi} \left(\sin \frac{\pi}{N} \right) \ln \left(\cot \frac{\pi}{2N} \right). \quad (50)$$

and using $\sin(\pi/N) \approx \pi/N$ yields

$$C_N \sim 1 + 2 \ln(2N/\pi) \approx \tilde{C}_N. \quad (51)$$

For $N = 6-8$, \tilde{C}_N is within 1% for C_N , and for $N > 8$ the differences are less than or about 2%. For $N > 12$, we obtain better accord by using

$$C_N \sim \tilde{C}_{N+1} = 1 + 2 \ln[(2N+1)/\pi]. \quad (52)$$

where \tilde{C}_{N+1} is within 1% of the values of C_N given in (47) and (48) for $N = 13-23$. For $N = 24$, we have $C_{24} = 6.588$ and $\tilde{C}_{24}/C_{24} = 1.008$.

The final form of (39) requires that ρ^2/C_N be small for the form of the resonance frequency x_0 in (42) to apply. We obtain a bound for N for an accuracy (e.g., 2%) by using $\rho \sim Ny/\pi = Nx/\pi p$ to construct

$$\rho_0/\sqrt{\tilde{C}_N} = Nx_0/\pi p \sqrt{\tilde{C}_N} = Nx_0/\pi p [C_N(1 + pC_N)]^{1/2} \quad (53)$$

in terms of $C_N \sim \tilde{C}_N$. Thus for N to 37 at $p = 1/4$, we have $\rho_0^2/\tilde{C}_N < 0.02$ corresponding to $\rho_0 \approx 0.383$ and $\tilde{C}_{38} \approx 7.372$, i.e., for these values $\rho \approx C_N/y$ to within 2%, and $\rho \approx 1 \pm N$ to within 1.23%; for this case, $x_0/x_c \approx 0.59$, $S/\sigma_c \approx 2.84$, and $w_0/w_c \approx 4.58$ based on (44).

ACKNOWLEDGMENT

This work was supported in part by the Office of Naval Research.

APPENDIX A: PERIODIC LINE OF MONOPOLES

For ϕ incident normally to an infinite number of monopoles with spacing d along the z axis, we obtain the forms (8) and (9) in terms of different sums. As discussed before,⁴

$$B = \frac{a_0}{1 - a_0 \mathcal{H}}, \\ \mathcal{H} = 2 \sum_{n=1}^{\infty} h(kd, n) \frac{kd}{2\pi} = v \neq n, \quad n = (1, 2, 3, \dots), \quad (A1)$$

$$\mathcal{H} = B \sum_{n=1}^{\infty} h(k|r-s|dz) \equiv B\mathcal{H}'. \quad (A2)$$

For the excluded integer values of $kd/2\pi$ (which correspond to analogs⁴ of the Wood anomalies), \mathcal{H} reduces to the harmonic series and diverges logarithmically. However, since $|r-s|dz \approx |sd| \pm z$ for sufficiently large $|s|$, we have $\mathcal{H} = \mathcal{H}' + (e^{i\pi/2} + e^{-i\pi/2})/2$, where \mathcal{H}' is finite for $v \neq n$. Thus

$$\lim_{v \rightarrow n} \mathcal{H} = \lim_{v \rightarrow n} \frac{a_0[\mathcal{H}' + \mathcal{H} \cos kz]}{1 - a_0 \mathcal{H}} = -\cos kz \quad (A3)$$

corresponding to a standing wave along the axis of the array. There are no singularities in \mathcal{H} for any such multiple scattering problems. (See analogous development⁴ for the doubly periodic infinite planar array.)

We transformed⁴ \mathcal{H} to an infinite set of conical-cylindrical waves

$$\mathcal{H} = \frac{B\pi}{kd} \sum_{n=0}^{\infty} e^{i\pi/4} H_n^{(1)}(kR \cos \theta_n), \\ \sin \theta_n = 2n\pi/kd, \quad n = (0, \pm 1, \pm 2, \dots), \quad (A4)$$

where $R = \sqrt{r^2 - z^2}$ is the distance perpendicular to the axis, and $m < kd/2\pi < m+1$, with $m = 0$ or an integer. The values $|\sin \theta_n| < 1$ and $\cos \theta_n = \sqrt{1 - \sin^2 \theta_n}$ for $|n| < m$ specify $2m+1$ propagating modes, the values $|\sin \theta_n| > 1$ and $\cos \theta_n = i|\cos \theta_n|$ for $|n| > m$ specify an infinite number of evanescent modes; grazing modes correspond to the limit of \mathcal{H} for $|\sin \theta_n| \rightarrow 1$, the equivalent of (A3).

The \mathcal{H} sum is elementary:

$$\mathcal{H} = \frac{2}{ikd} \sum_{n=1}^{\infty} \frac{e^{i\pi/4}}{s} = -\frac{2}{ikd} \ln(1 - e^{i\pi/4}) = \mathcal{J} + i\mathcal{I}, \quad (A5)$$

$$\mathcal{J} = \frac{\pi}{kd} (2m+1) - i,$$

$$\mathcal{I} = \frac{2}{kd} \ln \left| 2 \sin \frac{1}{2} (kd - 2m\pi) \right|. \quad (A6)$$

For closure with the development of (A3), we note that $kd - 2m\pi = kd(1 - \sin \theta_m)$, so that if $\theta_m = \pi/2 - \epsilon$ with ϵ small (near grazing), then $\sin \theta_m \approx 1 - \epsilon^2/2$ and $\cos \theta_m \approx \epsilon$. The dominant term of \mathcal{H} is

$$i\mathcal{I} \approx \frac{i2}{kd} \ln \left(\frac{kde^2}{2} \right) \approx \frac{i4}{kd} \ln \epsilon.$$

Similarly, the dominant terms of α, B of (A4) involve

$$H_0^{(1)}(kR \cos \theta_m) \approx \frac{i2}{\pi} \ln \epsilon,$$

so that

$$\psi/B \approx \frac{\pi}{kd} (e^{ikz} + e^{-ikz}) \frac{i2}{\pi} \ln \epsilon$$

The limit of ψ for $\theta_m \rightarrow \pi/2, \epsilon \rightarrow 0$, is identically (A3)

Since $kd/2\pi < m+1$, it follows that

$$f' > \frac{2m+1}{2m+2} - 1 > -\frac{1}{2}, \quad f' > -\frac{1}{2}. \quad (A7)$$

The smallest value of f' arises for $m=0$ corresponding to $kd < 2\pi$, the case of only one propagating mode.⁴ To facilitate comparison with (37) and other forms in the text, we revert to $y = kd$.

For $2x < y < 2\pi$, we have

$$f' = \frac{\pi}{y} - 1 > -\frac{1}{2}, \quad f' = \frac{2}{y} \ln \left| 2 \sin \frac{y}{2} \right| \quad (A8)$$

and

$$B = -\frac{1}{(f' + 1)(1 + i\Gamma)} = -\frac{y}{\pi(1 + i\Gamma)},$$

$$\Gamma = \frac{y + i}{1 + f'} = \frac{y}{\pi} (y + i), \quad (A9)$$

The corresponding propagating part of α is a simple two-dimensional cylindrical wave

$$\alpha_p = \frac{B\pi}{y} H_0^{(1)}(kR) = -\frac{H_0^{(1)}(kR)}{1 + i\Gamma} \equiv \alpha_0 H_0^{(1)}(kR), \quad (A10)$$

with monopole coefficient α_0 equal to -1 at the resonances determined by $\Gamma = 0$. The evanescent modes depend on

$$kR \cos \theta_n = i(R/d) \sqrt{(2n\pi)^2 - (kd)^2}$$

and decay exponentially as $\exp(-R2n\pi/d)$ with increasing n . For large R/d and large kR ,

$$\alpha \sim \alpha_0 (2/\pi kR)^{1/2} e^{i\pi/4} \quad (A11)$$

is the appropriate far field form for a cylindrical monopole.

From (A9) with y as in (4), the resonance frequencies correspond to

$$x^2 = \frac{x_0^2}{1 - x_0^2} = \frac{x_0^2}{1 - 2x_0/y \ln |2 \sin y/2|}. \quad (A12)$$

Thus for $y = 5.723$, the largest value that arose for the polygons (the case $N=20$), we obtain $f' \approx -0.451$, $f' \approx -0.207$, and $x \approx x_0(1 + x_0 f'/2) \approx 0.01372$ (as compared to the polygonal values $f' \approx -0.455$, $f' \approx -0.213$, and $x_0 \approx 0.01372$). For $y = 6$, we have $f' \approx -0.4764$, $f' \approx -0.4217$, and $x = 0.01370$. The corresponding peak

widths at half-power are of order $w_c/2$ as discussed for (23), i.e., $w/w_c \approx 0.546$ and 0.518 .

For small $y = x/p$,

$$x^2 \approx x_c^2/(1 - 2p \ln y) = x_c^2/(1 + 2p \ln p/x). \quad (A13)$$

For $p = 1/4$, we have $x/x_c \approx 0.6087$; this is practically the same as the value at $N = 27$ based on (42) in terms of (52).

To delineate the relation of $\alpha_0 = -(1 + i\Gamma)^{-1}$ for small $y = x/p$ to the analogous result for the circular cylinder,⁵ we write

$$\Gamma = \frac{(3/C) - x^2[1 + 2p \ln(p/x)]}{x^2 \pi p}. \quad (A14)$$

At resonance, $\Gamma = 0$ reproduces x of (A13) with $x_c = (3/C)^{1/2}$. The corresponding scattering coefficient $\alpha_0^{(2)} = -(1 + i\gamma^{(2)})^{-1}$ of a two-dimensional monopole resonator for small x is given by⁵

$$\gamma^{(2)} = \frac{(2/C) - x^2 \ln(2/c_0 x)}{x^2 \pi/2}, \quad c_0 = 1.78107. \quad (A15)$$

At resonance, $\gamma^{(2)} = 0$ for $x = x_0 \approx 0.0048 \approx 0.3496x_c$; the value x_0 is smaller than any physically realizable value based on (A13), i.e., for $p < 1/2$ we require $x > 0.428x_c \approx 0.0059$.

For α_0 based either on (A14) or on (A15), the scattering cross section per unit length is given by $|\alpha_0|^2 4\pi/k = |\alpha_0|^2 (4\pi/x)$ with $|\alpha_0|^2 = 1$ at the resonance value of x .

¹ V. Twersky, "Multiple scattering by finite regular arrays of resonators," *J. Acoust. Soc. Am.* **87**, 25-41 (1990).

² V. Twersky, "Multiple scattering by arbitrary configurations in three dimensions," *J. Math. Phys.* **3**, 88-91 (1962). See tutorial illustrations in V. Twersky, *J. Opt. Soc. Am.* **52**, 145-171 (1962).

³ G. N. Watson, *Treatise on the Theory of Bessel Functions* (Cambridge, U.P. New York, 1944). The Poisson (1823) form is discussed on p. 10. The earlier Carlini (1817) form is considered on p. 7 and its integral is given on p. 255.

⁴ V. Twersky, "Multiple scattering of sound by a periodic line of obstacles," *J. Acoust. Soc. Am.* **53**, 96-112 (1973). The analogous development for the doubly periodic planar array mentioned after (A3) and other related results are given in V. Twersky, *J. Math. Phys.* **16**, 633-666 (1975).

⁵ V. Twersky, "Acoustic bulk parameters of random volume distributions of small scatterers," *J. Acoust. Soc. Am.* **36**, 1314-1329 (1964). See development of the two-dimensional case in (46)-(51) for $b_{30} = 1/\gamma^{(2)}$.

⁶ R. Wildt, Ed., "Acoustic theory of bubbles," in *Physics of Sound in the Sea*, NDRC Summary Tech. Rep. Div. 6, Chap. 28, Vol. 8 (Washington, DC, 1946).

⁷ G. Gaunard, K. P. Schamhorst, and H. Ueberall, "Giant monopole resonances," *J. Acoust. Soc. Am.* **65**, 573-594 (1979).

⁸ The derivative of $f(p)$ vanishes at an infinite number of points $p = p_i(N)$ corresponding to an infinite number of extrema where $f(p_i) = J(p_i)$ with $J(p) = \sum \cos(p \sin(\pi r/N))$. The intersections of the curves of $J(p)$ with the curves in Figs. 1-7 help determine $p_i = p_x$ and the values of the two different functions at $p = p_x$ provide checks on numerical computations.

Comments on resonant systems of scatterers

Victor Twersky

Mathematics Department, University of Illinois, Chicago, Illinois 60680

(Received 10 April 1990; accepted for publication 10 April 1990)

Details are provided for aspects of scattering by resonant systems.

PACS number: 43.20.Fn

This letter provides contexts and details for remarks quoted¹ from a recent article² on multiple scattering by finite regular arrays of resonators. Some of the remarks apply for all distances of observation, and the rest hold for the far field.

The article² analyzes scattering of an excess pressure field $\phi = \exp(ikr)$ by arrays of monopoles (of radius a) with centers at $b_i = db_i$ around the origin $r=0$, for arbitrary directions of incidence (\hat{k}) and observation (\hat{r}). Applying earlier results,³ the scattered field \mathcal{U} is given in terms of the appropriate explicit coefficients $D_i(\hat{k})$ for seven different regular arrays (with minimum separation d of neighbors) for all values of $r>0$ external to the obstacles. As kd increases, D_i reduces to the isolated monopole scattering coefficient a_0 . For $r < b_i$, \mathcal{U} consists of standing waves $j_n(kr)$; for $r > b_i$, \mathcal{U} consists of radiating waves $h_n^{(1)}(kr)$. The internal field of an individual obstacle(s) follows from continuity of the total field $\Psi(r) = \phi + \mathcal{U}$ evaluated at $r = b_i + a$.

If $ka \rightarrow 0$ for any value of r , then $\mathcal{U} \rightarrow 0$ and $\Psi \rightarrow \phi$. There are no singularities in \mathcal{U} . Discussions⁴ of "real poles" and

of the "removal of infinities" by the introduction of radiation damping and nonzero radii are vacuous.

Discussions⁵ and plots of Figs. 3–11 for an individual D_i are misleading. Key features are distorted because "peaks narrower than $2ka$... have been truncated at width $2ka$ " to display $|D_i/a_0| \approx M$. Thus, for axial incidence on the doublet (Fig. 3), at coordinate values $(ka, kd) = (0.01389, 0.55)$, the "maximum effective" peak is given as $M \approx 7$ instead of the actual $M \approx 10$; this value is not the largest in the range shown for ka , i.e., $M \approx 24$ at $(0.0140, 0.3553)$. (The range could be extended to pick up an additional order of magnitude and still maintain the restriction that d be sufficiently larger than $2a$ for the simple monopole development to apply^{2,3}.) The discussions⁵ obscure the essential physics. The physical interpretation of $D_i(\hat{k})$ for an array with n different separations $|b_i - b_j| > d$ follows directly from its decomposition² in terms of $n+1$ k -independent oscillator mode coefficients: All characteristics of $D_i(\hat{k})$ are determined by coupling of the $n+1$ collective oscillators that represent the array. For example, the doublet is represented

by coupled mode-0 and mode-1 oscillators, at axial incidence, the peaks correspond to mode-1 resonances detuned slightly by coupling with mode 0.

The discussion of an "obstacle/barrier" half-plane⁵ for Fig. 12 is misleading, the half-plane perpendicular to the triangular array (with edge at its geometrical center) gives rise to a more complicated four-obstacle problem than indicated. At a simplified (and incomplete) level, the incident wave and the three resonators excite cylindrical waves radiated by the edge of the half-plane, and the two flanking resonators excite reflected as well as transmitted waves.

If measurements of \mathcal{Q} are feasible in the near field $r \approx b$, + a of obstacle(s) under conditions for which the fields of all neighbors are negligible, then a coefficient $D_i(k)$ could constitute an observable. However, such measurements are not possible in the far field of the array ($r \gg b$), the context² for the remaining quotations.¹ In the far field, r/b and kr large, \mathcal{Q} factors³ to $h_0^{(1)}(kr)\mathcal{S}(\hat{r}, \hat{k})$ where the scattering amplitude \mathcal{S} is basic to applications. The scattering cross section $S(k)$ obtained from \mathcal{S} determines the net energy outflow from the system. All values of $|\mathcal{S}(\hat{k}, \hat{k})|$ and

$S(\hat{k})$ are less² than twice the maximal values of the single scattering approximations.

The only observable scattering amplitude for the system of resonators in a medium free of other obstacles is $\mathcal{S}(\hat{r}, \hat{k})$. An individual D_i is not observable via a scattering amplitude unless $D_i = D$, the special cases of symmetrically excited planar arrays for which \mathcal{S} is proportional to D . Numerical computations¹ for an individual D_i do not represent physically observable far-field data, and their peaks and locations (ka, kd) are not representative of the values for maximal scattering by the system as a whole. In particular, for polygonal arrays, the maximum values of $|\mathcal{S}|$ and S occur for broadside incidence.²

¹I. Tolstoy, J. Acoust. Soc. Am. 88, 1178-1179 (1990)

²V. Twersky, J. Acoust. Soc. Am. 87, 25 (1990).

³V. Twersky, J. Math. Phys. 3, 88 (1962); J. Opt. Soc. Am. 52, 145 (1962)

⁴I. Tolstoy, J. Acoust. Soc. Am. 80, 282 (1986); 81, 1987 (1987)

⁵I. Tolstoy and A. Tolstoy, J. Acoust. Soc. Am. 83, 2086 (1988).

Multiple scattering by finite regular arrays of resonators

Victor Twersky

Mathematics Department, University of Illinois, Chicago, Illinois 60680

(Received 2 June 1989; accepted for publication 18 August 1989)

Earlier results for multiple scattering by arbitrary configurations of N obstacles are applied to seven regular arrays of two to six monopole resonators (with radius a , maximum scattering cross section σ_c , and normalized resonance frequency $x_c = k_c a$). The arrays involve $m = 1, 2$, or 3 different values of the separations of monopole centers, with d as the smallest. For each array, the corresponding scattering amplitude reduces to a sum of $m + 1$ collective oscillator modes F_n (orthogonal in the same sense as the spherical harmonics). The doublet, triangular, and tetrahedral arrays are specified by two modes, F_0 and F_1 ; the square, pentagonal, and octahedral arrays require a third, F_2 ; and the hexagonal array also requires a fourth, F_3 . The scattering cross section S of each array is less than $2N\sigma_c$, with maximum at a frequency $ka = x$ near x_c for relatively large $kd = y = x/p \gg x$. If $y > 2x$ is small, the F_n reduce to simple multipoles in terms of spherical harmonics and elementary functions of x , p , and x_c . Then S has narrow resonance peaks $S_n = O(\sigma_c)$ at frequencies x_n relatively far from x_c (with $x_0 < x_c$, and the other $x_n > x_c$); the averages over orientation \bar{S}_n add up to $N\sigma_c$ (an average oscillator-strength sum rule). The separations of the resonance frequencies x_n and the fineness of the peaks S_n (nonoverlapping at half-power) provide distinctive signatures for diagnostic and related applications.

PACS numbers: 43.20.Fn

INTRODUCTION

An earlier paper¹ derived representations for the multiple scattered field of an arbitrary configuration of $s = 1$ to N obstacles specified by their isolated scattering amplitudes g_s and locations b_s . The field was expressed in terms of auxiliary amplitudes G_s determined by functional equations involving g_s and radiative functions of the separations $|b_s - b_t| = b_{st} \gg d$ of obstacle centers. Expanding g_s and G_s as series of multipole coefficients times spherical harmonics led to a system of self-consistent algebraic equations relating the two sets of coefficients. Solutions for arbitrary propagation parameter k and directions of incident (\hat{k}) and observation (\hat{r}) were obtained for two obstacles,¹ periodic arrays,² and other distributions.³ Arrays of monopoles were included as illustrations,^{1,2} and symmetrically excited cases (the doublet and regular arrays on a circle normal to \hat{k}) served in a tutorial introduction¹ to multiple scattering. For monopole resonators ($g_s = a_0$), with radius a and normalized resonance frequency ($x_c = k_c a$), the frequency shifts and magnitude changes arising from multiple coupling in periodic arrays² were obtained for small $kd = y > 2ka = 2x$.

Now we consider seven regular arrays of two to six monopole resonators (with maximum scattering cross section σ_c at x_c corresponding to $|a_0| = 1$). Each array has $m < N/2$ different values of b_{st} ; the resulting $G_s = D_s(\hat{k})$ are highly symmetrical, and the multiple scattered amplitude¹ $\mathcal{S}(\hat{r}, \hat{k})$ for the array reduces to a set of $m + 1$ collective modes $F_n(\hat{r}, \hat{k})$. The doublet, triangular, and tetrahedral arrays have two modes; the square, pentagonal, and octahedral arrays have three; and the hexagonal array has four. The oscillator modes F_n are orthogonal in the same sense as the spherical harmonics, and satisfy the same constraints (the

reciprocity and energy theorems) as \mathcal{S} and g . The collective array amplitude \mathcal{S} constitutes the only observable scattering amplitude in a medium free of other obstacles, but an individual F_n may constitute an observable in a subsection of space defined by an appropriate set of infinite image planes. (An individual D_s is not observable unless all $D_t = D_s$, the special cases of symmetrical excitation¹ for which \mathcal{S} is proportional to D_s .)

Complete expressions for $\mathcal{S}(\hat{r}, \hat{k})$ and for the multiple scattered cross section $S(\hat{k})$ of each array are included, but we emphasize only key aspects that help delineate the essential physics. For each array, S is less than $2N\sigma_c$ with maximum at x_n near x_c , all values of S are compatible with elementary physical considerations of interference processes. (Discussions⁴ of extraordinarily large scattering magnitudes and of poles for such arrays are vacuous; discussions⁵ of the plots in Figs. 3-11 for an individual D_s and of the "obstacle/barrier" in Fig. 12 are misleading.) We also show that the average of $|\mathcal{S}(\hat{r}, \hat{k})|$ over all orientations of the array is not larger than the single scattered maximum value (i.e., $|\mathcal{S}| < N$), and consider other physically significant aspects.

If $y = x/p$ is small (with $p = a/d < 1/2$ as the packing factor), the F_n reduce to simple collective multipoles in terms of spherical harmonics times elementary functions of x , p , and x_c . (Neither poles nor other singularities arise for $x \rightarrow 0$.) For y small, S has narrow resonance peaks $S_n = O(\sigma_c)$ at frequencies x_n relatively far from x_c (with $x_0 < x_c$, and the other $x_n > x_c$). The averages over orientation \bar{S}_n add up to $N\sigma_c$, an average oscillator-strength sum rule. The separations of the resonance frequencies x_n and the fineness of the peaks S_n (nonoverlapping at half-power)

provide distinctive signatures for diagnostic and related applications.

In the following, for brevity, we use (1:8) for Eq. (8) of Ref. 1 and Fig. 3.5 for Fig. 5 of Ref. 3, etc. Section I introduces notation and summarizes aspects of scattering theory for one or more obstacles. The mode decomposition of g for a nonspherical obstacle and the small- x behavior of the scattering coefficients a_n of a sphere (for various special cases of its relative compressibility and mass density) are considered to provide prototypes for subsequent sections. Section II gives an overview of common features of the solutions for the regular arrays, and Sec. III deals with explicit illustrations.

Sections II and III retain only the isolated monopole coefficient a_0 , but Appendix A includes the dipole a_1 to obtain monopole-dipole coupling corrections to the resonance frequencies of the doublet at close packing. Section II serves as a summary and reference for general relations that apply for all illustrations; the summary obviates repetition of similar details, and the sequence of topics for arbitrary \hat{k} provides a format to display the essential physics of the specific arrays considered in Sec. III. For each regular array, the simple algebraic system for the N auxiliary coefficients can be solved by elementary algebra to express the $D_i(\hat{k})$ in terms of $m+1$ coefficients B_n , and the array amplitude \mathcal{G} as a sum of corresponding modes $F_n(\hat{r}, \hat{k})$. The F_n in terms of the \hat{k} -independent B_n are basic; Appendix B considers D_1 and D_2 for the doublet, and shows that $D_i(\hat{k})$ need not indicate even the correct order of magnitude of \mathcal{G} .

The mode development emphasizes that each regular array constitutes a single collective obstacle, and clarifies the physical basis for the similarities and differences of the arrays we consider sequentially in Sec. III. The mode decomposition delineates that $\mathcal{G} = \sum F_n$ represents a set of oscillators; the resonance characteristics of a component oscillator are simple, but for arbitrary \hat{k} the oscillators are coupled. To indicate the significance of coupling effects on peaks of $S(\hat{k})$, we include examples of the associated values for component modes, and show that particular peaks correspond to detuning of a single-mode or double-mode resonance, etc. To provide physical interpretations of mode structures, we consider related problems based on image methods (results obtained by superposing array solutions for two or four incident waves): individual modes constitute observables for a single monopole over a free or rigid image plane, or for a monopole centered within a corner reflector of intersecting image planes. The $m+1$ modes of a given array correspond to the fields of $m+1$ sets of in-phase and out-of-phase weighted monopoles, and the F_n are essentially large-scale multipole analogs that generalize the multipoles they reduce to for small $y = x/p$.

The characteristic radiation patterns and sequences of peaks S_n at resonance frequencies x_n provide distinctive scatterers for guidance purposes, for designing composite attenuators and filters, for identifying clusters in propagation through random distributions, etc.

I. SCATTERING FORMALISM

The incident wave ϕ^{inc} is given by

$$\phi = e^{i\mathbf{k} \cdot \mathbf{r}}, \quad \mathbf{k} \cdot \mathbf{r} = kr \cos \theta,$$

$$\hat{r} = \hat{r}(\theta, \varphi) = \hat{z} \cos \theta + \hat{\rho}(\varphi) \sin \theta, \quad (1)$$

$$\hat{\rho}(\varphi) = \hat{x} \cos \varphi + \hat{y} \sin \varphi,$$

where $\hat{k} = \hat{r}(\alpha, \beta)$. When convenient, we use

$$\begin{aligned} \hat{k} &= \hat{x} \sin \alpha \cos \beta + \hat{y} \sin \alpha \sin \beta + \hat{z} \cos \alpha \\ &= \hat{x} \alpha_1 + \hat{y} \alpha_2 + \hat{z} \alpha_3, \end{aligned} \quad (1')$$

with α_n as direction cosines. The phase origin (where $\phi = 1$) is fixed at $r = 0$ for all cases considered.

A. One obstacle

For a single obstacle with center at $r = 0$, the center of its smallest circumscribing sphere (of radius a), we write the external field (the excess pressure) as $\psi = \phi + u$, where u is a radiative function; the internal field is nonsingular. For kr and r/a large, the scattered wave u has the form

$$u \sim h(kr)g(\hat{r}, \hat{k}), \quad g(\hat{r}, \hat{k}) = g(-\hat{k}, -\hat{r}), \quad (2)$$

with g as the dimensionless scattering amplitude and $|g(\hat{r}, \hat{k})|^2/k^2$ as the differential scattering cross section. Restricting discussion to lossless scatterers, the energy transferred via interference of ϕ and u in the forward direction ($\hat{r} = \hat{k}$) is specified by

$$\begin{aligned} -\text{Re } g(\hat{k}, \hat{k}) &= \mathcal{A} |g(\hat{r}, \hat{k})|^2, \\ \mathcal{A} &= \frac{1}{4\pi} \int d\Omega(\hat{r}) = \frac{1}{4\pi} \int_0^{2\pi} d\varphi \int_0^\pi d\theta \sin \theta, \end{aligned} \quad (3)$$

where \mathcal{A} is the mean value over all directions of observation \hat{r} . The total reradiation, the scattering cross section σ , is then $\sigma(\hat{k}) = (4\pi/k^2) \mathcal{A} |g(\hat{r}, \hat{k})|^2 = -(4\pi/k^2) \text{Re } g(\hat{k}, \hat{k})$. (3')

All scattering amplitudes we deal with satisfy the reciprocity theorem $g(\hat{r}, \hat{k}) = g(-\hat{k}, -\hat{r})$ and the forward scattering theorem (3), as well as other relations discussed earlier.

If the obstacle's center is displaced to $\mathbf{r} = \mathbf{b}$, then $u(\mathbf{r})$ is replaced by $u(\mathbf{r} - \mathbf{b})e^{i\mathbf{k} \cdot \mathbf{b}}$ with $u(\mathbf{r} - \mathbf{b}) \sim gh(k|\mathbf{r} - \mathbf{b}|)$ for large $k|\mathbf{r} - \mathbf{b}|$. For $r \gg b$, we have $|\mathbf{r} - \mathbf{b}| \approx r - \hat{r} \cdot \mathbf{b}$, and for $kr \gg 1$,

$$u(\mathbf{r} - \mathbf{b})e^{i\mathbf{k} \cdot \mathbf{b}} \sim h(kr)ge^{i(k\hat{r} \cdot \mathbf{b} - \hat{r} \cdot \mathbf{b})} = h(kr)ge^{i(\delta - \Delta)}, \quad (2')$$

with $\delta = k\hat{r} \cdot \mathbf{b}$ and $\Delta = \hat{r} \cdot \mathbf{b}$ as the incident and radiated phase shifts introduced by the displacement. When convenient we decompose h (the propagator) as

$$h = j + in, \quad j = \sin Y/Y, \quad n = -\cos Y/Y, \quad (4)$$

where $(h, j, n) = (h_0^{(1)}, j_0, n_0)$ are the standard spherical (Hankel, Bessel, and Neumann) functions of order zero.

For the sphere,⁶ in terms of Legendre polynomials $P_n = P_n^0$, Rayleigh obtained

$$\begin{aligned} g(\hat{r}, \hat{k}) &= \sum_{n=0}^{\infty} a_n P_n(\hat{r} \cdot \hat{k}), \\ a_n &= \frac{i(2n+1)b_n}{1 - ib_n} = -\frac{2n+1}{1 + iy_n}. \end{aligned} \quad (5)$$

The scattering coefficients a_n are well known,^{6,7} and general results for $b_n = 1/\gamma_n$ and special cases were discussed before.⁸ For lossless spheres, the γ_n are real,⁸ and

$$- \operatorname{Re} a_n = \frac{2n+1}{1+\gamma_n^2} \frac{|a_n|^2}{2n+1}. \quad (5a)$$

Taking \hat{k} as the polar axis, we have⁷

$$\begin{aligned} \mathcal{M} P_n(\hat{r}; \hat{k}) P_n(\hat{r}; \hat{k}) &= \frac{1}{2} \int_{-1}^1 P_n(\xi) P_n(\xi) d\xi \\ &= \frac{\delta_{nn'}}{2n+1}, \quad P_n(\hat{k}; \hat{k}) = P_n(1) = 1. \end{aligned} \quad (5b)$$

It follows from (5a) that g of (5) satisfies (3). The scattering cross section (3') is

$$\sigma = \frac{4\pi}{k^2} \sum \frac{|a_n|^2}{2n+1} = -\frac{4\pi}{k^2} \sum \operatorname{Re} a_n. \quad (5c)$$

Equivalently, we may write (5) as a set of modes $f_n(\hat{r}, \hat{k}) = a_n P_n(\hat{r}; \hat{k})$,

$$g(\hat{r}, \hat{k}) = \sum f_n(\hat{r}, \hat{k}), \quad f_n(\hat{r}, \hat{k}) = f_n(-\hat{k}, -\hat{r}), \quad (6)$$

satisfying the orthogonality relation for spherical harmonics

$$\mathcal{M} f_n(\hat{r}, \hat{k}) f_{n'}(\hat{r}, \hat{k}) = 0, \quad \text{for } n \neq n'. \quad (6a)$$

Substituting g of (6) into (3) and using (6a) yields

$$\mathcal{M} \sum |f_n(\hat{r}, \hat{k})|^2 = -\operatorname{Re} \sum f_n(\hat{k}, \hat{k}). \quad (6b)$$

Forms (6)–(6b) also follow for more general shaped obstacles by expanding g in terms of $Y_n^\nu(\hat{r}) = P_n^\nu(\cos \theta) e^{i\nu\phi}$ and $Y_n^{\nu*}(\hat{k})$ with P_n^ν as the associated Legendre function; for general harmonics

$$\begin{aligned} \mathcal{M} Y_n^\nu(\hat{r}) [Y_n^{\nu*}(\hat{r})]^* &= \delta_{nn'} \frac{1}{2} \int_{-1}^1 P_n^\nu(\xi) P_n^{\nu*}(\xi) d\xi \\ &= \frac{\delta_{nn'} \delta_{\nu\nu'}}{2n+1} \frac{(n+\nu)!}{(n-\nu)!}, \quad P_n^\nu(1) = \delta_{\nu,0}. \end{aligned} \quad (6c)$$

A special (but not unique) aspect of the completely symmetrical case of the sphere, is that from (5a) and (5b),

$$\mathcal{M} |f_n(\hat{r}, \hat{k})|^2 = -\operatorname{Re} f_n(\hat{k}, \hat{k}), \quad (6d)$$

i.e., each mode f_n satisfies the same relation (3) as g . From (6a) and (6b),

$$\mathcal{M} f_n(\hat{r}, \hat{k}) f_n^*(\hat{r}, \hat{k}) = -\delta_{nn'} \operatorname{Re} f_n(\hat{k}, \hat{k}) \quad (7)$$

with scattering cross section equal to

$$\sigma = -\frac{4\pi}{k^2} \sum \operatorname{Re} f_n(\hat{k}, \hat{k}). \quad (7a)$$

To display less symmetrical cases for which (7) applies, we write the expansion theorem⁷ for the Legendre polynomials as

$$\begin{aligned} P_n(\hat{r}; \hat{k}) &= P_n^0 P_n^0 + 2 \sum_{\nu=1}^n \frac{(n-\nu)!}{(n+\nu)!} P_n^\nu P_n^\nu \cos \nu(\varphi - \beta) \\ &= \sum_{\nu=0}^n Z_n^\nu(\hat{r}, \hat{k}), \end{aligned} \quad (7b)$$

$$P_n^\nu P_n^\nu = P_n^\nu(\cos \theta) P_n^\nu(\cos \alpha), \quad Z_n^\nu = Z_n^{\nu e} + Z_n^{\nu o},$$

where e and o indicate $\cos \nu\varphi \cos \nu\beta$ and $\sin \nu\varphi \sin \nu\beta$. From (6c), we have

$$\mathcal{M} Z_n^\nu(\hat{r}, \hat{k}) Z_n^{\nu'}(\hat{r}, \hat{k}) = \delta_{nn'} \delta_{\nu\nu'} (2n+1)^{-1} Z_n^{\nu\nu}(\hat{k}, \hat{k}), \quad (7c)$$

where $\nu = e$ or o , so that the result also holds for $Z_n^{\nu e}$, and for any set $Z_n^\nu(\hat{r}, \hat{k})$ of one or more of the $Z_n^{\nu e}$ components of $P_n(\hat{r}; \hat{k})$. Thus (7) applies for any term of

$$\sum A_n Z_n^\nu(\hat{r}, \hat{k}), \quad A_n = -\frac{2n+1}{1+i\Gamma_n}, \quad (7d)$$

where Γ_n is real, and (7a) applies for the sum. This form provides a prototype for subsequent decompositions of multiple scattering amplitudes for regular arrays of monopoles in terms of more general functions subject to the same constraint (7).

For a sphere with relative compressibility C and relative mass density B^{-1} , exclusive of either $B = 1$ or $C = 1$, the correct leading terms⁶ for small $ka = x$ follow from

$$\begin{aligned} \gamma_0 &= \frac{3-x^2C}{x^3(C-1)}, \quad \gamma_1 = -\frac{3(B+2)}{x^3(B-1)}, \\ \gamma_n &= O(x^{-1-2n}). \end{aligned} \quad (8)$$

For the excluded cases, if only $B = 1$, then, in general, $\gamma_n = O(x^{-1-2n})$, and $\gamma_0 = O(x^{-3})$ dominates; if only $C = 1$, then, in general, $\gamma_0 = O(x^{-3})$, and $\gamma_1 = O(x^{-2})$ dominates. [Analogous of the first with $\Gamma_n = O(x^{-1-2n})$ arise subsequently.] If both $B \rightarrow 1$ and $C \rightarrow 1$, or if $x \rightarrow 0$ and consequently $x \rightarrow 0$, then $\gamma_n \rightarrow \infty$, $a_n \rightarrow 0$, and g vanishes for the trivial case of no obstacle: there are no singularities in the problem.

The rigid sphere corresponds to $B = C = 0$ in (8); then $\gamma_0 = -3x^{-3}$, $\gamma_1 = 6x^{-2}$, and all γ_n except γ_0 are positive. The free surface (pressure release) case corresponds to infinite C and B in (8), with $\gamma_0 = -x^{-1}$ and $\gamma_1 = -3x^{-2}$, so that γ_0 dominates; all γ_n are negative. [The difference in sign of $O(x^{-1-2n})$ terms of Γ_n that arise subsequently facilitates interpretation of multipoles as either rigid or free.]

If C and B are finite but very large, then

$$\gamma_0 = \frac{3-x^2C}{x^3C} = \frac{x^2-x^2}{x^3} = \gamma, \quad \gamma_1 = -\frac{3}{x^3}, \quad (8a)$$

with resonance ($\gamma = 0$) at $x = x_c = (3/C)^{1/2}$, where $a_0 = -1$. For $x/x_c = X$ increasing from zero, the normalized function $\gamma x_c = (1-X^2)/X^3$ decreases initially as X^{-3} , vanishes at $X = 1$, has its minimum value $-2/3\sqrt{3}$ at $X = \sqrt{3}$, and then approaches zero as $-X^{-1}$. The benchmark values

$$\gamma = x_c^2/x^3, \quad 0, \quad -1/x \quad (8b)$$

(with corresponding $|a_0| = x^3/x_c^2, 1, x$) highlight the behavior at very low frequency, the resonance frequency, and the higher frequency pressure release range. From $|a_1| \approx x^2$ we have $|a_1/a_0| \approx x_c^2/x_c^2 x^2$; the smallness of x^2 provides a criterion for neglecting the dipole as well as the higher-order terms of the monopole. (We include a_1 only in Appendix A to illustrate the simplest monopole-dipole coupling effects in multiple scattering.)

The primary development is based on

$$a_0 = -\frac{1}{1+i\gamma}, \quad \gamma = \frac{x_c^2-x^2}{x^3}, \quad x_c = \left(\frac{3}{C}\right)^{1/2}. \quad (9)$$

The corresponding $|a_0|^2 = -\text{Re } a_0 = (1 + \gamma^2)^{-1}$ is a maximum at resonance:

$$x = x_c, \quad a_0 = a_{0c} = -1, \quad |a_{0c}|^2 = 1. \quad (9a)$$

The half-power values ($|a_0|^2 = 1/2$) are at $x_{\pm} = x_c \pm x_c^2/2$, and the half-power peak width $w_c = x_{+} - x_{-} = x_c^2$ is narrow. In the pressure release range, the scattering cross section $\sigma = 4\pi|a_0|^2/k^2$ approximates $4\pi a^2 = \sigma^0$, the surface area of the sphere (twice the asymptotic high-frequency value of σ based on the complete g , and four times the geometrical cross section); the scattering cross section at resonance

$$\sigma_c = 4\pi/k_c^2 = 4\pi a^2/x_c^2 = \sigma^0/x_c^2 = \sigma^0 C/3 \quad (9b)$$

is orders of magnitude larger.

For numerical purposes we use $C = 1.589 \times 10^4$ and $B^{-1} = 1.3 \times 10^{-3}$ (appropriate for an air bubble in the sea)^{9,10} to obtain

$$x_c = 0.013740, \quad \sigma_c \approx 5300\sigma^0 = 2.12 \times 10^4 \pi a^2. \quad (9c)$$

Form a_0 of (9) suffices for $x < 0.1$, but with increasing x additional coefficients a_n and more complete forms of a_0 are required. The values in (9c) correspond to the leading resonance, the largest peak of σ and the lowest resonance frequency (the first for the monopole); the next peak is $\sigma \approx 14.2\sigma^0$ at $x \approx 0.46$ (the first resonance of the dipole). For x increasing, a double infinite set of values x_{nm} lead to $\gamma_n = 0$ and $a_n = -(2n+1)$ with associated radiation $\sigma^0(2n+1)/(x_{nm})^2$ corresponding to the m th resonance of the oscillator represented by a_n . The significance of subsequent peaks depends on the background radiation of the other modes; detailed numerical results are available.¹⁰ Thus, in general, the form $a_n(\gamma_n)$ represents an oscillator and g represents a sum of coupled oscillators.

B. Many obstacles

A bounded array of $s = 1$ to N obstacles is specified by the isolated scattering amplitudes g_s , and the locations b_s of the centers with respect to $r = 0$, such that N and $b_s < b$ are finite. For $r \gg b$, the scattered part of the solution external to all obstacles ($\Psi = \phi + \mathcal{U}$) satisfies¹

$$\mathcal{U}(r; \hat{k}) \sim h(kr) \mathcal{S}(\hat{r}, \hat{k}), \quad \mathcal{S}(\hat{r}, \hat{k}) = \mathcal{S}(-\hat{k}, -\hat{r}), \quad (10)$$

with \mathcal{S} as the scattering amplitude of the array. For lossless obstacles the scattering cross section $S(\hat{k})$ of the array fulfills

$$S(\hat{k}) = (4\pi/k^2) \cdot \mathcal{U}(\hat{r}, \hat{k}) \mathcal{U}(\hat{r}, \hat{k})^* = -(4\pi/k^2) \text{Re } \mathcal{S}(\hat{k}, \hat{k}). \quad (10')$$

These are the same forms as (2) and (3'): the array constitutes a single collective obstacle with scattering cross section $S(\hat{k})$.

As discussed before in detail,¹ we can decompose \mathcal{U} as

$$\mathcal{U}(r; \hat{k}) = \sum_{s=1}^N U_s(r - b_s) e^{i\delta_s}, \quad \delta_s = k \cdot b_s = k \hat{k} \cdot b_s = \delta_s(\hat{k}) \quad (11)$$

where U_s , a radiative field everywhere outside of obstacle s , depends on the locations and properties of all obstacles in the array. For r/b_s and kr large,

$$U_s(r - b_s) \sim h(k|r - b_s|) G_s(\hat{r}; \hat{k})$$

$$\sim h(kr) e^{-i\delta_s} G_s(\hat{r}; \hat{k}),$$

$$\Delta_s = k \hat{k} \cdot b_s = \delta_s(\hat{k}), \quad (12)$$

where G_s (the multiple scattering amplitude of obstacle s within the array) reduces to g_s with increasing separation $k|b_s - b_t| = kb_{st}$ of its neighbors. In terms of G_s ,

$$\mathcal{S}(\hat{r}, \hat{k}) = \sum_{s=1}^N G_s(\hat{r}; \hat{k}) e^{i(\delta_s - \Delta_s)}, \quad \mathcal{S}(\hat{k}, \hat{k}) = \sum_s G_s(\hat{k}; \hat{k}). \quad (13)$$

Various functional representations [integral equations (1:34), algebraic systems (1:42), etc.] for the auxiliary amplitudes G_s in terms of g_s and $b_s - b_t = b_{st} = b_{st} b_{st}$ were derived and applied¹⁻³ to construct \mathcal{S} or \mathcal{U} for determining the observable scattering characteristics of bounded and unbounded arrays.

The simplest problems involve only monopoles $g_s = a_s^0$ and $G_s = D_s(\hat{k})$. Then the self-consistent algebraic system (1:44) reduces to

$$D_s = a_s^0 \left(1 + \sum_{t \neq s} D_t h(y_{st}) e^{-i\delta_{st}} \right), \quad (14)$$

$$y_{st} = kb_{st} \gg kd = y, \quad \delta_{st} = \delta_s - \delta_t = k \cdot b_{st} = y_{st} \hat{b}_{st}$$

as follows directly from elementary physical considerations.¹ For increasing y , all propagators $h(y_{st})$ tend to zero, $D_s \sim a_s^0$, and \mathcal{S} reduces to the single scattering approximation.

Form (14) is based on the isolated monopole wave

$$u_s \phi(b_s) = u_s e^{i\delta_s} = a_s^0 h(k|r - b_s|) e^{i\delta_s} \quad (14')$$

and the corresponding auxiliary wave

$$U_s(r - b_s) e^{i\delta_s} = D_s h(k|r - b_s|) e^{i\delta_s}, \quad D_s = D_s(\hat{k}). \quad (15)$$

We expect (14) to apply for b_{st} large enough compared to the sum of the respective radii of scatterers s and t , but analytical criteria for validity require more complete forms of u_s and U_s that include higher-order multipoles. In particular, the closed form solution (1:72)–(1:75) for the doublet of two different spheres, each characterized in isolation by a different monopole plus dipole, provides criteria for the simpler cases of two different monopoles (1:63) as well as for two different dipoles (1:69). See discussion after (1:75). In Appendix A, we apply (1:75) to consider the effects of monopole-dipole coupling on the resonance frequencies of the doublet of identical monopoles.

II. REGULAR ARRAYS

The simplest finite arrays correspond to obstacle centers at the vertices $b_s = \hat{b}b$, of regular polygons or polyhedra on a sphere of radius $r = b$, for these $\Sigma b_s = 0$ with constant $\hat{b} \cdot \hat{b}_t$ between nearest neighbors. Each array has $m < N/2$ different values of $b_{st} > d$ known explicitly in terms of the smallest (an edge of one of the regular figures). A regular array of identical monopoles is particularly simple. The D_s obtained from

$$D_i(\hat{k}) = a_0 \left(1 + \sum_{j \neq i} D_j(\hat{k}) h(y_{ij}) e^{-i\Delta_j} \right), \quad (16)$$

are highly symmetrical, and the array amplitude

$$\mathcal{S}(\hat{r}, \hat{k}) = \sum_{i=1}^N D_i(\hat{k}) e^{i(\hat{r}, \hat{k} - \Delta_i)} \quad (17)$$

reduces to a set of $m+1$ collective orthogonal modes F_n that satisfy (6) and (7). Thus

$$\mathcal{S}(\hat{r}, \hat{k}) = \sum_{n=0}^m F_n(\hat{r}, \hat{k}), \quad F_n(\hat{r}, \hat{k}) = F_n(-\hat{k}, -\hat{r}), \quad (18)$$

$$\mathcal{M} F_n(\hat{r}, \hat{k}) F_n^*(\hat{r}, \hat{k}) = -\delta_{nn} \text{Re } F_n(\hat{k}, \hat{k}), \quad (18')$$

where $m+1$ is the number of distinct eigenvalues of the matrix for the system (16).

We analyze seven arrays for $N=2$ to 6, and arbitrary \hat{k} and \hat{r} : the doublet, triangular, and tetrahedral arrays ($m=1$) are specified completely by two modes F_0 and F_1 ; the square, pentagonal, and octahedral arrays ($m=2$) require a third F_2 ; and the hexagonal array ($m=3$) also requires a fourth F_3 . We obtain $\mathcal{S}(\hat{r}, \hat{k})$ as well as the array scattering cross section

$$S(\hat{k}) = R 4\pi/k^2 = R \sigma_c(x_c/x)^2, \quad (19)$$

$$R = -\text{Re } \mathcal{S}(\hat{k}, \hat{k}) = -\sum_n \text{Re } F_n(\hat{k}, \hat{k}) = \sum_n R_n.$$

The final form of S is normalized with respect to isolated monopole resonance values to facilitate comparisons. For y increasing, R tends to $N|a_0|^2$ and S tends to $N\sigma$. The maximal value of S (and the associated values of $y = kd$ and $x = ka$), and the maximal shifts of x from x_c that yield $S = O(\sigma_c)$, are included for all cases.

The collective array amplitude \mathcal{S} constitutes the only observable scattering amplitude in a medium free of other obstacles. An individual F_n may constitute an observable in a subsection of space defined by an appropriate set of image planes through $r=0$; several examples are included. An individual D_i is not observable unless $D_i = D$, the special cases of symmetrically excited planar arrays³ for which \mathcal{S} is proportional to D . (Numerical computations³ for an individual D_i do not represent physically observable data.) The D_i contain additional terms that cancel in the sum \mathcal{S} ; a simple example is given in Appendix B.

In order to introduce notation and terminology, we start with normal incidence on planar arrays,³ and then sketch the common features of the general mode development for arbitrary \hat{k} for all arrays analyzed in Sec. III.

A. Symmetrical excitation

The closed form solution of (16) for symmetrical distributions on a circle normal to the direction of incidence (say $\hat{k} = \hat{z}$) was given before.³ For such cases ($\hat{z} \cdot \hat{b}_i = 0$), the net excitation of each obstacle is identical, and consequently, by inspection,

$$D_i = D = \frac{a_0}{1 - a_0 \mathcal{H}} \equiv B, \quad \mathcal{H} = \sum' h(y_{ij}) = \mathcal{H}(y) \quad (20)$$

as discussed after (3:14). The sum is independent of one of the two interchangeable dummies, and we may take, e.g., $s=1$ and sum over $t=2$ to N , or the converse, etc. The y_{st} for regular polygons are known constants times y so that \mathcal{H} is a known function of y . For y increasing, \mathcal{H} tends to zero and B reduces to a_0 .

The corresponding array amplitude equals

$$\mathcal{S}(\hat{r}, \hat{z}) = B \sum_{i=1}^N e^{-i\Delta_i} = B \sum e^{-i\Delta_i \hat{b}_i}, \quad \mathcal{S}(\hat{z}, \hat{z}) = NB. \quad (20')$$

Since $-\Delta_i = \delta_i(-\hat{r})$, it follows that $\mathcal{S}(\hat{r}, \hat{z}) = \mathcal{S}(-\hat{z}, -\hat{r})$, as may also be obtained by direct summation of $D_i(-\hat{r}) = D_i[e^{-i\Delta_i}]$ of (16).

Decomposing the weighted sum of propagators into real and imaginary parts, $\mathcal{H}(y) = \mathcal{J} + i\mathcal{I}$, we generalize the isolated scatterer form $a_0 = -[1 + i\gamma(x)]^{-1}$ by

$$B(\mathcal{H}) = -[1 + i\gamma + \mathcal{H}]^{-1} \\ = -[1 + \mathcal{J} + i(\gamma + \mathcal{I})]^{-1} \\ = -[W(1 + i\Gamma)]^{-1}, \quad (21)$$

$$W = 1 + \mathcal{J}, \quad \Gamma = (\gamma + \mathcal{I})/W$$

$$\text{Re } B = -[W(1 + \Gamma^2)]^{-1} = -W|B|^2, \quad (21a)$$

$$W = 1 + \sum' j(y_{ij}), \quad (21b)$$

where $W = W(y)$ and $\Gamma = \Gamma(x, y)$.

The corresponding scattering cross section is proportional to

$$\mathcal{M}|\mathcal{S}(\hat{r}, \hat{z})|^2 = |B|^2 \mathcal{M} \left| \sum e^{-i\Delta_i} \right|^2 \\ = |B|^2 \left(N + \sum_{i,j} \mathcal{M} e^{i\Delta_{ij}} \right), \quad (21b)$$

where $\Delta_{ij} = y_{ij} \hat{r} \cdot \hat{b}_{ij}$. To evaluate $\mathcal{M} e^{i\Delta_{ij}}$, we take \hat{b}_{ij} as polar axis and obtain

$$\mathcal{M} \exp(iy_{ij} \hat{r} \cdot \hat{b}_{ij}) = \frac{1}{2} \int_{-1}^1 \cos(y_{ij} \xi) d\xi \\ = \frac{\sin y_{ij}}{y_{ij}} = j(y_{ij}) \quad (22)$$

(which also suffices for all averages in subsequent sections). Using (22) in (21b), and then (21a) and (20a),

$$\mathcal{M}|\mathcal{S}(\hat{r}, \hat{z})|^2 = |B|^2 NW = -N \text{Re } B \\ = -\text{Re } \mathcal{S}(\hat{z}, \hat{z}) \equiv R(x, y) \quad (23)$$

shows that $\mathcal{S}(\hat{r}, \hat{z})$ satisfies the required forward scattering theorem (3).

We have

$$R(x, y) = N[(1 + \mathcal{J})(1 + \Gamma^2)]^{-1} \\ < N(1 + \mathcal{J})^{-1} \equiv R(y), \quad (23a)$$

as well as $|\mathcal{S}(\hat{z}, \hat{z})| < R(y)$. We regard $x = ka$ (the normal-

ized frequency) as the variable, and $x/y = a/d = p$ (the packing factor, $p < 1/2$) as the parameter; however, when convenient we take both x and y as variables. All resonances correspond to $\Gamma = 0$, $-\mathcal{G}(\hat{z}, \hat{z}) = R(y)$,

$$R(y) = \frac{N}{1 + \mathcal{F}(y)}, \quad x^2 = \frac{x_c^2}{1 - x \mathcal{F}(y)},$$

$$\mathcal{N}(y) = \sum n(y_n), \quad y = \frac{x}{p}, \quad (23b)$$

where $R(x/p)$ vs x is the envelope of the magnitudes for a given value of p . The peak magnitude $R = R_\lambda$ is determined by the value $y = y_\lambda$ that minimizes $1 + \mathcal{F}(y)$; the resulting value $\mathcal{N}(y_\lambda)$ then specifies the associated frequency $x = x_\lambda$. To $N = 24$ we find $y_\lambda > 3.4$, $\mathcal{F}(y_\lambda) > -0.5$ (which also holds asymptotically for all N), and $x \approx x_c$ to within 0.2%; consequently $-\text{Re } \mathcal{G} = |\mathcal{G}| < 2N$, and $S < 2N\sigma_c$. The maximal shifts in resonance frequency from x_c that yield $S = O(\sigma_c)$ arise for small $y = x/p$. We reserve further discussion of symmetrically excited periodic ring distributions.

B. Arbitrary direction of incidence

From (16) for arbitrary \hat{k} ,

$$D_s(\hat{k})e^{i\delta_s} = \sum_{n=0}^m \frac{B_n I_n^s(\delta)}{N}, \quad (24)$$

where $I_n^s(\delta)$ is a weighted set of exponentials $\exp(i\delta_s)$. The B_n have the form in (21),

$$B_n = B_n(\mathcal{H}_n) = a_0/(1 - a_0 \mathcal{H}_n) \\ = -[W_n(1 + i\Gamma_n)]^{-1}, \\ W_n = 1 + \mathcal{F}_n, \quad \Gamma_n = (\gamma + \mathcal{N}_n)/W_n,$$

$$\text{Re } B_n = -W_n/B_n, \quad (24a)$$

with $\mathcal{H}_n = \mathcal{F}_n + i\mathcal{N}_n$ as a weighted set of propagators $h(y_n)$; in particular, $\mathcal{H}_0 = \sum h(y_n)$ generalizes \mathcal{H} of (20) to include polyhedra. From (16), $\sum_s D_s e^{i\delta_s} = B_0 \sum_s e^{i\delta_s} = B_0 I_0^s$,

$$I_0^s = \sum_{n=0}^N e^{i\delta_n} I_n^s(\delta), \quad \sum_{n=1}^N I_n^s = 0, \text{ for } n \neq 0; \\ \sum_{n=0}^m I_n^s(\delta) = N e^{i\delta_s}. \quad (24b)$$

The I_0^s are independent of s , and the other I_n^s consist of differences of exponentials whose sum over s vanishes; the last equality follows from (24) because D_s and $B_n \rightarrow a_0$ as $y \rightarrow \infty$. Substituting (24) into (17) yields (18) with

$$F_n(\hat{r}, \hat{k}) = B_n L_n(\hat{r}, \hat{k})/N, \\ L_n(\hat{r}, \hat{k}) = L_n(-\hat{k}, -\hat{r}) \\ = \sum_s I_n^s(\delta) e^{-i\delta_s} = \sum_s I_n^s(-\Delta) e^{i\delta_s}. \quad (25)$$

In the forward direction, $L_n(\hat{k}, \hat{k}) = L_n(-\hat{k}, -\hat{k}) = L_n^*(\hat{k}, \hat{k})$ is real. Since D_s and $B_n \rightarrow a_0$ for $y \rightarrow \infty$, the two forms (17) and (18) of \mathcal{G} yield

$$\sum_{n=0}^m \frac{L_n(\hat{r}, \hat{k})}{N} = \sum_{n=1}^N e^{i(\delta_n - \Delta_n)} \sum_n \frac{L_n(\hat{k}, \hat{k})}{N} = N. \quad (25a)$$

We write $L_0(\hat{r}, \hat{k})$ as

$$I_{(N)}(\delta) I_{(N)}(-\Delta) = I_{(N)} I'_{(N)} = II', \quad (25b)$$

and express the other L_n in terms of

$$e^{i\delta_n} - e^{i\delta'_n} = T_n(\delta) = T_n, \quad T_n(-\Delta) = T'_n, \quad (25c)$$

as weighted sets of the product form $T_n T'_n$ (but alternative groupings may be used). Applying (22), it can be shown for all cases considered subsequently that

$$\mathcal{H} L_n(\hat{r}, \hat{k}) L_n^*(\hat{r}, \hat{k}) = \delta_{nn} N W_n L_n(\hat{r}, \hat{k}). \quad (25d)$$

Consequently, the $F_n(\hat{r}, \hat{k})$ are orthogonal in the same sense as the spherical harmonics, and the modes satisfy (18'). Each coefficient B_n represents an oscillator essentially as discussed for (21), and \mathcal{G} represents a set of oscillators (coupled in general). We could expand all L 's as infinite subsets of spherical harmonics, but the expansions in terms of exponentials are simpler and emphasize the essential symmetries of the arrays.

In the forward direction, $I' = I^*$ and $T' = T^*$, and

$$F_n(\hat{k}, \hat{k}) = \frac{B_n L_n(\hat{k}, \hat{k})}{N} = B_n V_n(\hat{k}) = \frac{-V_n}{W_n(1 + i\Gamma_n)}, \\ V_n(\hat{k}) > 0, \quad \sum_{n=0}^m V_n(\hat{k}) = N, \quad (26)$$

where the V_n involve weighted sums of appropriate subsets (C) of $\cos \delta_{in} \approx \cos(\hat{y}_n \hat{k} \cdot \hat{b}_{in})$. The forward scattered array amplitude reduces to

$$\mathcal{G}(\hat{k}, \hat{k}) = \sum B_n V_n = - \sum \frac{V_n}{W_n(1 + i\Gamma_n)}, \\ -\text{Re } \mathcal{G}(\hat{k}, \hat{k}) = R = \sum R_n,$$

$$R_n = -\text{Re } F_n(\hat{k}, \hat{k}) = V_n(\hat{k})/W_n(1 + \Gamma_n^2), \\ R_n < V_n/W_n, \quad (26a)$$

with $W_n = 1 + \mathcal{F}_n$ and $\Gamma_n = (\gamma + \mathcal{N}_n)/W_n$ as in (24a). The scattering cross section S of the array follows directly from (19) in terms of R . The sum $\sum V_n/W_n$ provides an unrealizable upper bound for R and for $|\mathcal{G}(\hat{k}, \hat{k})|$. For all cases analyzed numerically, R is less than $2N$, and S is less than $2N\sigma_c$; all values are compatible with elementary physical considerations of interference processes.

For each array, we also obtain the average of $\mathcal{G}(\hat{k}, \hat{k})$ and of $S(\hat{k})$ over all orientations, or equivalently over all \hat{k} . Using (22) with \hat{r} replaced by \hat{k} converts the integrals of $\cos \delta_{in}$ to $j(y_{in})$, and the average of $V_n(\hat{k})$ is given by

$$\bar{V}_n = \frac{1}{4\pi} \int d\Omega(\hat{k}) V_n(\hat{k}) = v_n(1 + \mathcal{F}_n) = v_n W_n, \\ \sum_{n=0}^m v_n = N, \quad (26b)$$

where v_n is an appropriate integer. The averages of $\mathcal{G}(\hat{k}, \hat{k})$ and $R(\hat{k})$ satisfy

$$\bar{\mathcal{G}} = \sum \bar{F}_n = - \sum \frac{v_n}{(1 + i\Gamma_n)}, \\ \bar{R} = \sum \bar{R}_n = \sum \frac{v_n}{(1 + \Gamma_n^2)}, \quad \bar{R}_n < v_n, \quad \bar{R} < N. \quad (26c)$$

In general (except for $m=1$), $\bar{R}=N$ is realizable only for $y \sim \infty$ and $\gamma=0$, with y increasing, $\Gamma_n \sim \gamma$ and $\bar{R} \sim N/(1+\gamma^2)$, the single scattered value.

For small $y = x/p > 2x$, the L_n and W_n are $O(y^{2n})$, and $L_n/NW_n \rightarrow (2n+1)Z_n$ as sets of the spherical harmonics Z_n associated with $P_n(\hat{r}, \hat{k})$ as in (7b)ff. Then the F_n reduce to collective multipoles

$$F_n(\hat{r}, \hat{k}) = A_n Z_n(\hat{r}, \hat{k}), \\ A_n = -(2n+1)/(1+i\Gamma_n), \quad (27)$$

$$\mathcal{G} = \sum_{n=0}^{\infty} A_n Z_n,$$

with Γ_n as a simple function of x , p , and x_c . Thus, since $\mathcal{V}_n = c_n/y + O(y)$, we have

$$\Gamma_n = (\gamma + c_n/y) K_n y^{-2n} \\ = [x_c^2 - x^2(1 - pc_n)] K_n p^{2n} x^{-2n-3} \quad (27a)$$

such that c_0 is negative, and all other numerical factors c_n and K_n (with $K_0=N$) are positive; the corrections are $O(x^{-2n+1})$. At a resonance, $\Gamma_n = 0$, $\mathcal{G} \approx F_n$,

$$x_n^2 = x_c^2/(1 - pc_n), \quad F_n(\hat{r}, \hat{k}) = -(2n+1)Z_n(\hat{r}, \hat{k}), \\ S_n(\hat{k}) = (2n+1)Z_n(\hat{k}, \hat{k})(1 - pc_n)\sigma_c, \quad (27b)$$

where $x_0 = x_c/(1 + p|c_0|)^{1/2} < x_c$, but all other $x_n > x_c$. Except near special directions where a particular Z_n can vanish, $S_n = O(\sigma_c)$. The half-power peak width

$$w_n = x_n^{2n+2}/K_n p^{2n}(1 - pc_n) \\ = x_c^{2n+2}/K_n p^{2n}(1 - pc_n)^{n+1} \\ = O(w_0^{n+1}) \quad (27c)$$

indicates that w_0 is comparable to the isolated monopole value $w_c = x_c^2$ but that all other w_n are much smaller; the different widths do not overlap. The frequencies corresponding to the locations and separations of the fine peaks provide distinctive signatures for diagnostic and related purposes.

From (7b) and (6c) we have $\bar{Z}_n^{\alpha} = \bar{Z}_n^{\alpha}$, $\bar{Z}_n^{\alpha} = 1/(2n+1)$; the number of such terms in a particular Z_n of (27) is v_n so that $\bar{Z}_n = v_n/(2n+1)$, and the average of $S_n(\hat{k})$ over orientation reduces to $\bar{S}_n = v_n(1 - pc_n)\sigma_c$ such that $\sum v_n c_n = 0$. [The same \bar{S}_n follows from \bar{R}_n of (26c) for $\Gamma_n = 0$; we obtain $\bar{S}_n = v_n \sigma_c (x_c/x_n)^2$ and then use $(x_c/x_n)^2 = 1 - pc_n$.] Thus the averages over orientation satisfy

$$\sum_{n=0}^{\infty} \bar{S}_n = \sum v_n (1 - pc_n) \sigma_c = N \sigma_c, \\ \sum v_n \left(\frac{x_c}{x_n} \right)^2 = N, \quad (28)$$

an average oscillator-strength sum rule for magnitudes observed at the interrelated resonance frequencies (x_n); the resonance wavelengths ($\lambda_n = 2\pi/k_n$) satisfy $\sum v_n \lambda_n^2 = N \lambda_c^2$. The integers v_n are the multiplicities of the eigenvalues $(1 - a_0 \mathcal{H}_n)$ of the matrix for the system (16); the trace satisfies $\sum v_n (1 - a_0 \mathcal{H}_n) = N$, so that

$$\sum_{n=0}^{\infty} v_n \mathcal{H}_n(y) = 0. \quad (28a)$$

The sum rule is based on $\sum v_n c_n = 0$ which corresponds to the limit of $\sum v_n \mathcal{V}_n(y)$ for $y \rightarrow 0$.

The essentials of the nonresonant behavior of the F_n are covered by the following. Corresponding to the sequence (8b) of benchmark values of γ for increasing x ,

$$\Gamma_n = O(x_c^2 x^{-3-2n}), (2n-1)O(x_c^{-1-2n}), -O(x^{-1-2n}), \quad (28b)$$

where the exponents and signs are discussed after (8). If $x \rightarrow 0$, then $\mathcal{G} \rightarrow 0$; there are no poles or any other singularities in any such multiple scattering problems that have been properly analyzed. For all such cases, the collective monopole $A_0 = -(1 + i\Gamma_0)^{-1}$ dominates, and $\mathcal{G} \approx A_0$. We have

$$N\Gamma_0 = x_c^2/x^3, \quad p|c_0|/x_c, \quad -(1 + p|c_0|)/x. \quad (28c)$$

If $x \approx 0$, then $|\mathcal{G}| \approx N x_c^2/x^3$ approximates the single scattered value. If $\gamma = 0$, then Γ_0 corresponds to a collective free monopole, and the remaining Γ_n to collective rigid multipoles. For the free surface isolated monopole range ($\gamma = -1/x$), all collective multipoles are free.

On the other hand, if one of the $m+1$ modes is in resonance, $\Gamma_n(x_n) = 0$, then

$$\Gamma_n(x_n) = \pm O(x_n^{-1-2n}), \quad \text{for } n' \geq n, \quad (28d)$$

where the $\Gamma_n(x_n)$ correspond to free collective multipoles for $n' < n$ and to rigid for $n' > n$. For $\Gamma_0(x_0) = 0$, all the remaining modes are negligible. For $\Gamma_n(x_n) = 0$, because $F_n(\hat{r}, \hat{k})$ and $S_n(\hat{k})$ may vanish for special directions, we note that the background monopole is determined by

$$\Gamma_0(x_n) = -p(|c_0| + c_n)/N x_n. \quad (28e)$$

C. The field

From (11) and (15), the total field ($\phi + \mathcal{W}$) external to all monopoles is specified by

$$\mathcal{W}(\mathbf{r}; \hat{\mathbf{k}}) = \sum_{n=1}^N h(k|\mathbf{r} - \mathbf{b}_n|) D_n(\hat{\mathbf{k}}) e^{i\delta_n}, \quad (11a)$$

with $D_n e^{i\delta_n}$ as in (24). At the geometrical center ($r=0$) of a regular array,

$$\mathcal{W}(0, \hat{\mathbf{k}}) = h(kb) \sum_{n=1}^N D_n e^{i\delta_n} = h(kb) B_0 I_{(N)}(\delta), \quad (11b)$$

with B_0 and $I_{(N)}$ as discussed for (24a) and (24b). For polygonal arrays normal to $\hat{\mathbf{z}}$, the field along the center line ($r=z$) is given by

$$\mathcal{W}(z, \hat{\mathbf{k}}) = h(k\sqrt{z^2 + b^2}) B_0 I_{(N)}(\delta). \quad (11c)$$

For the doublet with axis along $\hat{\mathbf{z}}$, we use $r^2 = z^2 + \rho^2$ to write the field in the midplane ($r=\rho$) as

$$\mathcal{W}(\rho, \hat{\mathbf{k}}) = h(k\sqrt{\rho^2 + b^2}) 2B_0 \cos \delta_1, \quad \delta_1 = kb\hat{\mathbf{k}} \cdot \hat{\mathbf{z}}. \quad (11d)$$

More generally for arbitrary r external to all monopoles we use (11a) in terms of (24) and expand the propagator $h = h_0^{(1)}$ as the series

$$h(k|\mathbf{r}-\mathbf{b}_i|)$$

$$= \sum_{m=0}^{\infty} (2m+1) j_m(kr_<) h_m^{(1)}(kr_>) P_m(\hat{\mathbf{r}} \cdot \hat{\mathbf{b}}_i)$$

with $r_< = r$ and $r_> = b$ for $r < b$ (standing waves in kr) and conversely for $r > b$ (radiating waves in kr). Grouping the various s factors, we isolate the B_n and the subsets of spherical harmonics appropriate for a particular array. Analogous results for regular arrays of cylindrical monopoles parallel to z follow from the forms for regular planar arrays [e.g., from (11c) with $B_0 = B$ as in (20)] on replacing spherical functions by corresponding cylindrical functions.

III. ILLUSTRATIONS

The seven regular arrays for $N = 2$ to 6 considered in the following are grouped for $m = 1, 2$, and 3 under A , B , and C . For each array the \mathbf{b}_i are listed in Cartesian coordinates, and D_i is exhibited directly in terms of $B_n(\mathcal{H}_n)$ and I_n , and T_n ; in general, the other D_i follow by cyclical interchange. We then list the modes $F_n(\hat{\mathbf{r}}, \hat{\mathbf{k}})$ and proceed as for (26)ff. Several examples of image methods are included to facilitate interpretation of the mode structure that is key to the development. We start with a special case of the earlier¹ result for two different monopoles, and give $B_0(\mathcal{H}_0)$ and $B_1(\mathcal{H}_1)$ explicitly to provide prototypes.

A. Two collective modes

There are three regular figures for which each vertex ($\mathbf{b}_i = b\hat{\mathbf{b}}_i$) is at the same distance $d = b_i$ from the others: the doublet ($N = 2$), equilateral triangle ($N = 3$), and tetrahedron ($N = 4$); for these, $\hat{\mathbf{b}}_i \cdot \hat{\mathbf{b}}_j = -1, -1/2, -1/3$, and $d/b = 2, \sqrt{3}, \sqrt{8/3}$, respectively. Each corresponding array of monopoles involves only one propagator $h(kd) = h(y) = h = j + in$, and the multiple scattered array amplitude of each consists of only two collective orthogonal modes

$$\mathcal{S}(\hat{\mathbf{r}}, \hat{\mathbf{k}}) = F_0(\hat{\mathbf{r}}, \hat{\mathbf{k}}) + F_1(\hat{\mathbf{r}}, \hat{\mathbf{k}}). \quad (29)$$

1. The doublet

We take $\hat{\mathbf{z}}$ as the doublet axis, and work with $d = 2b$,

$$\hat{\mathbf{b}}_1 = \hat{\mathbf{z}} = -\hat{\mathbf{b}}_2, \quad \delta_i = (y/2)\hat{\mathbf{k}} \cdot \hat{\mathbf{b}}_i,$$

$$\Delta_i = (y/2)\hat{\mathbf{r}} \cdot \hat{\mathbf{b}}_i, \quad \hat{\mathbf{k}} \cdot \hat{\mathbf{b}}_1 = \cos \alpha, \quad \hat{\mathbf{r}} \cdot \hat{\mathbf{b}}_1 = \cos \theta,$$

From (16) in terms of

$$I(\delta) = e^{i\delta} + e^{i\delta} T_{12}(\delta) = e^{i\delta} - e^{i\delta},$$

$$2D_i e^{i\delta_i} = B_0(h)I(\delta) + B_1(-h)T_{12}(\delta), \quad (30)$$

$$B_0(h) = a_0/(1 - a_0 h) = -[W_0(1 + i\Gamma_0)]^{-1},$$

$$W_0 = 1 + j, \quad \Gamma_0 = (\gamma + n)/W_0, \quad (30a)$$

$$B_1(-h) = a_0/(1 + a_0 h) = -[W_1(1 + i\Gamma_1)]^{-1},$$

$$W_1 = 1 - j, \quad \Gamma_1 = (\gamma - n)/W_1. \quad (30b)$$

Substituting D_1 and the corresponding D_2 that follows by cyclical interchange into (17), we obtain (29) with

$$F_0(\hat{\mathbf{r}}, \hat{\mathbf{k}}) = B_0(h)I(\delta)I(-\Delta)/2 = B_0 I^2/2,$$

$$F_1(\hat{\mathbf{r}}, \hat{\mathbf{k}}) = B_1(-h)T_{12}(\delta)T_{12}(-\Delta)/2$$

$$= B_1 T_{12} T_{12}^*/2. \quad (31)$$

The mode structure was anticipated in an early image development.¹¹ If we write

$$2F_0(\hat{\mathbf{r}}, \hat{\mathbf{k}}) = 4B_0 \cos \delta_1 \cos \Delta_1,$$

$$2F_1(\hat{\mathbf{r}}, \hat{\mathbf{k}}) = 4B_1 \sin \delta_1 \sin \Delta_1 \quad (31')$$

then, as discussed originally,¹¹ $2F_0$ and $2F_1$ (twice the components of \mathcal{S} symmetric and antisymmetric to reflection of either \mathbf{k} or $\hat{\mathbf{r}}$ in the midplane $z = 0$) are the multiple scattering amplitudes for ϕ incident on a single monopole at height $z = d/2$ above rigid (+) and free (-) image planes, respectively. This followed by superposing doublet solutions for $\phi = \phi(\alpha)$ and its image $\pm \phi_i = \pm \phi(\pi - \alpha)$, the wave specularly reflected from the plane $z = 0$. (We display only the key angles for image pairs.) Figure 11.4 shows the image method, and the present forms follow from (11.26) on dropping dipole contributions.

In the forward direction, $\Delta = \delta$, and (31) reduces to

$$F_0/B_0 = 1 + C = V_0, \quad F_1/B_1 = 1 - C = V_1,$$

$$C = \cos \delta_{12} = \cos(y\hat{\mathbf{k}} \cdot \hat{\mathbf{b}}_{12}) = \cos(y \cos \alpha). \quad (32)$$

Thus

$$\mathcal{S}(\hat{\mathbf{k}}, \hat{\mathbf{k}}) = B_0 V_0 + B_1 V_1$$

$$= -V_0/W_0(1 + i\Gamma_0) - V_1/W_1(1 + i\Gamma_1),$$

$$= \text{Re } \mathcal{S}(\hat{\mathbf{k}}, \hat{\mathbf{k}}) = R = R_0 + R_1 \quad (32a)$$

$$R_0 = \frac{1 + \cos(y \cos \alpha)}{(1 + j)(1 + \Gamma_0^2)}, \quad R_1 = \frac{1 - \cos(y \cos \alpha)}{(1 - j)(1 + \Gamma_1^2)}. \quad (32b)$$

The scattering cross section follows directly from R and (19), i.e., $S(\mathbf{k}) = R(\hat{\mathbf{k}})\sigma_c x_c^2/x^2$.

The cross section represents the net radiation for two coupled oscillators. The maximum value arises for axial incidence, $\mathbf{k} = \hat{\mathbf{z}}$ ($\alpha = 0^\circ$);

$$R_\Lambda = 3.546, \quad \gamma_\Lambda = 1.1467,$$

$$x_{\Lambda} = 0.01377, \quad S_\Lambda = 3.53\sigma_c, \quad (33)$$

with $\gamma = -0.357$. (The maximum value of $|\mathcal{S}|$, i.e., 3.562, is about 0.5% larger than R_Λ ; the corresponding values of y and x are 1.1073 and 0.01378.) Since $R_0 = 0.679$ and $R_1 = 2.867$, mode-1 dominates; R_Λ corresponds to a slightly detuned mode-1 resonance, and were $\Gamma_1 = 0$ we would obtain practically the same R and x at $y = 1.15$, for which $n = \gamma = -0.355$. (As shown in the following, the maximum of R_1 , i.e., $R_{1\Lambda} = 3$, also arises for $\hat{\mathbf{k}} = \hat{\mathbf{z}}$ but at small y and at frequency $x_{1\Lambda}$ for which R_0 is negligible; R_Λ is about 18% larger than $R_{1\Lambda}$.) The largest value of R for both modes in resonance ($\Gamma_0 = \Gamma_1 = 0$) arises for $y = \pi/2$ and $x = x_c$; then $R = -\mathcal{S} = 3.363$ is within 6% of R_Λ .

For incidence normal to the doublet axis, $\mathbf{k} \cdot \hat{\mathbf{z}} = 0$ ($\alpha = 90^\circ$), mode-1 vanishes to yield to simplest case of symmetrical excitation. Then $-\mathcal{S}_\Lambda = R_{0\Lambda}$, and

$$R_{0\Lambda} = 2.555, \quad y_{0\Lambda} = 4.4934,$$

$$x_{0\Lambda} = 0.013745, \quad S = 2.553\sigma_c, \quad (33')$$

with $\gamma = -n = -0.04835$. For $y = \pi/2$ and $x = x_c$, the result $R_0 = 2.54$ is within 1% of R_{0A} . (The maximum R_A is about 39% larger than R_{0A} , for polygonal arrays, the maximum scattering arises for symmetrical excitation.) Here and in the following, we include sufficient digits to show a trend.

Simple benchmarks are provided by the infinite set of values for which both modes are in resonance; $\Gamma_0 = \Gamma_1 = 0$ corresponds to $\gamma = n = 0$ at

$$x = x_c, \quad y = \pi(2l+1)/2 \equiv y_l, \quad (34)$$

$$j(y_l) = (-1)^l/y_l; \quad l = 0, 1, 2, \dots$$

For such cases,

$$-\mathcal{S} = R = (1+C)/(1+j) + (1-C)/(1-j),$$

$$C = \cos(y_l \cos \alpha) \quad (34')$$

which led to the cited supplementary values. For given \hat{k} , this same form with y arbitrary provides an upper bound for all values of $R(\hat{k})$ and $|\mathcal{S}(\hat{k}, \hat{k})|$, but the bound is realizable only for the conditions in (34). The conditions exclude $y \approx 0$, so that $R < 4$ for all values of x, y , and \hat{k} .

The average over orientation, based on $\bar{C} = j$ and $\bar{V}_n = v_n W_n$ as discussed for (26b), yields

$$\mathcal{S} = -(1+i\Gamma_0)^{-1} - (1+i\Gamma_1)^{-1},$$

$$-\text{Re } \mathcal{S} = \bar{R} = (1+\Gamma_0^2)^{-1} + (1+\Gamma_1^2)^{-1} < 2 \quad (35)$$

corresponding to $v_0 = v_1 = 1$. If either mode is in resonance, then $1 < \bar{R} < 2$, and if both are in resonance then $\bar{R} = 2$. For $\gamma = 0$, and y increasing, $\bar{R} = \bar{S}/\sigma_c$ increases from $O(y^2)$ to 1 at $y = 1$, to 2 at $y = \pi/2$, and then oscillates with maxima of 2 at $y = y_l$, the lowest local minimum (the first) is $\bar{R} \approx 1.785$ at $y \approx 2.6$.

For small $y = x/p$, the F_n of (31) reduce to collective multipoles as in (27)ff. Then $\mathcal{S} = F_0 + F_1 = A_0 + A_1 Z_1^0$ with

$$F_0 = A_0 = -\frac{1}{1+i\Gamma_0}, \quad \Gamma_0 = \frac{1}{2} \left(\gamma - \frac{1}{y} \right);$$

$$F_1 = A_1 Z_1^0 = -\frac{3}{1+i\Gamma_1} Z_1^0, \quad \Gamma_1 = \frac{6}{y^2} \left(\gamma + \frac{1}{y} \right), \quad (36)$$

$$Z_1^0 = P_1^0 P_1^0 = \cos \theta \cos \alpha.$$

The dipole factor Z_1^0 has rotational symmetry around the z axis (the axis of the doublet). The numerical factors c_n and K_n used in Γ_n of (27a)ff follow by inspection of (36).

For the collective monopole resonance ($\Gamma_0 = 0$),

$$x_0^2 = \frac{x_c^2}{1+p}, \quad w_0 = \frac{2x_0^2}{1+p} = \frac{2w_c}{(1+p)^2}; \quad (37)$$

$$\mathcal{S} \approx F_0 = -1, \quad S_0 = \sigma(x_c/x_0)^2 = \sigma_c(1+p). \quad (37')$$

For the collective dipole resonance ($\Gamma_1 = 0$),

$$x_1^2 = \frac{x_c^2}{1-p}, \quad w_1 = \frac{x_1^4}{6p^2(1-p)} = \frac{w_c^2}{6p^2(1-p)^3}; \quad (38)$$

$$\mathcal{S} \approx F_1 = -3 \cos \theta \cos \alpha, \quad (38')$$

$$S_1 = 3\sigma_c(1-p)\cos^2 \alpha, \quad \bar{S}_1 = \sigma_c(1-p), \quad (38'')$$

with maximum S_1 at axial incidence ($\alpha = 0$). Since F_1 vanishes for α or $\theta = \pi/2$ (in the midplane), we note that the

background monopole is determined by $\Gamma_0(x_1) = -p/x_1$. The peak width w_1 is much smaller than w_c . From Appendix A, we may take $p = a/d$ at least as large as $\frac{1}{4}$ (a gap of one sphere diameter) with negligible monopole-dipole coupling corrections for x_0 and x_1 .

Thus the collective oscillators uncouple for small y , and only frequencies in the neighborhoods of x_0 and x_1 yield large magnitudes $S = O(\sigma_c)$. These frequencies bracket the isolated monopole resonance value $x_0 < x_c < x_1$. To first order in p the displacements from x_c are symmetrical; $x_c - x_0 \approx x_1 - x_c \approx px_c/2$, with separation $x_1 - x_0 \approx px_c$. More generally, the displacements are asymmetrical: x_0 is closer to x_c , and x_1 is farther from x_c . The single scattered peak ($2\sigma_c$ at x_c) splits into two multiple scattered peaks (S_0 and S_1 at x_0 and x_1 , respectively) such that $S_0 + \bar{S}_1 = 2\sigma_c$ satisfies the average oscillator-strength sum rule (28).

2. Triangular array

For the equilateral triangular array, we work with $d = bv\sqrt{3}$,

$$\hat{b}_1 = \hat{x}, \quad 2\hat{b}_2 = -\hat{x} + \hat{y}\sqrt{3}, \quad 2\hat{b}_3 = -\hat{x} - \hat{y}\sqrt{3};$$

$$\delta_i = (y/\sqrt{3})\hat{k} \cdot \hat{b}_i = \delta_i(\hat{k}), \quad \Delta_i = \delta_i(\hat{r}).$$

From (16),

$$3D_1 e^{i\delta_i} = B_0(2h)I(\delta) + B_1(-h)[T_{12}(\delta) + T_{13}(\delta)],$$

$$I(\delta) = \sum_i e^{i\delta_i}, \quad (39)$$

where B_0 involves $2h$ (two neighbors) and B_1 is the same as for the doublet. From (17), we obtain (29) in terms of

$$F_0(\hat{r}, \hat{k}) = B_0 I' / 3,$$

$$F_1(\hat{r}, \hat{k}) = B_1 (T_{12} T_{12}' + T_{23} T_{23}' + T_{31} T_{31}') / 3, \quad (40)$$

with $I' = I(-\Delta)$, etc. The same B_1 arises as before, because a free surface image plane through the center of (say) sphere-1 and perpendicular to the axis (\hat{b}_{23}) of the other two, reproduces essentially the same problem as for the doublet: superposing array solutions for incident $\phi - \phi_i = \phi(\beta) - \phi(-\beta)$, the B_0 terms cancel and the multiple scattering amplitude reduces to $\mathcal{S} - \mathcal{S}_i = B_1 T_{23} T_{13}'$. A rigid image plane leads to the solution for a sphere off the plane and a hemisphere on it; for $\phi + \phi_i$ incident, the multiple scattering amplitude is $\mathcal{S} + \mathcal{S}_i = 2B_0 I' / 3 + B_1 (T_{12} + T_{13})(T_{12}' + T_{13}') / 3$. (The discussion of an "obstacle/barrier" half-plane for Fig. 5:12 is misleading; the half-plane gives rise to a more complicated four-obstacle problem than indicated.)

In the forward direction,

$$F_0/B_0 = (3+2C)/3 = V_0, \quad (41)$$

$$F_1/B_1 = 2(3-C)/3 = V_1,$$

$$C = \sum_i \cos \delta_{i(i+1)} = \sum \cos(y\hat{k} \cdot \hat{b}_{i(i+1)});$$

$$\left[\begin{matrix} \hat{b}_{12} \\ \hat{b}_{13} \end{matrix} \right] = \frac{\hat{x}\sqrt{3} \mp \hat{y}}{2}, \quad \hat{b}_{23} = \hat{y}. \quad (41a)$$

In terms of $\alpha_1 = \sin \alpha \cos \beta$ and $\alpha_2 = \sin \alpha \sin \beta$ of (1'),

$$C = 2 \cos \left(\frac{y\sqrt{3}}{2} \alpha_1 \right) \cos \left(\frac{y}{2} \alpha_2 \right) + \cos(y\alpha_2), \quad (41b)$$

where only $0^\circ < \alpha < 90^\circ$, $0^\circ < \beta < 30^\circ$ need be considered. Thus, we obtain (32a) with

$$W_0 = (1 + 2j), \quad \Gamma_0 = (\gamma + 2n)/W_0; \quad (41c)$$

$$W_1 = (1 - j), \quad \Gamma_1 = (\gamma - n)/W_1;$$

$$R_0 = \frac{3 + 2C}{3W_0(1 + \Gamma_0^2)}, \quad R_1 = \frac{2(3 - C)}{3W_1(1 + \Gamma_1^2)}. \quad (41d)$$

The maximum value of R arises for symmetrical excitation $\hat{k} = \hat{z}$ (incidence normal to the plane of the array); $\alpha = 0^\circ$, and mode-1 vanishes. Then $R_\Lambda = -\mathcal{S}_\Lambda$, and

$$R_\Lambda = R_{0\Lambda} = 5.305, \quad y_\Lambda = 4.4934, \quad (42)$$

$$x_\Lambda = 0.013749, \quad S_\Lambda = 5.298\sigma_c \approx 5.3\sigma_c,$$

with $\gamma = -2n = -0.0967$. For $x = x_c$ and $y = \pi/2$, the value $R = 5.212$ is within 2% of R_Λ .

For $\alpha = 90^\circ$ (incidence in the plane of the array), mode-1 dominates. The largest maxima arise for $\hat{k} = \hat{b}_u$ (e.g., $\beta = 30^\circ$), $C = \cos y + 2 \cos(y/2)$:

$$R(\hat{b}_u) = 3.794, \quad y \approx 1.384, \quad x = 0.01375, \quad S = 3.788\sigma_c, \quad (42a)$$

(with $R_0 = 0.8649$, $R_1 = 2.929$, and $\gamma \approx n \approx 0.134$); for $x = x_c$ and $y = \pi/2$, the result 3.764 is within 1%. The smallest maxima arise for $\hat{k} = \hat{b}_v$ (e.g., $\beta = 0^\circ$), $C = 1 + 2 \cos(y\sqrt{3}/2)$:

$$R(\hat{b}_v) = 3.791, \quad y = 1.379, \quad x = 0.01375, \quad S = 3.785\sigma_c, \quad (42b)$$

(with $R_0 = 0.8648$, $R_1 = 2.926$, and $\gamma \approx n \approx -0.138$); for $x = x_c$ and $y = \pi/2$, the result 3.758 is within 1%. The differences between (42a) and (42b) are minor. The maximum value of R for arbitrary β (and $\alpha = 90^\circ$) corresponds to a slightly detuned mode-1 resonance; practically the same values of R follow from $\Gamma_1 = 0$, $\gamma = n$. The maximum S_Λ for $\alpha = 0^\circ$ is about 40% larger than the maxima of S for $\alpha = 90^\circ$.

Both Γ_0 and Γ_1 vanish for the conditions in (34); then

$$-\mathcal{S} = R = \frac{3 + 2C}{3(1 + 2j)} + \frac{2(3 - C)}{3(1 - j)}, \quad (43)$$

which led to the supplementary values in the above. For given \hat{k} , this same form with y arbitrary provides an upper bound for R and $|\mathcal{S}|$.

The average over orientation based on $\bar{C} = 3y$ yields

$$-\bar{\mathcal{S}} = (1 + i\Gamma_0)^{-1} + 2(1 + i\Gamma_1)^{-1}, \quad (44)$$

$$\bar{R} = (1 + \Gamma_0^2)^{-1} + 2(1 + \Gamma_1^2)^{-1} < 3,$$

corresponding to $v_0 = 1$ and $v_1 = 2$. If $\Gamma_0 = 0$, then $\bar{R} > 1$; if $\bar{\Gamma}_1 = 0$, then $\bar{R} > 2$; and if both modes are in resonance, then $\bar{R} = 3$ corresponding to the average of (43). For $\gamma = 0$, and y increasing, $\bar{R} = \bar{S}/\sigma_c$ increases for $O(y^2)$ to 1.018 at $y = 1$, to 3 at $y = \pi/2$, and then oscillates with maxima of 3 at $y = y_1$; the lowest local minimum is $\bar{R} \approx 2.52$ at $y \approx 2.87$.

For small $y = x/p$, corresponding to (27)f, we obtain $\mathcal{S} = A_0(\Gamma_0) + A_1(\Gamma_1)Z_1^1$ in terms of Γ_i of (36) and

$$\Gamma_0 = \{(\gamma - 2/y), \quad (45)$$

$$Z_1^1 = P_1^1 P_1^1 \cos(\varphi - \beta) = \sin \theta \sin \alpha \cos(\varphi - \beta).$$

The present dipole is planar, Z_1^1 depends on the angle between the projections of \hat{r} and \hat{k} on the plane of the array.

For the collective monopole resonance ($\Gamma_0 = 0$),

$$x_0^2 = \frac{x_c^2}{1 + 2p}, \quad w_0 = \frac{3w_c}{(1 + 2p)^2}, \quad (46)$$

$$\mathcal{S} = F_0 = -1, \quad S_0 = \sigma_c(1 + 2p).$$

The dipole resonance specified by (38), now yields

$$\mathcal{S} = F_1 = -3Z_1^1, \quad S_1 = 3\sigma_c(1 - p)\sin^2 \alpha, \quad (47)$$

$$\bar{S}_1 = 2\sigma_c(1 - p).$$

The amplitude $F_1 = -3 \sin \theta \sin \alpha \cos(\varphi - \beta)$ vanishes for α or $\theta = 0$ (either \hat{k} or \hat{r} normal to the plane of the array) or for $\varphi - \beta = \pm \pi/2$; the background monopole, determined by $\Gamma_0(x_1) = -p/x_1$ is the same as for the doublet. The maximum of S_1 arises for incidence in the plane of the array ($\alpha = \pi/2$), and \bar{S}_1 is twice that for the doublet.

To first order in p , the displacement of x_0 below x_c is twice that of x_1 above x_c , and the separation of the corresponding peaks S_0 and S_1 is 50% larger than for the doublet, i.e., $x_1 - x_0 \approx 3x_c p/2$. The single scattered peak ($3\sigma_c$ at x_c) splits into two, such that $S_0 + \bar{S}_1 = 3\sigma_c$ satisfies the sum rule (28).

3. Tetrahedral array

We work with $d = b(8/3)^{1/2}$, $\delta_i = y(3/8)^{1/2} \hat{k} \cdot \hat{b}_i = \delta_i(\hat{k})$, $\Delta_i = \delta(\hat{r})$ in terms of $\hat{b}_i \sqrt{3} = \hat{x} + \hat{y} + \hat{z}$, $\hat{x} - \hat{y} - \hat{z}$,

$$-\hat{x} + \hat{y} - \hat{z}, \quad -\hat{x} - \hat{y} + \hat{z},$$

for $s = 1, 2, 3, 4$, respectively. From (16),

$$4D_1 e^{i\omega t} = B_0(3h)I + B_1(-h)(T_{12} + T_{13} + T_{14}),$$

$$I = \sum_i e^{i\delta_i}, \quad (48)$$

where B_0 involves $3h$ (three neighbors) and B_1 is the same as for the doublet. From (17) we obtain (29) with

$$F_0(\hat{r}, \hat{k}) = (B_0/4)II',$$

$$F_1(\hat{r}, \hat{k}) = \frac{B_1}{8} \sum_i \sum_j T_{ij} T'_{ij} = \frac{B_1}{4} \sum_i T_{ii} T'_{ii}, \quad (49)$$

such that $\sum_i^* Q_{ii} = Q_{12} + Q_{13} + Q_{14} + Q_{23} + Q_{24} + Q_{34}$. The same B_1 arises as before because a free surface image plane through the centers of two of the spheres and perpendicular to the axis of the remaining two reproduces the same problem considered originally for the doublet. (A rigid image plane leads to the solution for a sphere off the plane and two hemispheres on the plane.)

In the forward direction

$$F_0/B_0 = 2(2 + C)/4 = V_0, \quad F_1/B_1 = 2(6 - C)/4 = V_1 \quad (50)$$

$$C = \sum^* \cos \delta_{ii} = \sum^* \cos(y \hat{k} \cdot \hat{b}_{ii});$$

$$\begin{Bmatrix} \hat{b}_{12} \\ \hat{b}_{34} \end{Bmatrix} = \frac{\hat{y} \pm \hat{z}}{\sqrt{2}}, \quad \begin{Bmatrix} \hat{b}_{13} \\ \hat{b}_{24} \end{Bmatrix} = \frac{\hat{x} \pm \hat{z}}{\sqrt{2}}, \quad (50a)$$

$$\begin{Bmatrix} \hat{b}_{14} \\ \hat{b}_{23} \end{Bmatrix} = \frac{\hat{x} \pm \hat{y}}{\sqrt{2}}.$$

Combining the six terms of C (corresponding to the six edges of the tetrahedron), we have

$$C/2 = \cos \xi_1 \cos \xi_2 + \cos \xi_2 \cos \xi_3 + \cos \xi_3 \cos \xi_1, \\ \xi_i = y\alpha_i/\sqrt{2} \quad (50b)$$

with α_i as in (1'); we need consider only $0^\circ < \alpha < 90^\circ$, $0^\circ < \beta < 45^\circ$. Thus, we obtain (32a) with

$$W_0 = (1 + 3j), \quad \Gamma_0 = (\gamma + 3n)/W_0; \\ W_1 = (1 - j), \quad \Gamma_1 = (\gamma - n)/W_1; \quad (50c)$$

$$R_0 = \frac{2+C}{2W_0(1+\Gamma_0^2)}, \quad R_1 = \frac{6-C}{2W_1(1+\Gamma_1^2)}. \quad (50d)$$

The maximum value of R arises for maximally symmetric excitation $\hat{k} = \hat{b}_i$ perpendicular to a face of the corresponding tetrahedron, e.g., $\hat{k} = \hat{b}_1$ (at $\alpha = \tan^{-1}\sqrt{2} \approx 54.74^\circ, \beta = 45^\circ$) perpendicular to the three edges of the face $b_{23} + b_{34} + b_{42} = 0$. For such cases, $C = 3 + 3\cos(y\sqrt{2}/3)$,

$$R_\Lambda = R_\Lambda(\hat{b}_i) \approx 5.92, \quad y_\Lambda \approx 4.746, \\ x_\Lambda \approx 0.013735, \quad S_\Lambda \approx 5.92\sigma_c, \quad (51)$$

with $R_0 \approx 3.76$, $R_1 \approx 2.16$, $\gamma \approx 0.021$, and $n \approx -0.007$. (The maximum value of $|\mathcal{S}|$ and corresponding x are practically the same as R_Λ and x_Λ and arise for $y = 4.747$.) The result $R = -\mathcal{S} \approx 5.918$ for $x = x_c$ and $y = \pi/2$ for both modes in resonance ($\Gamma_0 = \Gamma_1 = 0$) is within 0.04% of R_Λ and $|\mathcal{S}|_{\max}$. If $\hat{k} = \hat{b}_n$ is along one edge, and therefore perpendicular to the opposite edge (e.g., $\hat{k} = \hat{b}_{14}$ perpendicular to b_{23}), then $C = 1 + \cos y + 4 \cos(y/2)$, and the largest maxima are

$$R(\hat{b}_{14}) \approx 5.05, \quad y \approx 11.21, \\ x \approx 0.013735, \quad S \approx 5.05\sigma_c \quad (51a)$$

(with $R_0 \approx 4.29$, $R_1 \approx 0.76$, $\gamma \approx 0.053$, and $n \approx -0.019$). Mode-0 dominates, and the values are practically the same as for the mode-0 resonance ($\gamma = -3n = 0.057$) at the same value of y . If both modes are in resonance for $x = x_c$ and $y = \pi/2$, the result $-\mathcal{S} = R = 5.00$ is within 1%. For \hat{k} along a coordinate axis, and therefore perpendicular to two mutually perpendicular opposite edges (e.g., $\hat{k} = \hat{z}$ perpendicular to both b_{14} and b_{23}) we have $C = 2 + 4 \cos(y/\sqrt{2})$, and the largest maxima are

$$R(\hat{z}) \approx 4.84, \quad y \approx 10.54, \quad x \approx 0.01375, \quad S \approx 4.83\sigma_c, \quad (51b)$$

(with $R_0 \approx 3.73$, $R_1 \approx 1.10$, $\gamma \approx -0.106$, and $n \approx 0.0417$). Mode-0 dominates, and the values are practically the same as for the mode-0 resonance ($\gamma = -3n = -0.125$) at the same value of y ; for $x = x_c$ and $y = \pi/2$, the value $-\mathcal{S} = R = 4.46$ is within 4%.

Both Γ_0 and Γ_1 vanish for the conditions in (34); then

$$-\mathcal{S}(\hat{k}, \hat{k}) = R = \frac{2+C}{2(1+3j)} + \frac{6-C}{2(1-j)}, \quad (52)$$

which was used for the supplementary values in the above. This same form for arbitrary y provides an upper bound for R and $|\mathcal{S}|$.

The average over orientation based on $C = 6j$ yields

$$-\mathcal{S} = (1 + i\Gamma_0)^{-1} + 3(1 + i\Gamma_1)^{-1}, \quad (53) \\ -\text{Re } \mathcal{S} = \bar{R} = (1 + \Gamma_0^2)^{-1} + 3(1 + \Gamma_1^2)^{-1} < 4$$

corresponding to $v_0 = 1$ and $v_1 = 3$. If $\gamma = -3n$, then $\bar{R} > 1$; if $\gamma = n$, then $\bar{R} > 2$; and if $\gamma = n = 0$, corresponding to the average of (52), then $\bar{R} = 4$. For $\gamma = 0$ and y increasing, \bar{R} increases from $O(y^2)$ to about 1.06 at $y = 1$, to 4 at $y = \pi/2$, and then oscillates with maxima of 4 at $y = y_i$; the lowest local minimum is $\bar{R} \approx 3.247$ at $y = 3.13$.

For small $y = x/p$, we obtain $\mathcal{S} = A_0 + A_1 Z_i$ in terms of Γ_i of (36) and

$$\Gamma_0 = \frac{1}{2}(\gamma - 3/y), \quad Z_i = Z_i^0 + Z_i^1 = P_i(\hat{r}, \hat{k}) = \hat{r} \cdot \hat{k}. \quad (54)$$

The monopole is the fourth of the sequence specified by

$$\Gamma_{0N} = (1/N)[\gamma - (N-1)/y], \quad N = 1, 2, 3, 4 \quad (54')$$

that we have considered. The present Z_i represents a spherical dipole with rotational symmetry around the direction of incidence.

For the collective monopole resonance ($\Gamma_0 = 0$),

$$x_0^2 = \frac{x_c^2}{1+3p}, \quad w_0 = \frac{4w_c}{(1+3p)^2}, \quad (55)$$

$$\mathcal{S} = F_0 = -1, \quad S_0 = \sigma_c(1+3p).$$

The dipole resonance specified by (38), now yields

$$\mathcal{S}(\hat{r}, \hat{k}) = F_1(\hat{r}, \hat{k}) = -3\hat{r} \cdot \hat{k}, \quad S_1 = \bar{S}_1 = 3\sigma_c(1-p). \quad (56)$$

The present S_i cannot vanish, so $F_i(\hat{r}, \hat{k})$ cannot vanish for all \hat{r} at a particular value of \hat{k} . However, since F_i vanishes for \hat{r} perpendicular to \hat{k} , the background monopole determined by $\Gamma_0(x_i) = -p/x_i$ is still of interest; (54') shows that the same value of Γ_0 arises for $\gamma = -1/y$ for all three cases $N = 2, 3$, and 4.

To first order in p , the displacement of x_0 below x_c is three times that of x_1 above x_c , and the separation of the peaks S_0 and S_1 is twice that for the doublet, $x_1 - x_0 = 2px_c$. The single scattering peak ($4\sigma_c$ at x_c) splits into two, such that $S_0 + S_1 = 4\sigma_c$ satisfies (28).

B. Three collective modes

The square, pentagon, and octahedron ($N = 4, 5$, and 6 vertices respectively) are the three regular figures specified by only two different separations of the vertices $b_i = \hat{b}\hat{b}_i$; the smaller separation represents an edge d , and the larger a diagonal dr . The associated regular arrays of N monopoles involve only two propagators $h(y)$ and $h(yr)$ in three sets \mathcal{K}_n , and the multiple scattering array amplitudes consist of three modes

$$\mathcal{S}(\hat{r}, \hat{k}) = F_0(\hat{r}, \hat{k}) + F_1(\hat{r}, \hat{k}) + F_2(\hat{r}, \hat{k}). \quad (57)$$

We consider the square, octahedral, and pentagonal arrays successively. The first two yield a common B_1 form (as in Sec. III A but in terms of the diagonal propagator), and also a common form of B_2 .

1. Square array

We work with $d = b\sqrt{2}$, $dr = d\sqrt{2} = b2$, and

$$\hat{b}_1 = \hat{x} = -\hat{b}_3, \quad \hat{b}_2 = \hat{y} = -\hat{b}_4, \\ \delta_i = (y/\sqrt{2})\hat{k} \cdot \hat{b}_i = \delta_i(\hat{k}), \quad \Delta_i = \delta_i(\hat{r}).$$

From (16),

$$4D_1 e^{i\phi_1} = B_0 I + B_1 2T_{13} + B_2 (T_{12} + T_{34}), \quad I = \sum_1^4 e^{i\phi_i}, \quad (58)$$

$$B_n = B_n(\mathcal{H}_n); \quad \mathcal{H}_0 = 2h(y) + h(y\sqrt{2}), \quad (58')$$

$$\mathcal{H}_1 = -h(y\sqrt{2}), \quad \mathcal{H}_2 = -2h(y) + h(y\sqrt{2}),$$

where B_0 and B_1 are full analogs of the versions in Sec. III A. From (17) we obtain (57) in terms of

$$F_0 = (B_0/4)I', \quad F_1 = (B_1/2)(T_{13}T'_{13} + T_{24}T'_{24}),$$

$$F_2 = (B_2/4)(T_{12} + T_{34})(T'_{12} + T'_{34}), \quad (59)$$

with $I' = I(-\Delta)$, etc. The B_n are expressed in terms of \mathcal{H}_n and γ , and then in terms of W_n and Γ_n as in (24a).

Equivalently,

$$F_0/B_0 = (\cos \delta_1 + \cos \delta_2)(\cos \Delta_1 + \cos \Delta_2),$$

$$F_1/B_1 = 2(\sin \delta_1 \sin \Delta_1 + \sin \delta_2 \sin \Delta_2), \quad (59')$$

$$F_2/B_2 = (\cos \delta_1 - \cos \delta_2)(\cos \Delta_1 - \cos \Delta_2).$$

Essentially as before, B_1 can be isolated by a free surface image plane containing the axis of one diagonal pair and perpendicular to the axis of the other; for such cases there are no contributions from the remaining two modes. Thus superposing array solutions for $\phi - \phi_1 = \phi(\beta) - \phi(-\beta)$ yields $4B_1 \sin \delta_2 \sin \Delta_2$ as the multiple scattered amplitude for ϕ incident on a single monopole at distance b from a free image plane $y=0$ (and $-\phi_1$ as the specularly reflected wave). Similarly $4F_0$ (or $4F_2$) is the multiple scattering amplitude for ϕ incident on a single monopole, say at $\hat{b}_1 = b\hat{x}$, on the axis of a z-edged 90°-corner reflector with rigid (or free) sides along $\hat{p}(\pm 45^\circ) = (\hat{x} \pm \hat{y})/\sqrt{2}$, corresponding to two infinite rigid (or free) image planes intersecting at right angles along the z axis; for either case, there are no contributions from the remaining modes. Results for the rigid (+) and free (-) corner reflectors are obtained by superposing array solutions for $\phi_1 + \phi_2 \pm (\phi_3 + \phi_4)$ with respective arguments equalling, e.g., $\beta + \pi/4, \pi + \beta + \pi/4, -\beta + \pi/4, \pi - \beta + \pi/4$; for either case, the plane wave that emerges from the corner has the same sign as that incident. A monopole on the axis of a mixed corner reflector, one side rigid and the other free, corresponding to superposing array solutions for $\phi_1 - \phi_2 - \phi_3 + \phi_4$, also serves to isolate B_1 ; the other modes do not contribute, the multiple scattering amplitude reduces to $4B_1(\sin \delta_1 - \sin \delta_2)(\sin \Delta_1 - \sin \Delta_2)$, and the plane wave emerging from the corner differs in sign from that incident.

In the forward direction

$$F_0/B_0 = (2 + C_1 + C_2)/2 = V_0,$$

$$F_1/B_1 = 2 - C_2 = V_1, \quad (60)$$

$$F_2/B_2 = (2 - C_1 + C_2)/2 = V_2,$$

$$C_1 = \sum_1^4 \cos \delta_{i(i+1)} = \sum \cos(\gamma \hat{k} \cdot \hat{b}_{i(i+1)})$$

$$= 4 \cos \xi_1 \cos \xi_2, \quad (60')$$

$$C_2 = \sum_1^2 \cos \delta_{i(i+2)} = \sum \cos(\gamma \sqrt{2} \hat{k} \cdot \hat{b}_{i(i+2)})$$

$$= \cos 2\xi_1 + \cos 2\xi_2,$$

with $\delta_i = (y/\sqrt{2})\alpha_i = \xi_i$ in terms of the direction cosines α_i . (Here and in the following, C_1 and C_2 involve near and far neighbors respectively.) For numerical computations of the resulting R based on (26a) and the present V_n and \mathcal{H}_n , we need consider only $0^\circ < \alpha < 90^\circ$, $0^\circ < \beta < 45^\circ$.

The maximum value of R arises for normal incidence ($\alpha = 0$), the case of symmetrical excitation for which mode-1 and mode-2 vanish. Then $|\mathcal{S}| = -\text{Re } \mathcal{S} = R_0$, and

$$R_\Lambda = R_{0\Lambda} = 7.7225, \quad y_\Lambda = 4.006,$$

$$x_\Lambda = 0.013757, \quad S_\Lambda = 7.703\sigma_c, \quad (61)$$

with R_Λ about 30% larger than the maximum for the tetrahedral array (the more regular of the two). For $\hat{k} = \hat{b}_1$ along a diagonal of the square (incidence along the axis of one diagonal pair and perpendicular to the axis of the other pair, e.g., $\hat{k} = \hat{x}$), we have $C_1 = 4 \cos(y/\sqrt{2})$ and $C_2 = 1 + \cos(y\sqrt{2})$. Then the largest maxima are

$$R(\hat{b}_1) = 6.189, \quad y = 1.897,$$

$$x = 0.013739, \quad S = 6.19\sigma_c, \quad (61a)$$

(with $R_0 = 0.633$, $R_1 = 1.973$, $R_2 = 3.583$). Mode-2 dominates, and mode-0 is the weakest, the result is about 20% less than R_Λ . The maxima are even smaller for $\hat{k} = \hat{b}_2$ along an edge of the square (incidence along the axes of two pairs of near neighbors and perpendicular to the axes of the opposite pairs, e.g., $\hat{k}\sqrt{2} = \hat{x} + \hat{y}$); $C_1 = 2 + \cos y$, $C_2 = 2 \cos y$, and

$$R(\hat{b}_2) = 5.150, \quad y = 4.693,$$

$$x = 0.013733, \quad S = 5.155\sigma_c, \quad (61b)$$

(with $R_0 = 3.1046$, $R_1 = 2.0456$, $R_2 = 0$). Mode-0 dominates, mode-1 is strong, and mode-2 vanishes, the result is about 33% less than R_Λ , and about 17% less than $R(\hat{b}_1)$.

The average over orientation based on $\bar{C}_1 = 4y(y)$ and $\bar{C}_2 = 2j(y\sqrt{2})$ yields the appropriate special case of (26c). We now have

$$\bar{R} = \sum_{n=0}^2 \frac{v_n}{(1 + \Gamma_n^2)} < 4; \quad v_0 = 1, \quad v_1 = 2, \quad v_2 = 1. \quad (62)$$

If $\Gamma_0 = 0$ or $\Gamma_2 = 0$, then $R > 1$; if $\Gamma_1 = 0$, then $\bar{R}_2 > 2$. The present values of v_n times the corresponding \mathcal{H}_n of (58) shows that $\sum v_n \mathcal{H}_n = 0$ as in (28a).

For small $y = p/x$, we obtain (27)ff in terms of

$$\Gamma_0 = \frac{1}{4} \left(\gamma - \frac{c_0}{y} \right), \quad c_0 = -2 - \frac{1}{\sqrt{2}};$$

$$\Gamma_1 = \frac{3}{y^2} \left(\gamma + \frac{c_1}{y} \right), \quad c_1 = \frac{1}{\sqrt{2}}; \quad (63)$$

$$\Gamma_2 = \frac{60}{y^4} \left(\gamma + \frac{c_2}{y} \right), \quad c_2 = 2 - \frac{1}{\sqrt{2}};$$

$$Z_0 = 1, \quad Z_1 = Z_1^\dagger = P_1^\dagger P_1^\dagger \cos(\varphi - \beta),$$

$$Z_2 = Z_2^\dagger = \frac{1}{3} P_2^\dagger P_2^\dagger \cos 2\varphi \cos 2\beta, \quad (63')$$

with, e.g., $P_1^\dagger = \sin \theta$ and $P_2^\dagger = 3 \sin^2 \theta$. The array amplitude \mathcal{S} comprises a collective monopole, a planar dipole, and a planar even quadrupole. The resonance frequencies are given by $x_n^2 = x_c^2/(1 - p c_n)$, and the half-power widths w_n follow from (27c) with $K_n = 1/4, 3, 60$ obtained by comparison of (63) and (27a). We need consider only the reso-

nance values of F_n and S_n , and some particular aspects for the array at hand. (We follow this same procedure for subsequent small- y illustrations.)

At the resonances $\Gamma_n = 0$, we have $\mathcal{G} \approx F_n = -(2n+1)Z_n$. For the collective monopole

$$F_0 = -i, \quad S_0 = \sigma_c(1 + p|c_0|). \quad (64)$$

For the collective dipole,

$$F_1 = -3Z_1, \quad S_1 = 3\sigma_c(1 - pc_1)\sin^2 \alpha, \quad (65)$$

$$\bar{S}_1 = 2\sigma_c(1 - pc_1)$$

where F_1 was discussed after (47), the present background-monopole is determined by $\Gamma_0(x_1) = -(p/2x_1)(1 + 1/\sqrt{2})$. For the collective quadrupole,

$$F_2 = -5Z_2, \quad S_2 = \frac{1}{2}\sigma_c(1 - pc_2)\sin^4 \alpha \cos^2 2\beta, \quad (66)$$

$$\bar{S}_2 = \sigma_c(1 - pc_2).$$

The mode $F_2 = -(15/4)\sin^2 \theta \sin^2 \alpha \cos 2\varphi \cos 2\beta$ vanishes for either α or $\theta = 0$, or for either β or φ equal to an odd multiple of $\pi/4$; these values include the cases $\hat{k} = \hat{b}_n$ discussed for (61b). The background monopole is determined by $\Gamma_0(x_2) = -p/x_2$ (the same form as in Sec. III A). The maxima of S_2 , i.e., $(15/4)\sigma_c(1 - pc_2)$, arise for $\hat{k} = \hat{b}_n$ (along a diagonal of the square). The peak width w_n decreases markedly with increasing n .

To first order in p , the displacements of the resonance frequencies x_n from x_c are given by $(x_n - x_c)/px_c = \epsilon_{0c}, \epsilon_{2c} \approx -2.707, 0.707, 1.293$; the displacement of x_0 below x_c is more than 3.8 times that of x_1 and more than twice that of x_2 above x_c . Since $\Sigma v_n c_n = c_0 + 2c_1 + c_2 = 0$, the sum $\Sigma \bar{S}_n = 4\sigma_c$ satisfies (28).

2. Octahedral array

For the regular octahedral array of six monopoles, we supplement the set \hat{b}_i for the square array by two additional elements $\hat{b}_5 = -\hat{b}_6 = \hat{z}$ to obtain

$$6D_1 e^{i\mathbf{k} \cdot \mathbf{r}} = B_0 I + B_1 3T_{13} + B_2 (T_{12} + T_{34} + T_{15} + T_{36}), \quad (67)$$

$$I = \sum_i e^{i\mathbf{k} \cdot \mathbf{r}_i}$$

$$B_0 = B_0(\mathcal{H}_0), \quad \mathcal{H}_0 = 4h(y) + h(y/2), \quad (67')$$

where B_n now involves propagators from five neighbors, but B_1 and B_2 are the same as in (58').

The corresponding version of (59) is

$$6F_0/B_0 = II', \quad (68)$$

$$2F_1/B_1 = T_{13}T'_{13} + T_{24}T'_{24} + T_{36}T'_{36}$$

$$6F_2/B_2 = (T_{12} + T_{34})(T'_{12} + T'_{34})$$

$$+ (T_{15} + T_{36})(\quad)' + (T_{25} + T_{46})(\quad)',$$

where, for brevity, $(\quad)'$ represents the form on its left with argument $-\Delta$ instead of δ . Similarly, we generalize (59') by

$$3F_0/2B_0 = (\cos \delta_1 + \cos \delta_2 + \cos \delta_3)$$

$$\times (\cos \Delta_1 + \cos \Delta_2 + \cos \Delta_3),$$

$$F_1/2B_1 = \sin \delta_1 \sin \Delta_1 + \sin \delta_2 \sin \Delta_2 + \sin \delta_3 \sin \Delta_3,$$

$$3F_2/2B_2 = (\cos \delta_1 - \cos \delta_2)(\cos \Delta_1 - \cos \Delta_2)$$

$$+ (\cos \delta_1 - \cos \delta_3)(\quad)'$$

$$+ (\cos \delta_2 - \cos \delta_3)(\quad)', \quad (68')$$

The discussion of (59') in terms of free surface image planes is fully applicable. Thus B_1 is the same as for the square because the earlier problem is reproduced by a free surface image plane through the centers of four spheres (the vertices of a square) and perpendicular to the axis of the remaining two. Similarly B_2 is the same as for the square, because two additional spheres on the z edge of the free corner reflector discussed for the square have no effect.

In the forward direction

$$F_0/B_0 = (3 + C_1 + C_2)/3 = V_0, \quad (69)$$

$$F_1/B_1 = 3 - C_2 = V_1,$$

$$F_2/B_2 = (6 - C_1 + 2C_2)/3 = V_2,$$

where C_1 consists of 12 terms in $\cos(\mathbf{y} \cdot \hat{k} \cdot \hat{b}_n)$ and C_2 of three terms in $\cos(\mathbf{y} \cdot 2\hat{k} \cdot \hat{b}_n)$, corresponding to the edges and diagonals of the octahedron respectively. Combining terms, we generalize (60') by

$$C_1/4 = \cos \xi_1 \cos \xi_3 + \cos \xi_2 \cos \xi_3 + \cos \xi_3 \cos \xi_1, \quad (69')$$

$$C_2 = \cos 2\xi_1 + \cos 2\xi_2 + \cos 2\xi_3,$$

with $\xi_i = (y/\sqrt{2})\alpha_i$. Comparison of C_1 with C of (50b) for the tetrahedron shows that $C_1 = 2C$, the normals of the octahedron's four pairs of parallel faces equal the four values of \hat{b}_i for the tetrahedron. As before, for numerical computations of R of (26a) we need consider only $0^\circ < \alpha < 90^\circ$, $0^\circ < \beta < 45^\circ$.

The maximum value of R arises for the cases of highest symmetry, $\hat{k} = \hat{b}_i$ along a diagonal (i.e., incidence along the axis of a diagonal pair and therefore normal to a diametral square array, e.g., $\hat{k} = \hat{z}$); then $C_1 = 4 + 8 \cos(y/\sqrt{2})$, $C_2 = 2 \cos(y\sqrt{2})$, and

$$R_\Lambda = 9.23, \quad y_\Lambda = 4.248, \quad x_\Lambda = 0.01376, \quad (70)$$

$$S_\Lambda = 9.197\sigma_c.$$

Here $R_0 = 6.02$, $R_1 = 0.036$, $R_2 = 3.17$; mode-0 dominates, mode-2 is strong, and mode-1 is minor. For $\hat{k} = \hat{n}$ normal to two parallel faces (i.e., incidence normal to two parallel triangular arrays, e.g., $\hat{k}\sqrt{3} = \hat{x} + \hat{y} + \hat{z}$), $C_1 = 6 + 6 \cos(y\sqrt{2}/3) = 6 + 2C_2$,

$$R(\hat{n}) = 8.66, \quad y = 4.649, \quad x = 0.01373, \quad (70')$$

$$S = 8.67\sigma_c,$$

(with $R_0 = 3.33$, $R_1 = 5.33$, $R_2 = 0$); mode-1 dominates and mode-2 vanishes. For $\hat{k} = \hat{b}_n$ normal to two opposite edges (e.g., $\hat{k}\sqrt{2} = \hat{x} + \hat{y}$), $C_1 = 2 + 2 \cos y + 8 \cos(y/2)$, $C_2 = 1 + 2 \cos y$, and

$$R(\hat{b}_n) = 8.49, \quad y = 11.4, \quad x = 0.01373, \quad S = 8.50\sigma_c$$

(with $R_0 = 7.2857$, $R_1 \approx 1.178$, $R_2 \approx 0.031$); mode-0 dominates, and mode-2 is minor.

The average over orientation based on $\bar{C}_1 = 12f(y)$, $\bar{C}_2 = 3f(y\sqrt{2})$ yields the required special cases of (26c). Now

$$\bar{R} = \sum v_n / (1 + \Gamma_n^2) < 6; \quad v_0 = 1, \quad v_1 = 3, \quad v_2 = 2. \quad (71)$$

If $\Gamma_0 = 0$, then $\bar{R} > 1$; if $\Gamma_1 = 0$, then $\bar{R} > 3$; and if $\Gamma_2 = 0$, then $\bar{R} > 2$. The present v_n times the corresponding \mathcal{H}_n show that (28a) is satisfied.

For small $y = p/x$, we obtain (27)ff in terms of Γ_1 and Γ_2 of (63), and different forms Γ_0 , Z_1 and Z_2 . Now

$$\Gamma_0 = \frac{1}{6} \left(\gamma - \frac{[c_0]}{y} \right), \quad c_0 = -4 - \frac{1}{\sqrt{2}}, \quad K_0 = \frac{1}{6}, \quad (72)$$

$Z_1 = P_1(\hat{r} \cdot \hat{k})$, $Z_2 = Z_2^0 + Z_2^1$, $Z_2^0 = P_2^0 P_2^0$, (72a) with, e.g., $P_2^0 = 1 - (3/2) \sin^2 \theta$. Because of higher symmetry, the dipole is as complete as for the sphere, but the quadrupole still lacks the odd terms Z_2^1 and Z_2^2 of (7). Explicitly, from Z_2^1 of (63'), we now have

$$\begin{aligned} Z_2 &= (1 - \frac{1}{2} \sin^2 \theta) (1 - \frac{1}{2} \sin^2 \alpha) \\ &\quad + \frac{1}{2} \sin^2 \theta \sin^2 \alpha \cos 2\varphi \cos 2\beta \\ &= \frac{1}{6} (3 \cos 2\theta + 1) (3 \cos 2\alpha + 1) \\ &\quad + \frac{1}{6} (1 - \cos 2\theta) (1 - \cos 2\alpha) \cos 2\varphi \cos 2\beta, \end{aligned} \quad (72b)$$

where the form in terms of 2θ and 2α delineates quadrupole characteristics. The form Z_2 vanishes if either α or $\theta = \sin^{-1} \sqrt{2/3}$ and if either β or φ is an odd multiple of $\pi/4$, these values include the cases $k = \hat{n}$ discussed for (70').

For the monopole resonance,

$$F_0 = -1, \quad S_0 = \sigma_c (1 + p[c_0]), \quad (73)$$

The dipole resonance specified by $c_1 = 1/\sqrt{2}$ as for (65) now yields

$$F_1 = -\hat{r} \cdot \hat{k}, \quad S_1 = \bar{S}_1 = 3\sigma_c (1 - pc_1), \quad (74)$$

with background monopole determined by $\Gamma_0(x_1) = -(p/3x_1)(2 + 1/\sqrt{2})$. The quadrupole resonance specified by $c_2 = 2 - 1/\sqrt{2}$ as for (66) yields

$$\begin{aligned} F_2 &= -5Z_2, \\ S_2 &= \frac{1}{2} [(2 - 3 \sin^2 \alpha)^2 + 3 \sin^2 \alpha \cos^2 2\beta] \sigma_c (1 - pc_2), \\ \bar{S}_2 &= 2\sigma_c (1 - pc_2), \end{aligned} \quad (75)$$

with background monopole determined by $\Gamma_0(x_2) = -p/x_2$ as before. The maxima of $S_2(\hat{k})$, i.e., $5\sigma_c (1 - pc_2)$, arise for $\hat{k} = \hat{b}_i$ (along a diagonal of the octahedron).

To first order in p , the displacement of the resonance frequencies are given by $(x_n - x_c)2/px_c \approx -4.707, 0.707, 1.293$; the displacement of x_0 below x_c is more than 6.6 times that of x_1 and more than 3.6 times that of x_2 above x_c . Since $\sum v_n c_n = c_0 + 3c_1 + 2c_2 = 0$, the sum $\sum \bar{S}_n = 6\sigma_c$ satisfies (28).

3. Pentagonal array

In terms of $\mu = \pi/5 = 36^\circ$, we have $d = b \sin \mu$ and $d\tau = d \sin 2\mu = b \sin 2\mu$. We work with $\delta_s = (y/2 \sin \mu) > \hat{k} \cdot \hat{b}_s$, where $\hat{b}_s = \hat{\rho}[(s-1)2\mu]$ corresponds to

$$\hat{b}_1 = \hat{x}, \quad \begin{Bmatrix} \hat{b}_2 \\ \hat{b}_3 \end{Bmatrix} = \hat{x} \cos 2\mu \pm \hat{y} \sin 2\mu,$$

$$\begin{Bmatrix} \hat{b}_3 \\ \hat{b}_4 \end{Bmatrix} = -\hat{x} \cos \mu \pm \hat{y} \sin \mu.$$

Since $\sum \hat{b}_s = 0$ requires $1 + 2 \cos 2\mu - 2 \cos \mu = \tau^2 - \tau - 1 = 0$, it follows that

$$\begin{aligned} \tau &= 2 \cos \mu = (1 + \sqrt{5})/2 \approx 1.618, \quad \tau - \tau^{-1} = 1, \\ \tau^2 + \tau^{-2} &= 3, \quad \tau + \tau^{-1} = \sqrt{5}. \end{aligned}$$

From (16), with $I = \sum \hat{b}_s e^{i\delta_s}$,

$$\begin{aligned} 5D_1 e^{i\delta_1} &= B_0 I + B_1 [\tau(T_{13} + T_{14}) - (T_{12} + T_{15})/\tau] \\ &\quad + B_2 [\tau(T_{12} + T_{15}) - (T_{13} + T_{14})/\tau], \end{aligned} \quad (76)$$

$$B_n = B_n(\mathcal{H}_n); \quad \mathcal{H}_0 = 2h(y) + 2h(y\tau),$$

$$\mathcal{H}_1 = h(y)/\tau - h(y\tau)\tau,$$

$$\mathcal{H}_2 = -h(y)\tau + h(y\tau)/\tau. \quad (76')$$

From (17), we obtain (57) in terms of

$$\begin{aligned} 5F_0 &= B_0 I I', \quad 5F_1 = B_1 (M_2 \tau - M_1/\tau), \\ 5F_2 &= B_2 (M_1 \tau - M_2/\tau), \end{aligned} \quad (77)$$

$$M_1 = \sum T_{i(i+1)} T'_{i(i+1)}, \quad M_2 = \sum T_{i(i+2)} T'_{i(i+2)}. \quad (77a)$$

The sets M_1 and M_2 involve δ_i and the phases δ_{i+1} and δ_{i+2} of the near and far neighbors, respectively. The phase differences δ_{ij} in the two sets form matched pairs because each edge is parallel to an appropriate diagonal:

$$\begin{aligned} \begin{Bmatrix} \hat{b}_{12} \\ \hat{b}_{31} \end{Bmatrix} &= \begin{Bmatrix} \hat{b}_{33} \\ \hat{b}_{42} \end{Bmatrix} = \pm \hat{x} \sin \mu - \hat{y} \cos \mu, \\ \begin{Bmatrix} \hat{b}_{23} \\ \hat{b}_{41} \end{Bmatrix} &= \begin{Bmatrix} \hat{b}_{14} \\ \hat{b}_{31} \end{Bmatrix} = \pm \hat{x} \sin 2\mu + \hat{y} \cos 2\mu, \\ \hat{b}_{34} &= \hat{b}_{25} = \hat{y}, \end{aligned} \quad (77b)$$

Thus $\delta_{12} = y\hat{k} \cdot \hat{b}_{12}$, $\delta_{33} = y\hat{k} \cdot \hat{b}_{33} = \tau\delta_{12}$, etc.

In the forward direction

$$\begin{aligned} F_0/B_0 &= (5 + 2C_1 + 2C_2)/5 = V_0, \\ F_1/B_1 &= 2(5 + C_1/\tau - C_2\tau)/5 = V_1, \\ F_2/B_2 &= 2(5 - C_1\tau + C_2/\tau)/5 = V_2, \end{aligned} \quad (78)$$

$$C_1 = \sum \cos \delta_{i(i+1)} = C_1(y),$$

$$C_2 = \sum \cos \delta_{i(i+2)} = \sum \cos \tau \delta_{i(i+1)} = C_1(y\tau),$$

$$\begin{aligned} C_1 &= 2 \cos(\eta_1 \sin \mu) \cos(\eta_2 \cos \mu) \\ &\quad + 2 \cos(\eta_1 \sin 2\mu) \cos(\eta_2 \cos 2\mu) + \cos \eta_3, \\ \eta_i &= y\alpha_i. \end{aligned} \quad (78')$$

The V_n and \mathcal{H}_n determine R of (26a) for numerical considerations.

For normal incidence ($\hat{k} = \hat{z}$), $C_1 = C_2 = 5$ and mode-1 and mode-2 vanish. The maximum is given by

$$\begin{aligned} R_\lambda &= R_{0\lambda} = 8.43, \quad y_\lambda = 3.439, \\ x_\lambda &= 0.01377, \quad S_\lambda \approx 8.4\sigma_c. \end{aligned} \quad (79)$$

For $\hat{k} = \hat{b}_s$ (perpendicular to an edge of the pentagon), e.g., $\hat{k} = \hat{x}$,

$$C_1(y) = 2 \cos(y \sin \mu) + 2 \cos(y \sin 2\mu) + 1, \\ C_2 = C_4(y\tau). \quad (79a)$$

For $\hat{k} = \hat{b}_{st}$ along an edge, e.g., $\hat{k} = \hat{y}$,

$$C_1(y) = 2 \cos(y \cos \mu) + 2 \cos(y \cos 2\mu) + \cos(y), \\ C_2 = C_4(y\tau). \quad (79b)$$

The average over orientation based on $\bar{C}_1 = 5j(y)$, $\bar{C}_2 = 5j(y\tau)$ yields (26c). Now,

$$\bar{R} = \sum v_n / (1 + \Gamma_n^2) < 5; \quad v_0 = 1, \quad v_1 = v_2 = 2. \quad (80)$$

If $\Gamma_0 = 0$, then $\bar{R} > 1$; if $\Gamma_1 = 0$ or $\Gamma_2 = 0$, then $R > 2$. To demonstrate that (28a) is satisfied, note that the present v_n times the corresponding \mathcal{H}_n of (76') leads to

$$\sum v_n \mathcal{H}_n = 2[h(y) + h(y\tau)](1 - \tau + \tau^{-1}), \quad (80')$$

which vanishes because $\tau - \tau^{-1} = 1$.

For small $y = p/x$, we obtain (27) if in terms of

$$\Gamma_0 = \frac{1}{5} \left(\gamma - \frac{c_0}{y} \right), \quad c_0 = -2\tau, \\ \Gamma_1 = \frac{6}{y^2 \tau \sqrt{5}} \left(\gamma + \frac{c_1}{y} \right), \quad c_1 = \frac{1}{\tau^2}; \quad (81)$$

$$\Gamma_2 = \frac{120}{y^4 \tau^2} \left(\gamma + \frac{c_2}{y} \right), \quad c_2 = \frac{2}{\tau} \\ Z_0 = 1, \quad Z_1 = Z_1', \quad (81') \\ Z_2 = Z_2' = Z_{2e}' + Z_{2o}' = \frac{1}{2} P^2 P^2 \cos 2(\varphi - \beta).$$

The Z 's differ from those for the square in (63'), in that Z_2 includes the odd as well as the even terms of Z_2' . The K_n required for w_n of (27c) are given by $K_0 = 1/5$, $K_1 = 6/\tau\sqrt{5}$, and $K_2 = 120/\tau^2$.

At $\Gamma_n = 0$, we obtain (27b). For the monopole

$$F_0 = -1, \quad S_0 = \sigma_c(1 + p|c_0|). \quad (82)$$

For the dipole

$$3Z_1', \quad S_1 = 3\sigma_c(1 - pc_1)\sin^2 \alpha, \\ \bar{S}_1 = 2\sigma_c(1 - pc_1), \quad (83)$$

where F_1 was discussed after (47). The background monopole is determined by $\Gamma_0(x_1) = -(p/x_1)(1/\tau^2 + 2\tau)$. For the quadrupole,

$$F_2 = -5Z_2', \quad S_2 = (15/4)\sigma_c(1 - pc_2)\sin^4 \alpha, \quad (84) \\ \bar{S}_2 = 2\sigma_c(1 - pc_2),$$

where F_2 vanishes for either α or $\theta = 0$, or for $\varphi - \beta$ equal to an odd multiple of $\pi/4$. The background monopole is determined by $\Gamma_0(x_2) = -2p/x_2\sqrt{5}$.

To first order in p , we have $(x_n - x_c)2/p x_c = c_n \approx -3.236, 0.382, 1.236$; the displacement of x_0 below x_c is more than 8.47 times that of x_1 and more than 2.6 times that of x_2 above x_c . Since $\sum v_n c_n = c_0 + 2c_1 + 2c_2 = -2\tau + 2/\tau^2 - 4/\tau = 0$ (as follows from the listed relations for τ), the sum $\sum \bar{S}_n = 5\sigma_c$ satisfies (28).

C. Four collective modes; hexagonal array

Three different separations of the vertices $b_i = \hat{b}\hat{b}_i$ arise for the regular hexagon: $d = b$ (an edge), $d\sqrt{3}$ (a short diagonal), and $d/2$ (a diameter). The corresponding array of monopoles involves three propagators $h(y)$, $h(y\sqrt{3})$, and $h(y/2)$. The multiple scattered array amplitude consists of four collective orthogonal modes,

$$\mathcal{G}(\hat{r}, \hat{k}) = \sum_0^3 F_n(\hat{r}, \hat{k}). \quad (85)$$

We work with

$$\hat{b}_1 = \hat{x} = -\hat{b}_4, \quad 2\hat{b}_2 = \hat{x} + \hat{y}\sqrt{3} = -2\hat{b}_5, \\ 2\hat{b}_3 = -\hat{x} + \hat{y}\sqrt{3} = -2\hat{b}_6$$

corresponding to the two subsets $\hat{b}_1 + \hat{b}_3 + \hat{b}_5 = \hat{b}_2 + \hat{b}_4 + \hat{b}_6 = 0$, (such that the odd terms represent the same set that arose for the triangle). Opposite edges are parallel to a diameter, and opposite short diagonals perpendicular to a diameter, e.g., $\hat{b}_{13} = \hat{b}_{65} = \hat{b}_1 = \hat{x}$, and $\hat{b}_{25} = \hat{b}_{34} = \hat{y}$, etc. The phase factors $\exp(i\delta_i) = \exp(i\hat{y}\hat{k}\cdot\hat{b}_i)$ pair off as complex conjugates.

From (16),

$$6D_1 e^{i\delta_1} = B_0 I_{(6)} + B_1 (2T_{14} + T_{25} - T_{36}) \\ + B_2 (T_{12} + T_{15} + T_{43} + T_{46}) \\ + B_3 (T_{12} + T_{34} + T_{36}). \quad (86)$$

$$B_n = B_n(\mathcal{H}_n); \quad \mathcal{H}_0 = 2h(y) + 2h(y\sqrt{3}) + h(y/2),$$

$$\mathcal{H}_1 = h(y) - h(y\sqrt{3}) - h(y/2),$$

$$\mathcal{H}_2 = -h(y) - h(y\sqrt{3}) + h(y/2),$$

$$\mathcal{H}_3 = -2h(y) + 2h(y\sqrt{3}) - h(y/2).$$

From (17), we obtain (85) in terms of

$$6F_0/B_0 = II', \\ 6F_1/B_1 = (T_{14} + T_{25})(T_{14}' + T_{25}') \\ + (T_{25} + T_{36})(Y' + (T_{36} + T_{41})(Y', \\ 6F_2/B_2 = (T_{12} + T_{45})(T_{12}' + T_{45}') \\ + (T_{13} + T_{46})(Y' + (T_{23} + T_{36})(Y', \\ 6F_3/B_3 = (T_{12} + T_{34} + T_{36})(T_{12}' + T_{34}' + T_{36}'). \quad (87)$$

Equivalently,

$$3F_0/2B_0 = (\cos \delta_1 + \cos \delta_2 + \cos \delta_3) \\ \times (\cos \Delta_1 + \cos \Delta_2 + \cos \Delta_3), \\ 3F_1/2B_1 = (\sin \delta_1 + \sin \delta_2)(\sin \Delta_1 + \sin \Delta_2) \\ + (\sin \delta_2 + \sin \delta_3)(Y' \\ + (\sin \delta_3 - \sin \delta_1)(Y', \\ 3F_2/2B_2 = (\cos \delta_1 - \cos \delta_2)(\cos \Delta_1 - \cos \Delta_2) \\ + (\cos \delta_1 - \cos \delta_3)(Y' \\ + (\cos \delta_2 - \cos \delta_3)(Y', \\ 3F_3/2B_3 = (\sin \delta_1 - \sin \delta_2 + \sin \delta_3) \\ \times (\sin \Delta_1 - \sin \Delta_2 + \sin \Delta_3). \quad (87')$$

[Note that the forms for $n = 0$ and 2 are essentially the same as in (68') for the octahedral array.] Analogous to the procedure for the square, the present forms may be interpreted by means of three image planes $\hat{p}(\pm 30^\circ)$, $\hat{p}(90^\circ)$ in terms of z -edged 60° -corner reflectors.

In the forward direction, $F_n/B_n = V_n$ with

$$\begin{aligned} V_0 &= (6 + 2C_1 + 2C_2 + 2C_3)/6, \\ V_1 &= (12 + 2C_1 - 2C_2 - 4C_3)/6, \\ V_2 &= (12 - 2C_1 - 2C_2 + 4C_3)/6, \\ V_3 &= (6 - 2C_1 + 2C_2 - 2C_3)/6. \end{aligned} \quad (88)$$

Here C_1 consists of six cosines in $\delta_{i(i+1)}$, C_2 of six in $\delta_{i(i+2)}$, and C_3 of three in $\delta_{i(i+3)}$, corresponding to the edges, short diagonals, and diameters of the hexagon, respectively. The δ 's in C_1 and C_3 are $\pm y\hat{k} \cdot \hat{p}(\mu)$ and $y2\hat{k} \cdot \hat{p}(\mu)$, respectively, with $\mu = \pm 60^\circ$ and 0° for both sets; the δ 's in C_2 are $\pm y\sqrt{3}\hat{k} \cdot \hat{p}(\mu)$ with $\mu = \pm 30^\circ$ and 90° . Combining terms we have

$$\begin{aligned} C_1 &= \sum \cos \delta_{i(i+1)} \\ &= 4 \cos(\eta_1/2) \cos(\eta_2\sqrt{3}/2) + 2 \cos \eta_1, \\ C_2 &= \sum \cos \delta_{i(i+2)} \\ &= 4 \cos(\eta_1/2) \cos(\eta_2\sqrt{3}/2) + 2 \cos(\eta_2\sqrt{3}), \\ C_3 &= \sum \cos \delta_{i(i+3)} \\ &= 2 \cos(\eta_1) \cos(\eta_2\sqrt{3}) + \cos 2\eta_1, \end{aligned} \quad (88')$$

where $\eta_i = y\alpha_i$. The V_n and \mathcal{R}_n determine R of (26a).

For normal incidence ($\hat{k} = \hat{z}$), $C_1 = C_2 = 6$ and $C_3 = 3$, so that $V_1 = V_2 = V_3 = 0$. The maximum is given by

$$\begin{aligned} R_\lambda &= R_{0\lambda} = 9.519, \quad y_\lambda = 5.551, \\ x_\lambda &= 0.01373, \quad S_\lambda = 9.533\sigma_e. \end{aligned} \quad (89)$$

For $\hat{k} = \hat{b}_i$ (along a diameter and two edges, and normal to two short diagonals), e.g., $\hat{k} = \hat{x}$,

$$\begin{aligned} C_1 &= 4 \cos(y/2) + 2 \cos y, \\ C_2 &= 4 \cos(y/2) + 2, \\ C_3 &= 2 \cos y + \cos 2y. \end{aligned} \quad (89a)$$

For $\hat{k} = \hat{b}_{i(i+2)}$ along a short diagonal, e.g., $\hat{k} = \hat{y}$,

$$\begin{aligned} C_1 &= 4 \cos(y\sqrt{3}/2) + 2, \\ C_2 &= 4 \cos(y\sqrt{3}/2) + 2 \cos(y\sqrt{3}), \\ C_3 &= 2 \cos(y\sqrt{3}) + 1. \end{aligned} \quad (89b)$$

For this case, V_3 vanishes.

The average over orientation based on $\bar{C}_1 = 6j(y)$, $\bar{C}_2 = 6j(y\sqrt{3})$, $\bar{C}_3 = 3j(2y)$ yields (26c). Now

$$R = \sum v_n (1 + \Gamma_n^2)^{-1} < 6, \quad (90)$$

where $v_n = 1, 2, 2, 1$ for $n = 0, 1, 2, 3$, respectively. If Γ_0 or $\Gamma_3 = 0$, then $\bar{R} > 1$, if Γ_1 or $\Gamma_2 = 0$, then $\bar{R} > 2$. The present v_n times the corresponding \mathcal{R}_n of (86') show that (28a) is satisfied.

For small $y = p/x$, we obtain (27) if in terms of

$$\begin{aligned} \Gamma_0 &= \frac{1}{6} \left(\gamma - \frac{|c_0|}{y} \right), \quad c_0 = -\frac{5}{2} - \frac{2}{\sqrt{3}}; \\ \Gamma_1 &= \frac{1}{y^2} \left(\gamma + \frac{c_1}{y} \right), \quad c_1 = \frac{1}{\sqrt{3}} - \frac{1}{2}; \\ \Gamma_2 &= \frac{20}{y^4} \left(\gamma + \frac{c_2}{y} \right), \quad c_2 = \frac{1}{2} + \frac{1}{\sqrt{3}}; \\ \Gamma_3 &= \frac{420}{y^6} \left(\gamma + \frac{c_3}{y} \right), \quad c_3 = \frac{5}{2} - \frac{2}{\sqrt{3}}; \\ Z_0 &= 1, \quad Z_1 = Z_1^1, \quad Z_2 = Z_2^1, \\ Z_3 &= Z_3^1 = \frac{1}{36} P_3^1 P_3^1 \cos 3\varphi \cos 3\beta, \end{aligned} \quad (91')$$

with e.g., $P_3^1 = 15 \sin^3 \theta$. The other harmonics are the same as in (81'). The K_n required for w_n of (27c) are given by $K_n = 1/6, 1, 20$, and 420 .

At $\Gamma_n = 0$, we obtain (27b). For the monopole

$$F_0 = -1, \quad S_0 = \sigma_e (1 + p|c_0|). \quad (92)$$

For the dipole,

$$\begin{aligned} F_1 &= -3Z_1^1, \quad S_1 = 3\sigma_e (1 - pc_1) \sin^2 \alpha, \\ \bar{S}_1 &= 2\sigma_e (1 - pc_1), \end{aligned} \quad (93)$$

where F_1 was discussed after (47); the background monopole is determined by $\Gamma_0 = p(2 + \sqrt{3})/6x_1$. For the quadrupole,

$$\begin{aligned} F_2 &= -5Z_2^1, \quad S_2 = \frac{1}{2} \sigma_e (1 - pc_2) \sin^2 \alpha, \\ \bar{S}_2 &= 2\sigma_e (1 - pc_2), \end{aligned} \quad (94)$$

where F_2 was discussed after (74); the background monopole is determined by $\Gamma_0 = -p(3 + \sqrt{3})/6x_2$. For the octupole,

$$\begin{aligned} F_3 &= -7Z_3^1 = -\frac{1}{2} \sin^3 \theta \sin^3 \alpha \cos 3\varphi \cos 3\beta, \\ S_3 &= \frac{1}{2} (\sin^6 \alpha \cos^2 3\beta) \sigma_e (1 - pc_3), \\ \bar{S}_3 &= \sigma_e (1 - pc_3), \end{aligned} \quad (95)$$

where F_3 vanishes: if either α or $\theta = 0$, or if either β or φ is an odd multiple of $\pi/6$; the background monopole is determined by $\Gamma_0 = -5p/6x_3$.

To first order in p , we have $(x_n - x_c)^2/px_c = c_n \approx -3.6547, 0.077350, 1.07735, 1.3453$; the displacement of x_n below x_c is more than 47 times that of x_1 , more than 3.39 times that of x_2 , and more than 2.7 times that of x_3 above x_c . Since $\sum v_n c_n = c_0 + 2c_1 + 2c_2 + c_3 = 0$, the sum $\sum \bar{S}_n = 6\sigma_e$ satisfies (28).

ACKNOWLEDGMENT

Work supported in part by the Office of Naval Research.

APPENDIX A: MONOPOLE-DIPOLE COUPLING CORRECTIONS

The low-frequency results (36)ff apply for $p = x/y < 1/2$, but as indicated after (15), a development based solely on (14) for monopoles provides no criterion for the largest permissible value of the packing factor p . To obtain a practical bound for close packing, we apply the earlier results¹ for a doublet of different spheres, each consisting of a monopole

plus dipole. Specializing (1:75) to identical spheres specified by a_0 of (9) and $a_1 \approx -ix^2$, leads directly to more complete results for the resonance frequencies x_0 and x_1 .

Keeping only the k -independent corrections, replaces h in the mode coefficients B_0 and B_1 by \mathcal{H}_\pm where the subscripts $+$ and $-$ represent different propagators, i.e.,

$$\left\{ \begin{aligned} B_0 \\ B_1 \end{aligned} \right\} = \frac{-1}{1 + iy \pm h} \Rightarrow \frac{-1}{1 + iy \pm \mathcal{H}_\pm},$$

$$\mathcal{H}_\pm = h \pm \frac{a_1 h_1^2}{1 \pm a_1 h_1^2}. \quad (A1)$$

Here $h = h_0(y)$, $h_1 = -h'$, and the prime indicates differentiation with respect to y . To lowest order in k , we have $h_1 \approx 1/y^2$ and $h_1' \approx -2/y^3$; consequently

$$\mathcal{H}_\pm = j \pm i\mathcal{N}_\pm \approx 1 - \frac{x^2}{6p^2} - \frac{i}{x} p_\pm,$$

$$p_\pm = p \left(1 \mp \frac{p^3}{1 \pm 2p^3} \right). \quad (A2)$$

Thus we obtain the resonance forms (37) and (38) with $\pm p$ replaced by $\pm p_\pm$.

Explicitly, the resonance frequencies are given by

$$x_0^2 = \frac{x_c^2}{1 + p_+}, \quad p_+ = p \left(1 - \frac{p^3}{1 + 2p^3} \right) < p, \quad (A3)$$

$$x_1^2 = \frac{x_c^2}{1 - p_-}, \quad p_- = p \left(1 + \frac{p^3}{1 - 2p^3} \right) > p. \quad (A4)$$

For $p = 0.25$ (a gap of one sphere diameter), $p_+ \approx 0.246$ is about 1.6% smaller, and $p_- \approx 0.254$ is about 1.6% larger. Both x_0 and x_1 are increased, the first by about 0.16% and the second by about 0.27%. Thus the effects of the monopole-dipole coupling on the resonance frequencies is negligible at $p = 1/4$. To consider coupling effects for p closer to 1, quadrupoles and higher-order multipoles should also be included.

If we retain only the first correction to p (i.e., if we discount dipole-dipole coupling), then

$$\left\{ \begin{aligned} x_0^2 \\ x_1^2 \end{aligned} \right\} \approx \frac{x_c^2}{1 \pm p - p^4}, \quad p = \frac{a}{d} = \frac{a}{2b} \quad (A5)$$

as given originally by Strasberg¹² for the analogous problems of a single bubble near a rigid (x_0) or free (x_1) plane.

APPENDIX B: THE INDIVIDUAL COEFFICIENTS D_i

Numerical and graphical results⁵ for an individual auxiliary multiple scattering coefficient lead to incorrect notions of the behavior of the observable multiple scattering amplitude \mathcal{S} for the array. The essentials are indicated by the forward scattered \mathcal{S} based on (32),

$$\mathcal{S} = D_1 + D_2 = F_0 + F_1$$

$$= B_0(1 + \cos Y) + B_1(1 - \cos Y), \quad Y = y \cos \alpha, \quad (B1)$$

and the values of D_1 and D_2 corresponding to (30),

$$\left\{ \begin{aligned} D_1 \\ D_2 \end{aligned} \right\} = \frac{B_0}{2} (1 + \cos Y \mp i \sin Y)$$

$$+ \frac{B_1}{2} (1 - \cos Y \pm i \sin Y). \quad (B2)$$

Thus, except for symmetrical excitation ($Y = 0$, $D_1 = D_2 = B_0 = \mathcal{S}/2$), the D_i contain terms that cancel in the sum \mathcal{S} , and considerations based on an individual coefficient D_i are misleading.

The simple explicit forms for small y delineate the marked differences in the behavior of D_i and \mathcal{S} . From the series expansion of j and n , we have $B_0 = A_0/2$ and $B_1 = 2A_1/y^2$ with A_0 and A_1 as in (36), expanding $\cos Y$ and $\sin Y$, we reduce (B2) to

$$\left\{ \begin{aligned} D_1 \\ D_2 \end{aligned} \right\} = \frac{A_0}{2} + \frac{A_1}{2} (\cos^2 \alpha \pm i \frac{2}{y} \cos \alpha) \quad (B3)$$

such that the $O(y^{-1})$ cancel in the sum \mathcal{S} . In particular, for a mode-1 resonance ($\Gamma_1 = 0$, $\gamma = -1/y = -p/x_1$), the dominant term of D_1

$$\left\{ \begin{aligned} D_1 \\ D_2 \end{aligned} \right\} = \frac{-ix_1/p}{2(1 + ix_1/p)} - \frac{3}{2} (\cos^2 \alpha \pm \frac{i2p}{x_1} \cos \alpha)$$

$$\approx \mp \frac{i3p}{x_1} \cos \alpha \quad (B4)$$

with $x_1 = x_c/(1 - p)^{1/2}$ as in (38), does not appear in the sum. Thus an individual $|D_1|$ does not indicate the correct order of magnitude of the observable multiple scattering amplitude of the array $|\mathcal{S}|$.

¹⁴ Twersky, "Multiple scattering by arbitrary configurations in three dimensions," *J. Math. Phys.* 3, 88-91 (1962).

¹⁵ Twersky, "Multiple scattering of sound by a periodic line of obstacles," *J. Acoust. Soc. Am.* 53, 96-112 (1973); "Multiple scattering of waves by the doubly periodic planar array of obstacles," *J. Math. Phys.* 16, 633-643 (1975); "Lattice sums and scattering coefficients for the rectangular planar array," *J. Math. Phys.* 16, 644-657 (1975); "Low frequency coupling in the planar rectangular lattice," *J. Math. Phys.* 16, 658-666 (1975).

¹⁶ Twersky, "Multiple scattering of waves and optical phenomena," in *Proceedings of the Symposium on Recent Developments in Optics in Related Fields*, edited by D. Judd, *J. Opt. Soc. Am.* 52, 145-171 (1962).

¹⁷ Tolstoy, "Superresonant systems of scatterers. I," *J. Acoust. Soc. Am.* 80, 282-294 (1986); 81, 1987 (1987).

¹⁸ Tolstoy and A. Tolstoy, "Superresonant systems of scatterers. II," *J. Acoust. Soc. Am.* 83, 2086-2096 (1988).

¹⁹ Lorn Rayleigh, *The Theory of Sound* (Cambridge U.P., Cambridge, 1878; Dover, New York, 1945), Sec. 335.

²⁰ M. Morse and H. Feshbach, *Methods of Theoretical Physics* (McGraw-Hill, New York, 1953), p. 1483 ff.

²¹ Twersky, "Acoustic bulk parameters of random volume distributions of small scatterers," *J. Acoust. Soc. Am.* 36, 1314-1329 (1964), sec (43) ff.

²² R. Wildt, Ed., "Acoustic theory of bubbles," in *Physics of Sound in the Sea*, NDRCSummary Tech. Rep. Div. 6, Chap. 28, Vol. 8m, Washington, DC (1946).

²³ G. Gaunard, K. P. Schamhorst, and H. Uberall, "Giant monopole resonances," *J. Acoust. Soc. Am.* 65, 573-594 (1979).

²⁴ Twersky, "Multiple scattering of radiation by an arbitrary planar configuration of parallel cylinders and by two parallel cylinders," *J. Appl. Phys.* 23, 407-414 (1952).

²⁵ M. Strasberg, "The pulsation frequency of non-spherical gas bubbles in liquids," *J. Acoust. Soc. Am.* 25, 536-537 (1953).